

**NUMERICAL AND EXPERIMENTAL
INVESTIGATION OF THE EFFECT OF
CHANNEL GEOMETRY ON CAVITY
FORMATION IN MICROFLUIDIC
CHANNELS**

A THESIS SUBMITTED TO
THE GRADUATE SCHOOL OF ENGINEERING AND SCIENCE
OF BILKENT UNIVERSITY

IN PARTIAL FULFILLMENT OF THE REQUIREMENTS FOR
THE DEGREE OF
MASTER OF SCIENCE
IN
MECHANICAL ENGINEERING

By
Gökçe Özkazanç
June 2020

NUMERICAL AND EXPERIMENTAL INVESTIGATION OF THE
EFFECT OF CHANNEL GEOMETRY ON CAVITY FORMATION
IN MICROFLUIDIC CHANNELS

By Gökçe Özkazanç

June 2020

We certify that we have read this thesis and that in our opinion it is fully adequate,
in scope and in quality, as a thesis for the degree of Master of Science.

E. Yegan Erdem(Advisor)

Levent Ünlüsoy(Co-Advisor)

Barbaros Çetin

Ali Koşar

Approved for the Graduate School of Engineering and Science:

Ezhan Karaşan
Director of the Graduate School

ABSTRACT

NUMERICAL AND EXPERIMENTAL INVESTIGATION OF THE EFFECT OF CHANNEL GEOMETRY ON CAVITY FORMATION IN MICROFLUIDIC CHANNELS

Gökçe Özkazanç

M.S. in Mechanical Engineering

Advisor: E. Yegan Erdem

Co-Advisor: Levent Ünlüsoy

June 2020

Cavitation formation in low pressure regions of a flow is a chaotic distortion in fluid mechanics. Due to the complicated nature of multiphase flows, its modelling is expensive in terms of time and computational power. Opensource softwares such as OpenFOAM reduce license expenses and provide a developer friendly environment to simulate these types of complicated flows. In this thesis, by using OpenFoam software, several different geometries that cause cavitation are investigated. Presented results are compared with both literature and supported by experimental results. Experiments are carried out in microfluidic chips that are fabricated with soft lithography technique; fluorescent particles were introduced in the flow and cavity formation was observed under a fluorescent camera. Results showed that, OpenFOAM is well capable of predicting the cavitation formation in small scales. It was observed that increasing channel width reduces the pressure difference causing bubbles to form in higher input pressures. It was also seen that decreasing the channel width causes friction and viscous forces to dominate and reduce the velocity of fluid preventing the cavitation to form. Overall the modelling of cavity formation in microchannels with varying width and cross sectional profile were successfully accomplished and results were verified with experiments.

Keywords: Cavitation, OpenFoam, Throttle, Multiphase flow, interPhaseChangeFoam.

ÖZET

MİKRO KANALLARDA KANAL GEOMETRİSİNİN KAVİTASYON OLUŞUMU ÜZERİNDEKİ ETKİSİNİN SAYISAL VE DENEYSEL OLARAK İNCELENMESİ

Gökçe Özkazanç

Makine Mühendisliği, Yüksek Lisans

Tez Danışmanı: E. Yegan Erdem

İkinci Tez Danışmanı: Levent Ünlüsoy

Haziran 2020

Düşük basınçlı bölgelerdeki kavitasyon oluşumu, akışkanlar mekaniğinde kaotik bir bozulmaya sebep olmaktadır. Karmaşık doğası sebebiyle bu tarz çok fazlı akış modellemeleri hem zaman hem de bilgisayar gücü olarak pahalı olmaktadır. Bu modelleme çalışmalarının OpenFOAM gibi açık kaynaklı yazılımlar ile yapılması ise hem lisans maliyetini düşürmekte hem de, içerisinde kolayca değişiklik yapılmasına izin vermektedir. Bu kapsamda yapılan tez çalışmasında, OpenFOAM yazılımı kullanılarak, kavitasyon oluşabilecek farklı geometriler incelenmiştir. Elde edilen sonuçlar hem literatür hem de yapılan deneyler ile karşılaştırılmıştır. Çipler yumuşak fotolitografi ile üretilmiş ve florans parçacıklar ile karıştırılan akış florans mikraskobu ile görüntülenmiştir. Sonuçlar OpenFOAM'un bu tip bir modellemeyi yapabildiğini göstermiştir. Kanal çapının arttırılmasının, baloncuk oluşumunu sağlayan basınç düşüşünü azaltmaktadır. Aynı zamanda kanal çapının düşürülmesinin ise sürtünme ve viskoz kuvvetlerin baskın hale gelmesine sebep olduğu görülmüştür. Sonuç olarak, mikro kanallarda farklı geometrilerde incelenen kavitasyon oluşumu başarılı bir şekilde gözlemlenmiş ve deneyler ile doğrulanmıştır.

Anahtar sözcükler: Kavitasyon, OpenFoam, Çok Fazlı, Boğaz Akış, inter-PhaseChangeFoam.

Acknowledgement

From the start of my undergraduate education till the end of this project and even after that, I am thankful to my family for making this possible. I would not be able to succeed without their patience, support and presence.

Also, I would like to thank my advisor Asst. Prof. Yegan Erdem for her unconditional support and guidance. Her patience and vision gave me the energy and motivation to continue. Without her, nothing would be as it is now. I would also like to thank Dr. Barbaros Çetin and Dr. Ali Koşar for their critics and time as the thesis committee.

As a mentor and advisor, I am thanking to my co-advisor Dr. Levent Ünlüsoy for guiding me through this project. It was an honour to work with him.

I would also like to thank O.Berkay Sahinoglu for being the most enjoyable lab partner and making the experiments easier and more fun.

As a friend, partner in crime and a family to me, I am especially grateful for Furkan Güç's presence, he gave me the energy and strength to keep on even when I did not know that I needed.

Lastly, I would like to acknowledge the Presidency of Defence Industries, SSB, for financially supporting this research under SAYP Program.

Contents

1	Introduction	8
1.1	Thesis Overview	10
2	Measurements, Equations and Numerical Methods and Algorithms	11
2.1	Boundary Conditions	11
2.2	Coupling Experiments with Simulation	12
2.3	Governing Equations	14
2.3.1	Pressure-Velocity Calculations	16
2.4	OpenFOAM Structure	17
2.4.1	Solvers	18
3	Development of Analysis Methodology	20
3.1	Verification of Boundary Conditions	21
3.1.1	Analytical Solution	21

3.1.2	simpleFOAM	23
3.1.3	pimpleFoam	25
3.1.4	interPhaseChangeFoam	25
3.2	Geometries	31
3.2.1	Single Channel Throttle Model and Configurations	31
3.2.2	Double Channel Geometry	35
3.2.3	Triple Channel Geometry	36
3.2.4	Nozzle Inspired Channel Geometry	37
3.2.5	Double Inclined Geometry	39
4	Calculations and Simulation Results	41
4.1	Single Channel Throttle Geometry	42
4.1.1	Coefficient Calculations	42
4.1.2	Effect of Input Pressure	53
4.1.3	Effect of Channel Thickness	55
4.2	Double Channel Geometry	57
4.3	Triple Channel Geometry	59
4.4	Nozzle Inspired Channel Geometry	62
4.4.1	Smaller to Larger Cross Section	62
4.5	Double Inclined Geometry	65

- 5 Experimental Set-up, Fabrication and Results 67**
 - 5.1 Set-Up 67
 - 5.2 Fabrication of Microfluidic Chips 69
 - 5.3 Experimental Results 74

- 6 Conclusion and Future Work 80**

- A Code 88**

- B Results 92**
 - B.0.1 Discharge Coefficient Results 92
 - B.0.2 Effect of Input Pressure Results 94
 - B.0.3 $D_h Re/L$ vs. Reynolds Number Table 95
 - B.0.4 CFD Results 96

- C Masks 102**

- D Experiment Visuals 104**

List of Tables

2.1	Stable Boundary Conditions	12
2.2	Properties of Labelled Sections	13
2.3	Measured Properties in the Set-up	15
3.1	Calculated Reynolds Number	22
3.2	Boundary Conditions Implemented in OpenFoam	24
3.3	Maximum Velocity Values Obtained in OpenFoam Solvers and Analytical Solution	26
3.4	Configurations of Single Throttle Geometry	32
3.5	Total cells of the meshes	32
3.6	Total cells of the meshes	35
3.7	Dimensions of the Geometry	37
3.8	Dimensions of the Geometry	39
4.1	Measured Properties in the Set-up	41

4.2	Contraction Coefficient Results for single throttle geometry	47
4.3	Percentage Errors for Discharge Coefficient in Single Channel Ge- ometry	51
5.1	Spin parameters for base layer	69
5.2	Spin parameters for main layer	70
B.1	wRe/L for all single throttle runs	95

List of Figures

2.1	Representation of the flow in the experimental set-up	13
2.2	Measured Flow Rate Values in Different Input Pressures	14
2.3	Solution Algorithm's of a) SIMPLE and b) PISO	17
2.4	Solution Algorithm of PIMPLE	18
2.5	Case File of Simulations	19
3.1	Step by Step Methodology of Model Development	20
3.2	Rectangular channel and its dimensions for analytical solution . .	22
3.3	Velocity contour obtained from analytical solution with MATLAB	23
3.4	Rectangular channel and its dimensions for analytical solution . .	23
3.5	Mesh generated for SimpleFoam	24
3.6	Solution of SimpleFoam	24
3.7	Solution of pimpleFoam	25
3.8	Solution of interPhaseChangeFoam	26

3.9	Velocity profile of the channel (a) with a detailed view (b)	27
3.10	Velocity profile of the channel (a) with a detailed view (b)	28
3.11	Velocity difference 2D and 3D simulations	29
3.12	Pressure difference in 2D and 3D simulations	30
3.13	Geometry and boundary conditions of throttle configuration	31
3.14	a) Coarse, b) Middle and c) Fine meshe sizes created for single throttle configuration	33
3.15	Axial velocity profiles for coarse, middle and fine meshes in the throttle	34
3.16	Clock time change according to the number of CPU's	34
3.17	Geometry and boundary conditions of double throttle channel ge- ometry	35
3.18	Grid of the double throttle channel geometry	36
3.19	Geometry and boundary conditions of triple channel geometry	36
3.20	Grid of the triple channel geometry	37
3.21	Geometry and boundary conditions of nozzle inspired channel ge- ometry	38
3.22	Grid of the nozzle type channel geometry	38
3.23	Geometry and boundary conditions double inclined channel geom- etry	39
3.24	Grid of the double inclined channel geometry	40


4.1	Representation of Vena Contracta	42
4.2	Location of <i>vena contracta</i> for different channel types) a) $\beta = 0, 12$ and $A=0,6$, b) $\beta = 0, 16$ and $A=0,8$ and c) $\beta = 0, 20$ and $A=1,0$.	43
4.3	Location of <i>vena contracta</i> for different channel types) a) $\beta = 0, 12$ and $A=0,6$, b) $\beta = 0, 12$ and $A=0,5$ and c) $\beta = 0, 12$ and $A=0,4$ d) $\beta = 0, 12$ and $A=0,3$	44
4.4	Location of <i>vena contracta</i> for different Reynolds numbers a) $Re=25$ b) $Re=42.6$ and c) $Re=58$	45
4.5	Contraction Coefficient with respect to the Square Root of Reynolds number	46
4.6	Discharge Coefficient with respect to the Square Root of Reynolds number	49
4.7	Discharge Coefficient of $\beta=0,06$ and $A=0,3$	50
4.8	Discharge Coefficient of $\beta=0,16$ and $A=0,8$	50
4.9	Discharge Coefficient of $\beta=0,24$ and $A=1,2$	51
4.10	Percentage Error in Discharge Coefficient calculations	52
4.11	Velocity coefficient results for single channel Geometry	53
4.12	Pressure change along the channel at $t=0.00013s$ for different inlet pressures	54
4.13	Phase change at different input pressures	55
4.14	Representation of the Flow in the Experimental Set-up	56
4.15	Alpha Contour at $t=0.00013$ for Different Channel types	56

4.16 Velocity Contour with Respect to Time for Double Channel Geometry	57
4.17 Pressure Change in Channels in Double Channel Geometry	58
4.18 Alpha Contour with Respect to Time For Double Channel Geometry	59
4.19 Velocity Contour with Respect to Time for Triple Channel Geometry	60
4.20 Pressure Change in Channels in Triple Channel Geometry	61
4.21 Alpha Contour with Respect to Time for Triple channel geometry	61
4.22 Velocity contour with respect to time for nozzle type channel geometry	62
4.23 Velocity contour with respect to time for nozzle type channel geometry	63
4.24 Pressure changes along the centerline of the nozzle inspired geometries	64
4.25 Angles in between channels	65
4.26 Velocity contour with respect to time for nozzle type channel geometry	66
4.27 Alpha contour with respect to time for nozzle type channel geometry	66
5.1 Experimental Set up	68
5.2 Photolithography technique to produce microchips with negative photoresist	72

5.3	Visuals of the produced chips	73
5.4	Steady flow in 30 micron width channel with 3 bars input pressure	74
5.5	Steady flow in nozzle inspired geometry with 3 bars input pressure	74
5.6	Vapour Bubble in the 30 Micron Channel	75
5.7	Simulation vs. Experimental Low Density Zones	75
5.8	Symmetrical Low Density Zones in Simulation and Experiments .	76
5.9	Vortex region (a) and its movement (b)	77
5.10	Cavitation Zone	78
5.11	Symmetrical Low Density Zones	78
5.12	Cavitation Bubble with Degasified Water	79
B.1	$\beta=0,1$ and $A=0,5$	92
B.2	$\beta=0,12$ and $A=0,6$	93
B.3	$\beta=0,20$ and $A=1,0$	93
B.4	Velocity Along the channel centerline in different pressure inputs .	94
B.5	Pressure contour with respect to time for double channel geometry	96
B.6	Pressure contour with respect to time for triple channel geometry	97
B.7	Pressure contour with respect to time for nozzle inspired channel geometry	98
B.8	Pressure contour with respect to time for nozzle inspired channel geometry	98

B.9	Pressure contour with respect to time for nozzle inspired channel geometry	99
B.10	Pressure contour with respect to time for nozzle inspired channel geometry	99
B.11	Pressure contour with respect to time for double inclined geometry	100
B.12	Velocity vectors with respect to time for double inclined geometry	101
C.1	Mask 1	102
C.2	Mask 2	103
D.1	Bubble vapours for 30 micron channel	104

Nomenclature



μ	Viscosity
ρ	Density
g	Gravitational Acceleration
H	Channel Thickness
h	Channel width
h	Height
L	Length of the entrance section
P_{st}	Static Pressure
P_{tot}	Total pressure
Q	Flow Rate
W	Width of the entrance section
u	X Velocity
v	Y Velocity
w	Z Velocity

Chapter 1

Introduction

One of the commonly used techniques to cool down a high temperature combustion chamber is by circulating a coolant fluid around its shell in a small channel [1, 2]. However, as the pressure drops along the channel, fluid inside the channel changes its phase and decreases the efficiency of the cooling procedure [3], which is known as cavitation. In other words cavitation, can be defined in detail as the phase change of the fluid flow by nucleation, growth and collapse of a vapour bubble in regions where pressure drop is rapid and high [4].

The damaging effects of cavitation are undesired not only in cooling channels but also in most of the applications that includes high speed fluid flows such as nozzles [5], hydraulic machinery [6] and diesel engines [7]. Therefore, before going further in the design process of these applications, predicting these unwanted phase changes is playing an important role to reduce both the time and expenses of the system.

To predict such behaviour, several different numerical and modeling methods have already been developed [8] such as the empirical study of Shi et al. [9] or the steady state approach of Hanimann et al. [10] or on the contrary using a highly transient model as Large Eddy Simulation (LES) approaches [11, 12].

One common point in all of these different approaches is that the modelling of cavitation is expensive in terms of both computational power and time. To minimize this cost, the usage of open source softwares are emerging [13, 14]. OpenFOAM, as an opensource tool is one of the most preferred tools due to its C++ language and adaptability by the users [15] for this purpose.

On top of that, with the development of microrockets and micropropulsion systems, micropumps, microturbomachinery, etc. that creates high speed flows in microchannels, cavitation studies also merged with microfluidic applications [16]. Even though there are studies that investigated the cavitation behaviour in various types of geometries [17, 18] throttle (orifice) and venturi geometries are the main interest in the studies of cavitation in microchannels [19–21]. Therefore a variety of studies such as testing the cavitation properties of different fluids [22], predicting the possible locations of cavitation [23], effect of surface roughness [24] and experiments [19, 20, 24–28] are also focused around this geometry.

The motivation of this study consists of developing the methodology of cavitation modeling in a cost efficient manner. It is expensive to conduct experiments on large scaled systems about cavitation in industrial applications. Therefore those systems require low cost verification and validation procedures of the computational fluid dynamics solvers. This study aims to verify and validate the OpenFOAM solver of *interPhaseChangeFOAM* in small scaled channels with reducing the experiment cost by using microchannels. With this way, its usability in industrial applications such as predicting the cavitation behaviour in cooling channels of combustion chambers, will also be shown with a quick and low cost approach. Therefore, the solvers mainly aim to show the applicability of the proposed method in macro-systems in an efficient way by using a low experimental and computational cost.

1.1 Thesis Overview

In this study, cavitation will be investigated from many aspects. Firstly, apart from the common geometries, behaviour of flow in different type of channels will be presented. Also, capability of OpenFOAM in small scales will be observed with the comparison of literature and experiments. With this concept, the overview of the thesis can be summarized as follows:

- Chapter 2 describes the measurements to couple the experiments with the simulations that are held on OpenFOAM as well as it introduces the main governing equations.
- Chapter 3 mainly describes the structure of OpenFoam and the solvers that it includes.
- Chapter 4 explains the choice of boundary conditions with a validation case and presents its results, leading to the simulation strategy. Geometries of the simulations are also explained in detail in this chapter.
- Chapter 5 includes the calculations of coefficients to validate the simulations and its comparison with literature. Also, results of the simulations are presented here.
- Chapter 6 explains the experimental set up that is built to conduct experiments.
- Chapter 7 presents the visuals obtained from the experiments and comparison to the simulations conducted.
- Chapter 8 is the conclusion that sums up the work conducted throughout this study and suggests future work to improve the performance of both experiments and simulations.

Chapter 2

Measurements, Equations and Numerical Methods and Algorithms

In this section, governing equations will be discussed. First section describes the exact equations and results that are used in simulations and second part describes the main equations and algorithms used by OpenFOAM foam-extend-4.1 with the description of main pressure-velocity coupling algorithms.

2.1 Boundary Conditions

Several different boundary condition couples are available for pressure-velocity systems in OpenFOAM. These combinations are already tested and grouped together regarding their stability. For incompressible systems, these boundary condition couples are classified as given in Table 2.1 [29].

Table 2.1: Stable Boundary Conditions

Inlet		Outlet		Stability
Physics	OpenFOAM	Physics	OpenFOAM	
Volume Flow Rate	flowRateVelocity	Static Pressure	fixedValue	Excellent
Total Pressure	totalPressure	Total Pressure	totalPressure	Very Good
Total Pressure	totalPressure	Static Pressure	fixedValue	Good
Static Pressure	fixedValue	Static Pressure	fixedValue	Poor

Regarding the table, total pressure for an incompressible fluid is defined as [29];

$$P_{tot} = P_{st} + \frac{1}{2}\rho\mathbf{u}^2 \quad (2.1.1)$$

where P_{st} is the static pressure and the summation of pressure in the regarding point and ρgh , \mathbf{u} is the magnitude of the velocity vector and ρ is the density.

As it is given in the equation, static pressure is known and the only unknown is the velocity, To be able to simulate the real life experimental values, velocity at the inlet must be learned. With this aim, next section explains the procedure for measuring the velocity at the inlet so that it could be implemented in the given equation 2.1 and used as a boundary condition value.

2.2 Coupling Experiments with Simulation

As an initial step for coupling simulations with experiments, velocity and pressure values of the critical points of the experimental set-up is calculated. To calculate these, experimental set-up is divided into several sections. These sections of control volume and geometrical representation of the flow path in the experiment is given in Figure 2.1. Points and sections, important for the calculations are also explicitly shown.

Relevant geometric properties of the labelled sections are given in the Table 2.2.

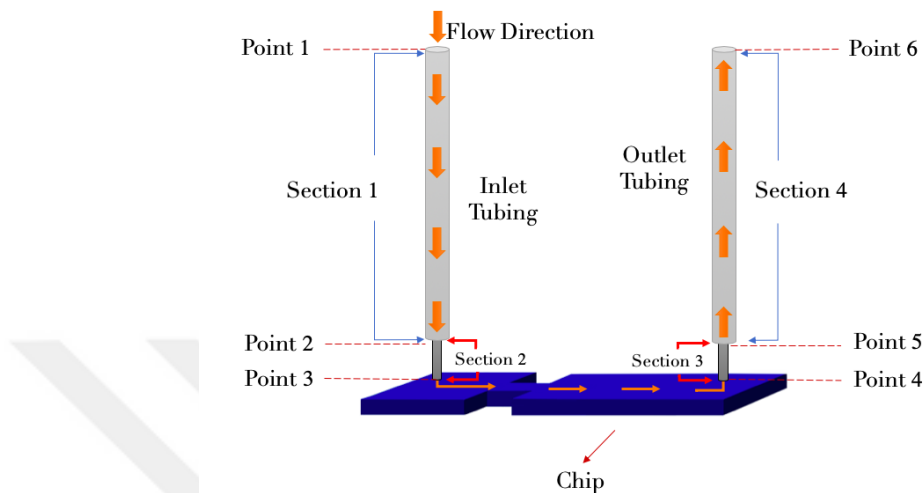


Figure 2.1: Representation of the flow in the experimental set-up

Table 2.2: Properties of Labelled Sections

	Section Area (m^2)	Length (m)
Section 1	2.0428e-07	0.31
Section 2	5.3093e-08	0.0166
Section 3	5.3093e-08	0.0166
Section 4	2.0428e-07	0.30

Flow rate entering the chip provided by the pressure pump is experimentally measured for several different pressure inputs. Values above the limit of the flow rate sensor (above 1ml/min [30]) were extrapolated through an exponential equation. Relevant graph of flow rate with respect to input pressure is given in Graph 2.2 below.

As a final step using hydraulic circuit analogy, pressure of the inlet section is calculated. All of the results are given in Table 2.3.

However, while modelling the simulations some phenomena are neglected since only the fluid flow inside the channels is simulated. These include surface roughness, hydrophobic and hydrophilic behaviour of the surfaces [31, 32]. These were neglected in order to satisfy the ease of use, implementation and repeatability of the analysis framework while capturing the requirements mentioned before.

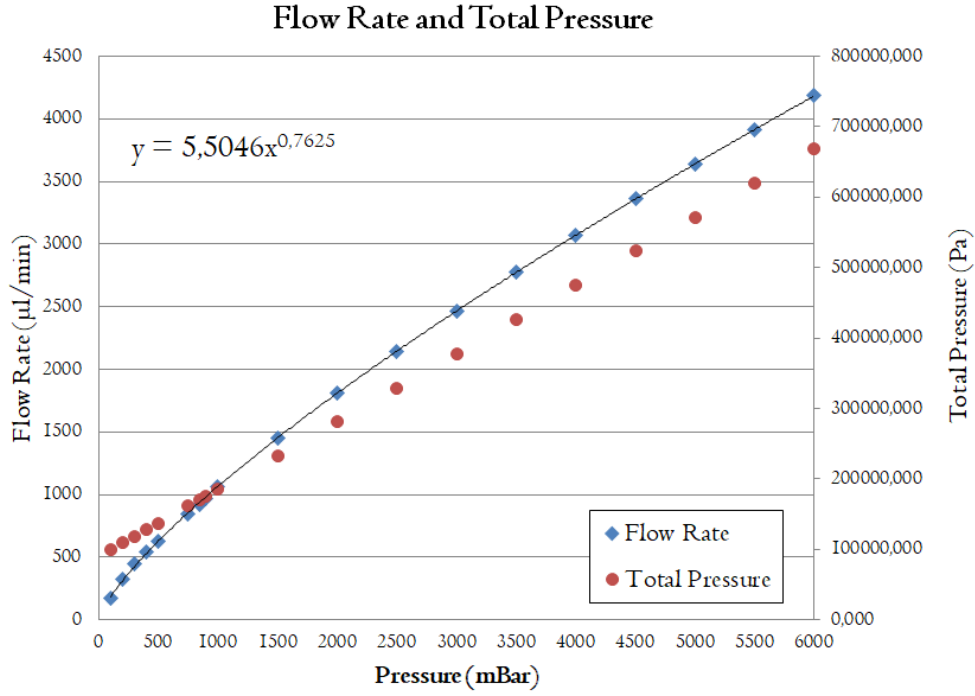


Figure 2.2: Measured Flow Rate Values in Different Input Pressures

2.3 Governing Equations

For a compressible fluid, conservation of mass is written as;

$$\frac{\partial \rho}{\partial t} + \frac{\partial(\rho \mathbf{u})}{\partial x} + \frac{\partial(\rho \mathbf{v})}{\partial y} + \frac{\partial(\rho \mathbf{w})}{\partial z} = 0 \quad (2.3.2)$$

where u , v and w are the relevant velocity vectors for the cartesian coordinates x , y and z . When fluid is incompressible, which corresponds to a constant density, equation 2.3.2 becomes as follows;

$$\frac{\partial(\rho \mathbf{u})}{\partial x} + \frac{\partial(\rho \mathbf{v})}{\partial y} + \frac{\partial(\rho \mathbf{w})}{\partial z} = 0 \quad (2.3.3)$$

Table 2.3: Measured Properties in the Set-up

Input Pressure at Point 1 (Pa)	Flow Rate (m^3/s)	Velocity (m/s)	Pressure at Point 3 (Pa)	Total Pressure (Pa)
10000	2.929e-09	0.05517	9037.294	100079.917
20000	5.341e-09	0.1006	18244.517	109290.677
30000	7.447e-09	0.1403	27552.316	118603.244
40000	9.101e-09	0.1714	37008.678	128064.467
50000	1.046e-08	0.1971	46562.002	137622.506
75000	1.409e-08	0.2655	70368.891	161445.236
85000	1.543e-08	0.2906	79928.459	171011.784
90000	1.612e-08	0.3035	84701.670	175788.826
100000	1.779e-08	0.3351	94152.773	185250.019
150000	2.424e-08	0.4565	142032.784	233178.080
200000	3.018e-08	0.5684	190080.422	281283.118
250000	3.578e-08	0.6739	238239.811	329507.981
300000	4.112e-08	0.7744	286484.656	377825.604
350000	4.624e-08	0.8710	334801.812	426222.233
400000	5.120e-08	0.9643	383171.557	474677.594
450000	5.601e-08	1.0549	431590.603	523188.216
500000	6.069e-08	1.1432	480052.378	571746.932
550000	6.527e-08	1.2293	528547.022	620343.711
600000	6.975e-08	1.3137	577074.533	668978.537

Regarding conservation of momentum equations for a compressible fluid in x , y and z coordinates are;

$$\frac{\partial(\rho\mathbf{u})}{\partial t} + \frac{\partial(\rho\mathbf{u}^2)}{\partial x} + \frac{\partial(\rho\mathbf{u}\mathbf{v})}{\partial y} + \frac{\partial(\rho\mathbf{u}\mathbf{w})}{\partial z} = -\frac{\partial p}{\partial x} + \mu\left(\frac{\partial^2\mathbf{u}}{\partial x^2} + \frac{\partial^2\mathbf{u}}{\partial y^2} + \frac{\partial^2\mathbf{u}}{\partial z^2}\right) \quad (2.3.4)$$

$$\frac{\partial(\rho\mathbf{v})}{\partial t} + \frac{\partial(\rho\mathbf{u}\mathbf{v})}{\partial x} + \frac{\partial(\rho\mathbf{v}^2)}{\partial y} + \frac{\partial(\rho\mathbf{v}\mathbf{w})}{\partial z} = -\frac{\partial p}{\partial y} + \mu\left(\frac{\partial^2\mathbf{v}}{\partial x^2} + \frac{\partial^2\mathbf{v}}{\partial y^2} + \frac{\partial^2\mathbf{v}}{\partial z^2}\right) \quad (2.3.5)$$

$$\frac{\partial(\rho\mathbf{w})}{\partial t} + \frac{\partial(\rho\mathbf{u}\mathbf{w})}{\partial x} + \frac{\partial(\rho\mathbf{v}\mathbf{w})}{\partial y} + \frac{\partial(\rho\mathbf{w}^2)}{\partial z} = -\frac{\partial p}{\partial z} + \mu\left(\frac{\partial^2\mathbf{w}}{\partial x^2} + \frac{\partial^2\mathbf{w}}{\partial y^2} + \frac{\partial^2\mathbf{w}}{\partial z^2}\right) \quad (2.3.6)$$

where μ is the viscosity. When fluid becomes incompressible, this equation transforms into the one given below for every coordinate;

$$\frac{\partial(|\mathbf{u}|)}{\partial t} + \nabla(|\mathbf{u}||\mathbf{u}|) = -\frac{1}{\rho} \nabla + \nabla (\mu \nabla |\mathbf{u}|) \quad (2.3.7)$$

2.3.1 Pressure-Velocity Calculations

OpenFOAM uses three different algorithms for combining mass conservation, pressure and momentum equations [33]. These are, semi-implicit method for pressure-linked equations (SIMPLE) pressure-implicit split-operator (PISO) and PIMPLE algorithm which is combination of both SIMPLE and PISO algorithms [33]. Main difference of these three algorithms can be summarized as follows; SIMPLE is used for modeling steady-state problems, PISO is used for transient problems with Courant Number limitation and PIMPLE is used for transient problems which requires bigger Courant Number (>1) [34]. Where Courant number is defined as follows;

$$Co = \frac{U \Delta t}{\Delta x} \quad (2.3.1.8)$$

In this manner SIMPLE, PIMPLE and PISO algorithms are summarized in 2.3 and 2.4 [35].

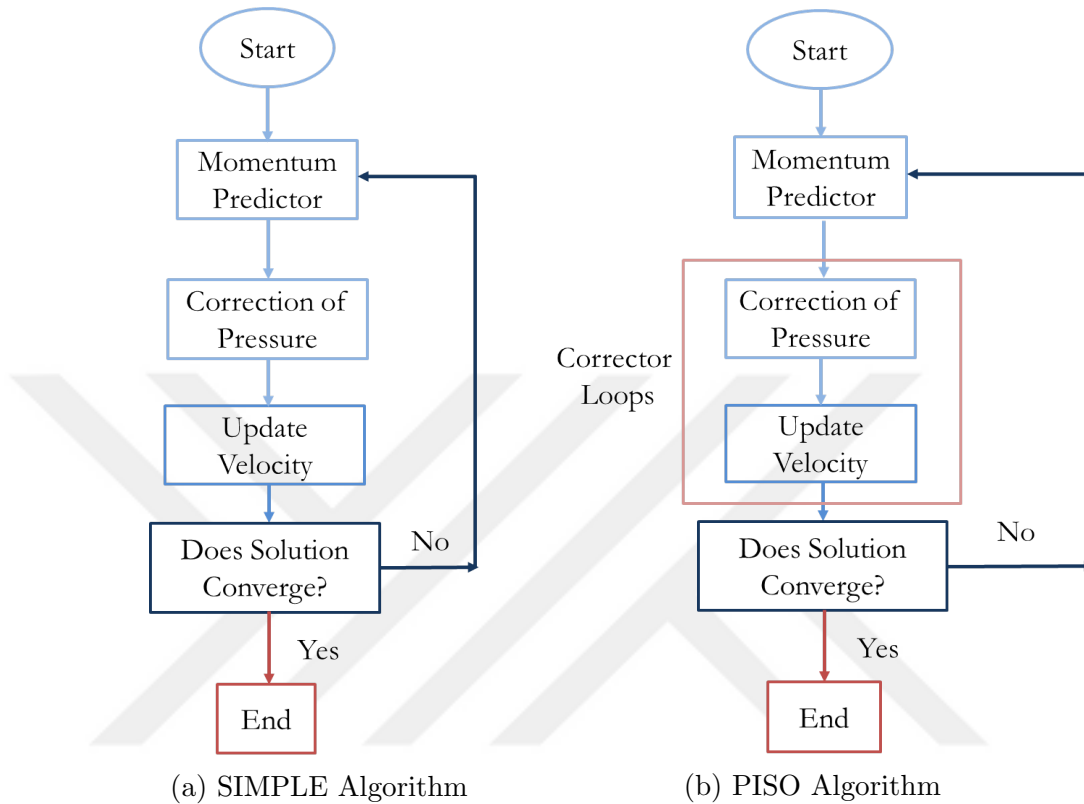


Figure 2.3: Solution Algorithm's of a) SIMPLE and b) PISO

2.4 OpenFOAM Structure

A basic OpenFOAM simulation requires 3 main subfolders which are *"0"*, *"constant"* and *"system"*. Respectively, *"0"* folder contains all the required boundary conditions for physical fields, *"constant"* directory contains mesh information of the geometry, transport properties of the fluid/fluids and turbulence properties. Finally *"system"* folder consists of solution based files such as numerical methods and simulation properties [15]. Each case runs with its relevant solver indicated in the system folder. Fields inside these folders may show diversity regarding the solver and the application, for this study all of the files are as the one given in Figure 2.5 below.

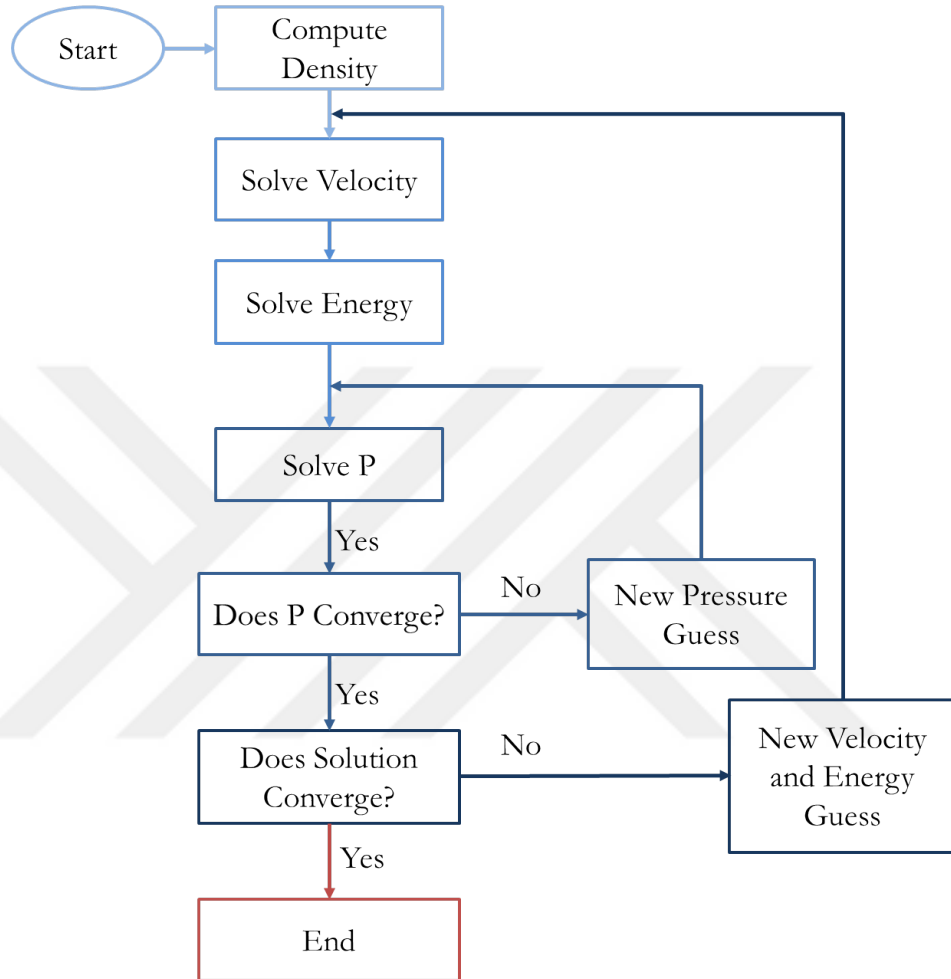


Figure 2.4: Solution Algorithm of PIMPLE

2.4.1 Solvers

OpenFOAM has many solvers adapted for modeling different physical phenomena. The ones that are used and discussed in this work are simpleFoam, pimpleFoam and interPhaseChangeFoam.

SimpleFoam solver is defined as a steady solver for incompressible fluids, whereas pimpleFoam is the transient solver for incompressible fluids and finally interPhaseChangeFoam is the transient solver for two immiscible and incompressible fluids with changing phase [33].

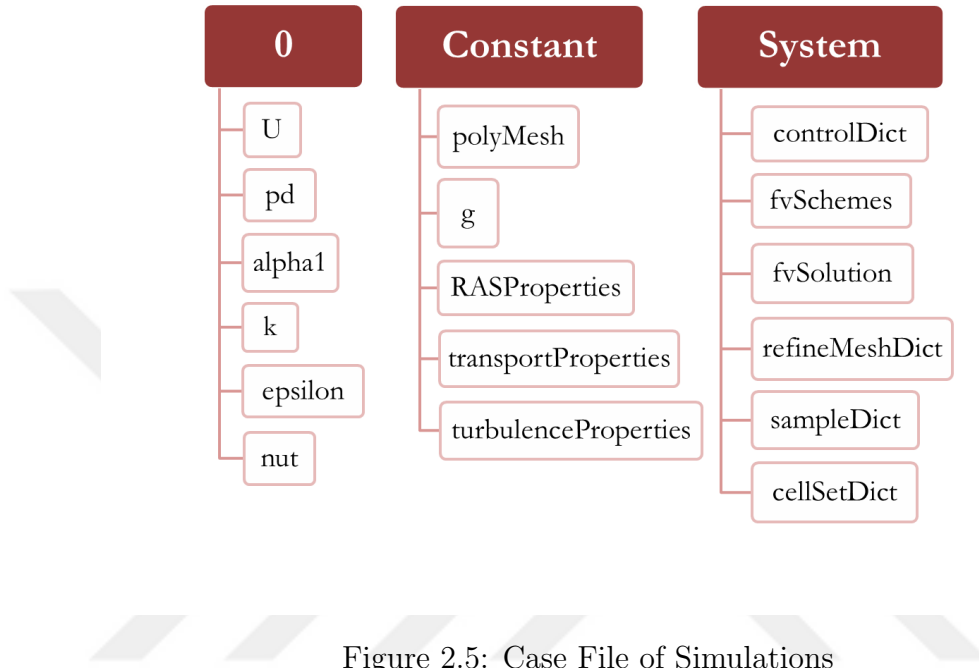


Figure 2.5: Case File of Simulations

InterPhaseChangeFoam solver is the multiphase solver that uses volume of fluid method to model cavitation and it is the main solver used for this study. Its algorithm is based on PISO which is described previously [33]. The solver also uses the *Volume of Fluid* (VOF) method to capture the interface between phase change sections of the domain. with this solver several different cavitation models can be used such as The Merkle, Schnerr-Sauer and Kunz models. Mainly these models differ from each by the methods they capture the interphase between the volumes and the coefficients used by the volume fractions [36,37]. In which, The Schnerr & Sauer Model that calculates the mixed bubble-liquid flow transiently is used for this study [37,38].

Chapter 3

Development of Analysis Methodology

Developing the analysis methodology for modelling cavitation in microchannels with OpenFOAM required several steps. With this aim, initially a simple verification case solved was a channel flow. Steps taken in order to determine the methodology was summarized in Figure 3.1. Then section continues with the description of geometries that will be used for modelling cavitation in this study.

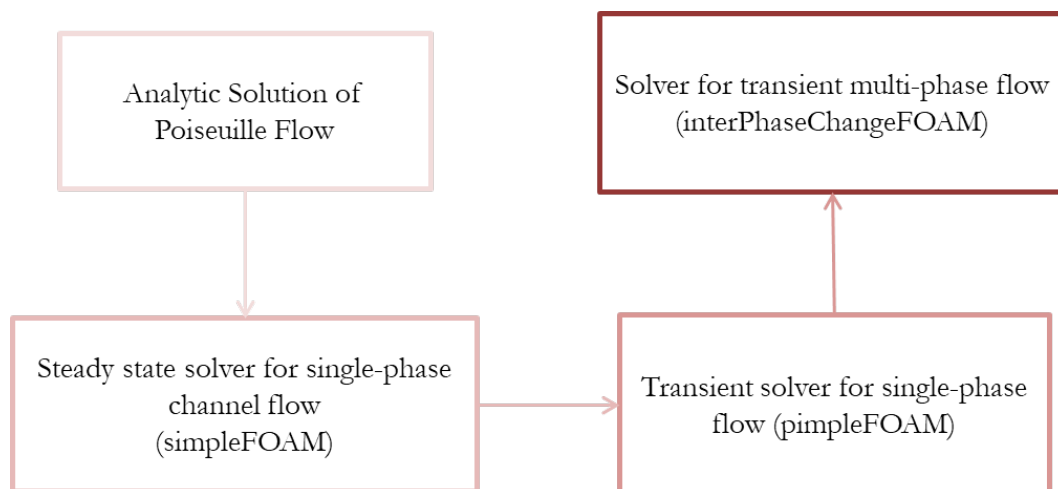


Figure 3.1: Step by Step Methodology of Model Development

3.1 Verification of Boundary Conditions

This section explains the verification study for a pressure driven flow in a rectangular channel solved with Matlab and its comparison to several solvers such as simpleFoam, pimpleFoam and interPhaseChangeFoam.

3.1.1 Analytical Solution

Studies were initially conducted on laminar channel flows which corresponds to Reynolds Number less than 2300 for most applications and calculated from the given equation below for the inlet region of the channel.

$$Re = \frac{VL\rho}{\mu} \quad (3.1.1.1)$$

in which, L is the length scale, V is the velocity, ρ is the density and μ is the dynamic viscosity. When velocity values of 2.3 are considered Reynolds Number are calculated as shown in Table 3.1 for an orifice with $60 \mu m$ width.

Simplest case for a pressure driven channel flow is Poiseuille flow. With dp/dx being the pressure difference in between inlet and outlet of the channel, w as width, L as length and μ as the dynamic viscosity, velocity profile for the laminar, steady, Poiseuille flow is calculated with the equation given below.

$$u(x) = \frac{1}{2\mu} \frac{dp}{dx} (y^2 - h^2) \quad (3.1.1.2)$$

Table 3.1: Calculated Reynolds Number

Input Pressure at Point 1 (Pa)	Velocity (m/s)	Reynolds Number
10000	0.05517	4.137
20000	0.1006	7.543
30000	0.1403	10.519
40000	0.1714	12.855
50000	0.1971	14.779
75000	0.2655	19.908
85000	0.2906	21.791
90000	0.3035	22.762
100000	0.3351	25.132
150000	0.4565	34.236
200000	0.5684	42.632
250000	0.6739	50.539
300000	0.7744	58.076
350000	0.8710	65.318
400000	0.9643	72.318
450000	1.0549	79.109
500000	1.1432	85.731
550000	1.2293	92.188
600000	1.3137	98.518

The given Poiseuille flow equation is solved for a 2D rectangular channel domain as it is given in Figure 3.2. Pressure difference is provided as 2 Bars and the fluid properties of water is used.

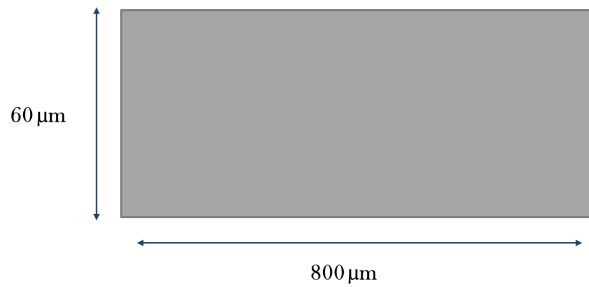


Figure 3.2: Rectangular channel and its dimensions for analytical solution

Mesh of the solution domain for analytic solution is produced as 200x200 cells in both x and y directions. Solution of this equation is obtained via MATLAB. Complete code for the solution is provided in A.

Velocity contour obtained from the analytical solution is given in Figure 3.3.

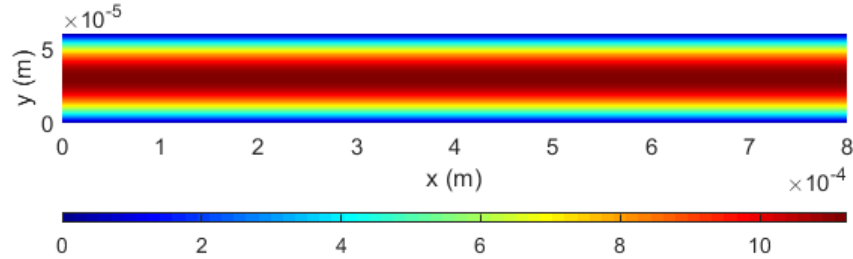


Figure 3.3: Velocity contour obtained from analytical solution with MATLAB

3.1.2 simpleFOAM

The corresponding steady, single phase, laminar solver for OpenFOAM is chosen as *simpleFOAM* [15]. Solution domain given in 3.4 is modelled as 2D.

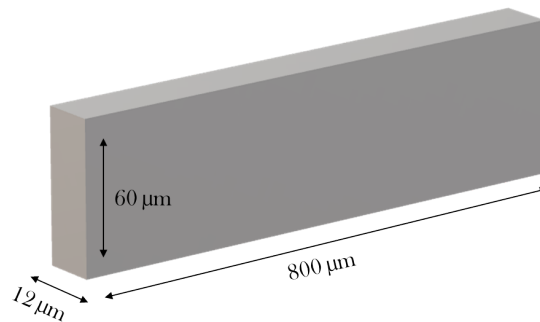


Figure 3.4: Rectangular channel and its dimensions for analytical solution

Mesh is generated with the open source mesh generator of OpenFOAM, *blockMesh*. *Yplus* is kept around 1 and mesh size is 108×50 for X and Y coordinates respectively which is given in Figure 3.5.

SimpleFoam requires dynamic pressure in m^2/s^2 unit, therefore given 288000 Pa pressure is divided 1000 kg/m^3 for corresponding constant density of the water. Walls are given as no slip boundary conditions. Summary of the boundary conditions are given in Table 3.2.

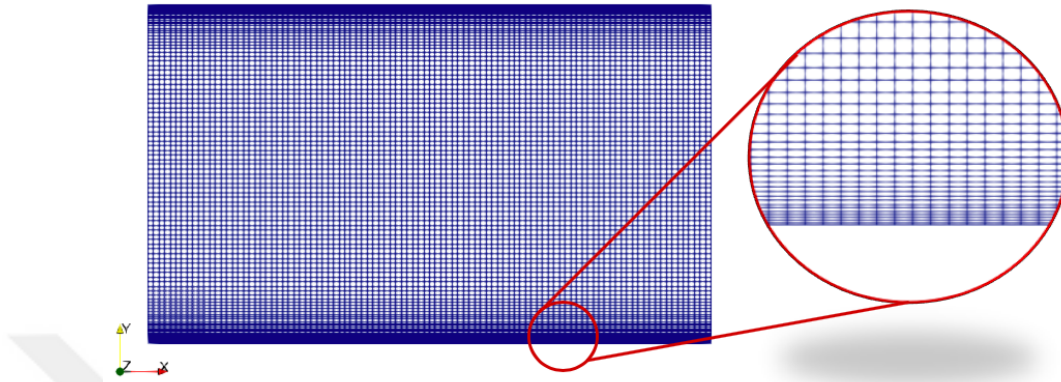


Figure 3.5: Mesh generated for SimpleFoam

Table 3.2: Boundary Conditions Implemented in OpenFoam

Name	Type	Velocity (m/s)	Pressure ($kg/m.s^{-1}$)
Inlet	patch	pressureInletVelocity	totalPressure
Outlet	patch	InletOutlet	fixedValue
Wall	wall	fixedValue	zeroGradient
frontBack	empty	empty	empty

Analysis is stopped when convergence of 10^{-6} order is obtained. Velocity contour of the analysis given with these conditions is shown in 3.6.

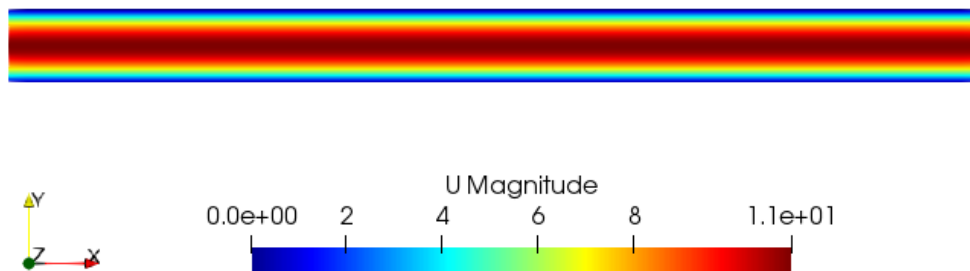


Figure 3.6: Solution of SimpleFoam

3.1.3 pimpleFoam

As a transient incompressible solver, *pimpleFoam* is used for the same case [33]. Same boundary conditions are used in a similar manner with *SimpleFoam*. Geometry, mesh and transport properties are also kept same with previous case. Only difference with *SimpleFoam* is the transient solver setup. Time step is taken as 10^{-5} , solution is stopped when the same residual which is 10^{-6} is obtained.

Solution obtained from the latest time from *pimpleFoam* for velocity contour is given in Figure 3.7 below.

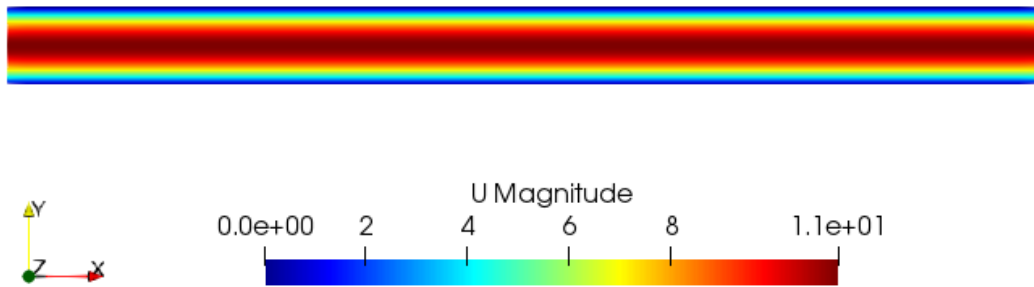


Figure 3.7: Solution of pimpleFoam

3.1.4 interPhaseChangeFoam

Regarding the previous sections, boundary conditions for the *interPhaseChangeFoam* which is a transient solver for two incompressible fluids with changing phases, was used similar to the *simpleFoam* and *pimpleFoam* [33]. Same geometry and mesh with previous sections are used for evaluating the performance of *interPhaseChangeFoam*. Input and output pressures are given as 288000 Pa and 88000 Pa for pressure boundary conditions. Obtained results are as it is presented in Figure 3.8.

To inspect the differences between the OpenFoam solvers and analytical solution velocity profile obtained from the center of the channel is investigated.

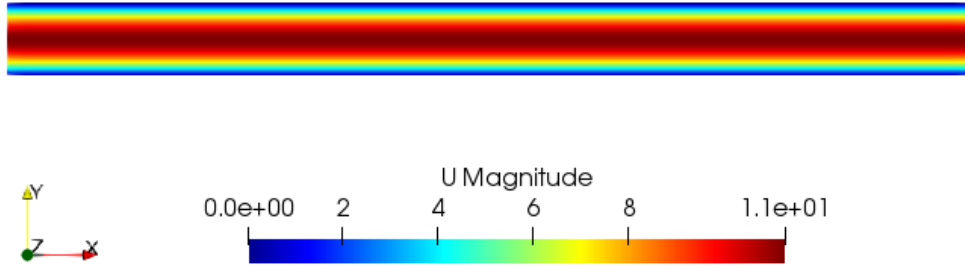


Figure 3.8: Solution of interPhaseChangeFoam

Velocity profiles are showing great resemblance in between and what is also expected from a Poiseuille flow. Figure 3.9 shows the portion of the parabolic velocity profile where the velocity is highest.

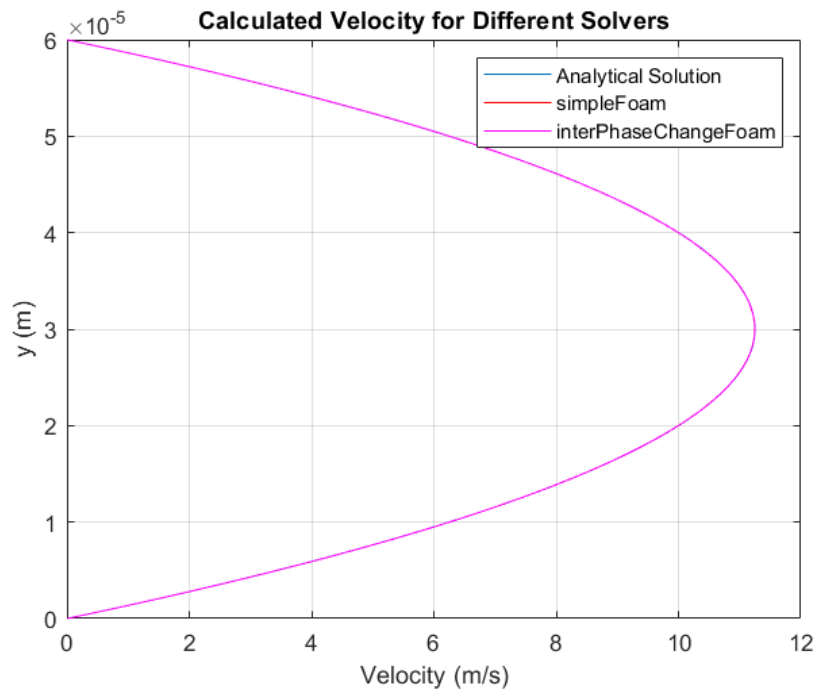
Maximum velocity values and relative error values with respect to analytical solution are tabulated in Table 3.5 for easiness in comparison.

Table 3.3: Maximum Velocity Values Obtained in OpenFoam Solvers and Analytical Solution

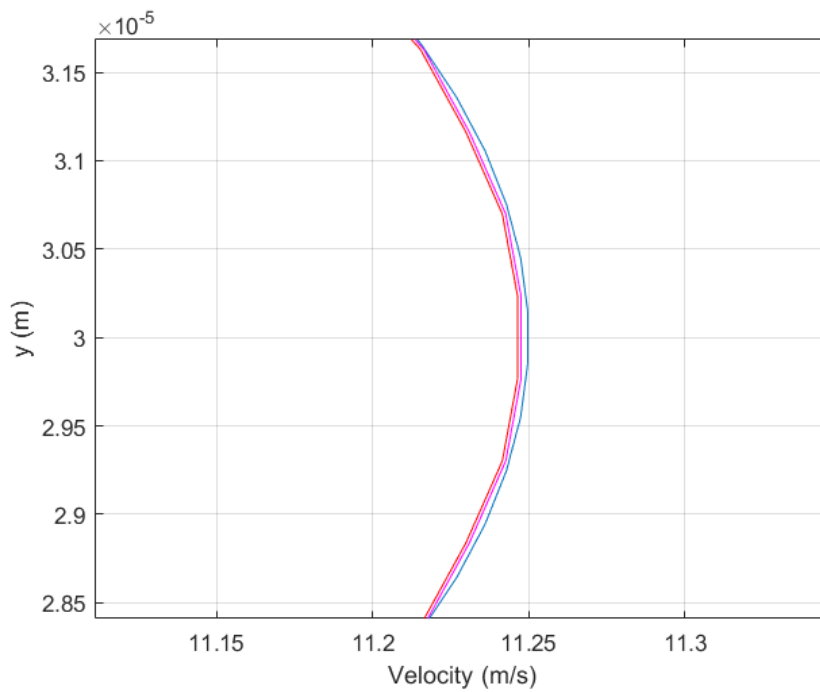
	Maximum Velocity (m/s)	Relative Error (%)
simpleFoam	11.2465	0.02844
pimpleFoam	11.2476	0.01867
interPhaseChangeFoam	11.2476	0.01867
Analytical Solution	11.2497	-

As it is seen, maximum relative error is around %0.03 so it is concluded that the boundary condition implementation for OpenFOAM solvers is correct and settings can be used for pressure and velocity conditions of the multiphase, transient solvers for the rest of this work as it is used here.

Also 2D and 3D simulations were compared to inspect the usability of a 2D simulation for this work. In this manner, a single throttle channel was simulated by using the previous discussed boundary conditions and also with including no slip wall boundary condition (by giving a fixed zero value at the wall in velocity boundary condition). Sectional views at the *vena contracta* location is given in Figure 3.10, to show the effect of no slip walls on the simulation results.

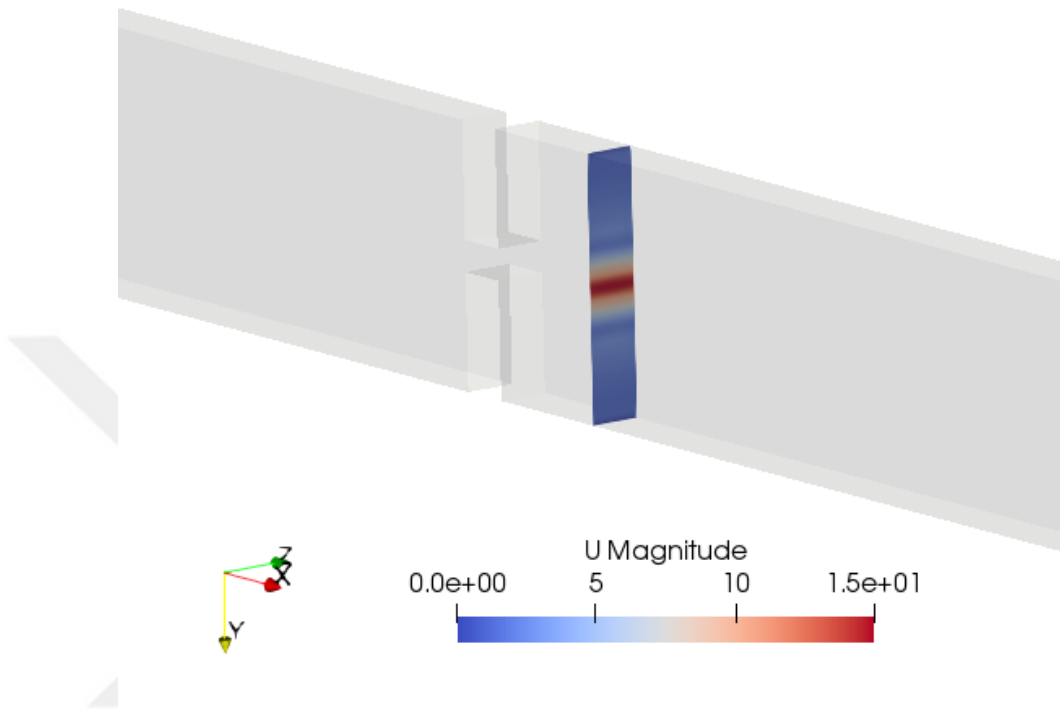


(a) Velocity Profile on the vertical channel centerline

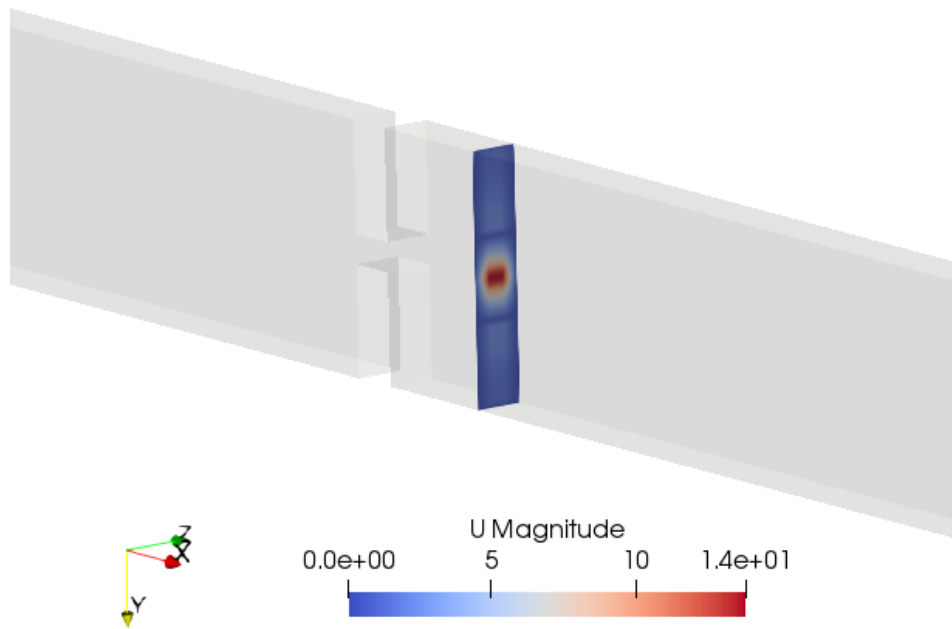


(b) Detailed view of the maximum velocity region

Figure 3.9: Velocity profile of the channel (a) with a detailed view (b)



(a) Velocity Contour at $x=0.00188$ for 2D simulation



(b) Velocity Contour at $x=0.00188$ for 3D simulation

Figure 3.10: Velocity profile of the channel (a) with a detailed view (b)

The effect of no slip boundary condition in the flows can be clearly seen with Figure 3.10. To investigate this effect on physical quantities velocity and pressure values are compared for 2D and 3D simulations. Firstly, the velocity differences at the horizontal centerline of the throttle investigated as Figure 3.11.

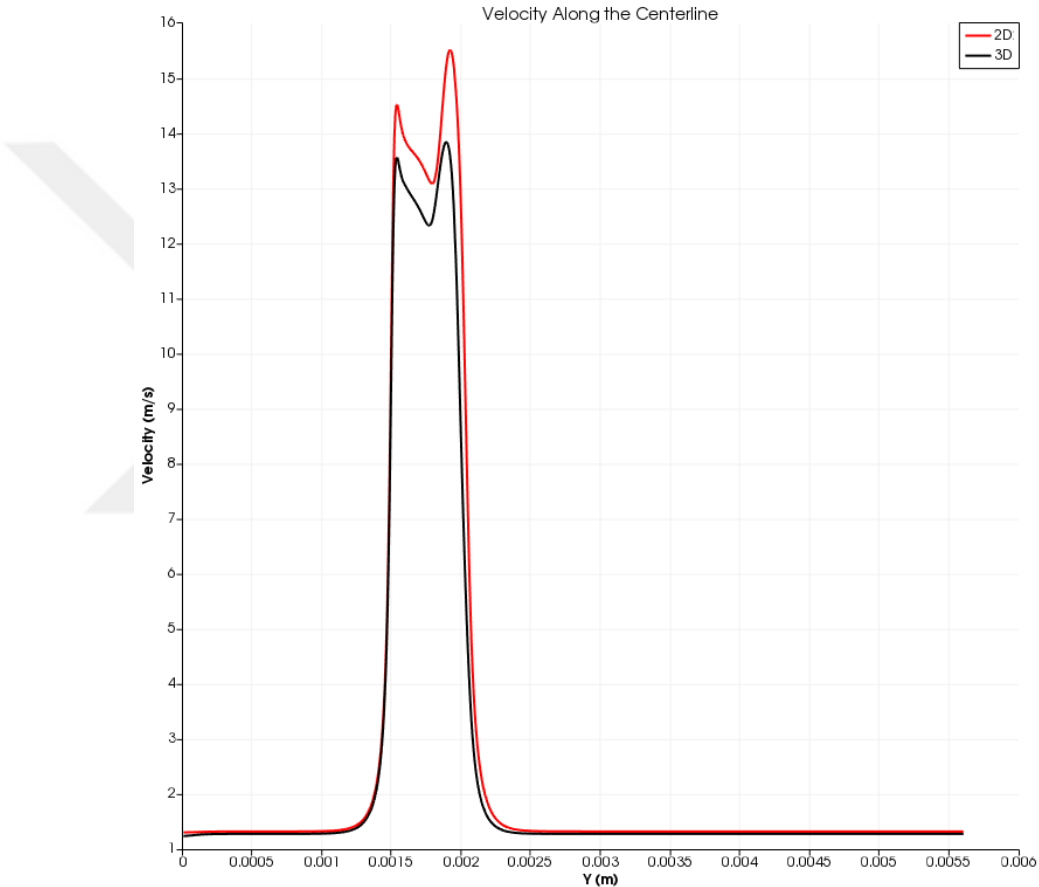


Figure 3.11: Velocity difference 2D and 3D simulations

Maximum difference is obtained as %11 when the highest difference at the pique points are compared. With the same manners, pressure along the channel in the middle section of the channel is compared and given in 3.12.

Difference of the pressure values at their lowest value (in which they differ the most) is calculated as %6.78. Even though the visuals of the contours seem to be different, qualitatively the results are different %11 at maximum. From the pressure graph, it is seen that, lowest pressure point (which is also the highest velocity point) is almost identical, which also shows that *vena contracta* point

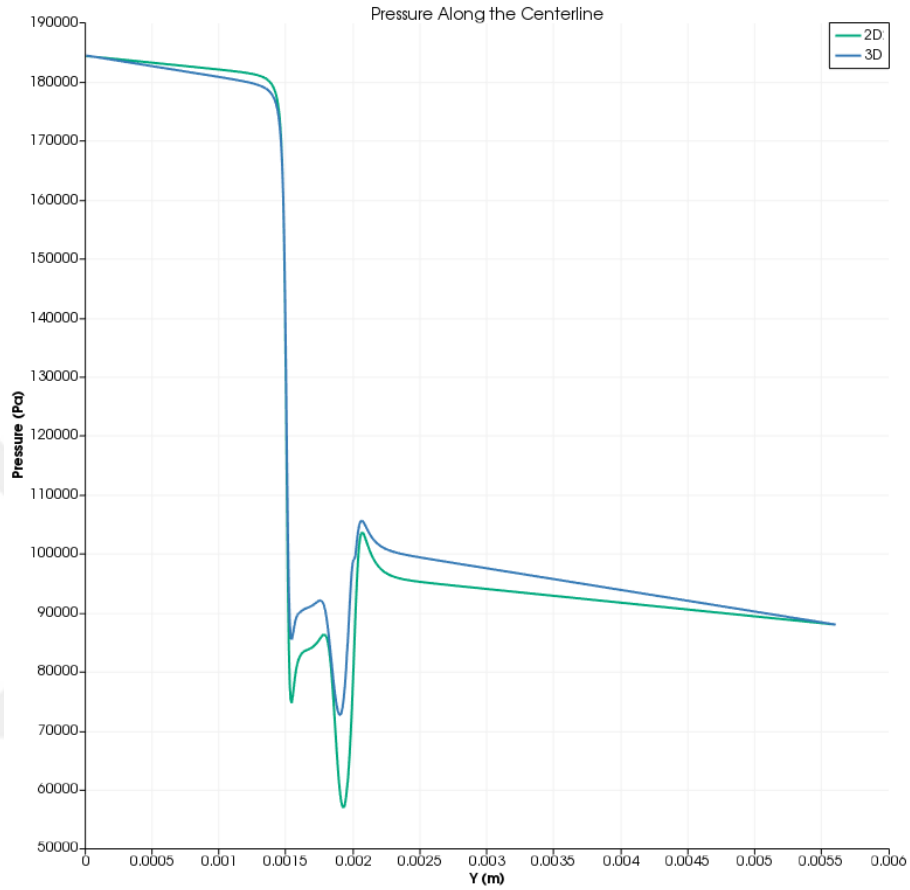


Figure 3.12: Pressure difference in 2D and 3D simulations

does not change. On the other hand, since the purpose of this study is to be able to predict the possible cavitation incidents in quickly on going design processes, the model captures it sufficiently. Also, as 2D model gives higher velocity values, resulting in higher pressure drops, 2D cases can be considered as the worst possible cases at critical cavitation incidents. By adding, the computational time advantages to these facts, 2D simulations are chosen for the rest of this study.

3.2 Geometries

Several different geometries were used for the investigation of cavitation behaviour. Each geometry with their boundary conditions and meshes will be explained in detail throughout this section.

3.2.1 Single Channel Throttle Model and Configurations

A throttle geometry was chosen to model cavitation as shown in Figure 3.13. Geometry of the domain is produced regarding the paper of Medrano et. al. [26]. As a common design in literature validation and verification studies were conducted in this geometry.

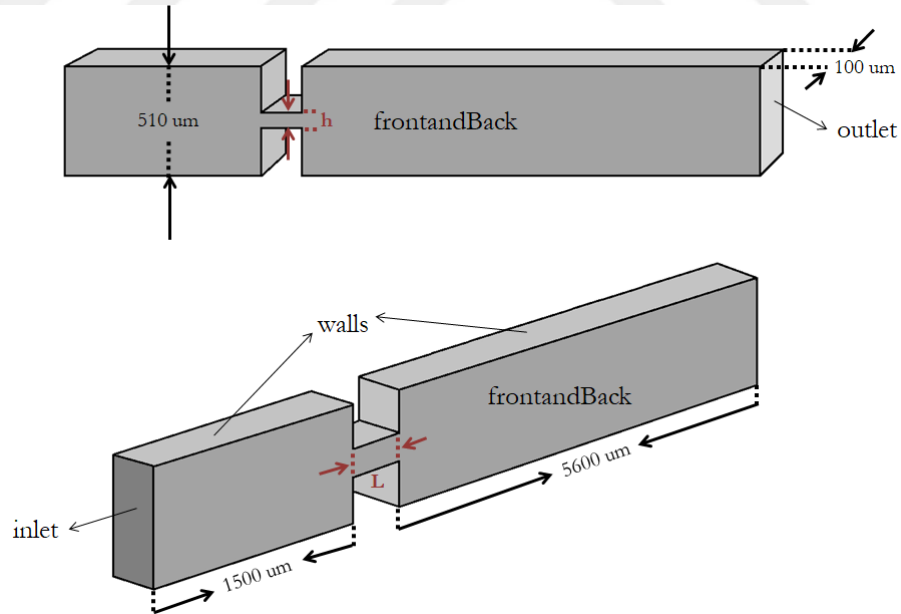


Figure 3.13: Geometry and boundary conditions of throttle configuration

The configuration of this geometry is produced to investigate the effect of aspect ratio. Variations of this geometry is obtained by changing h and L which are also shown in 3.13. All of the configurations and their aspect ratios are given in Table 3.4.

Table 3.4: Configurations of Single Throttle Geometry

Case Number	h (μm)	L (μm)	Aspect Ratio
1	30	100	0.03
2	30	120	0.25
3	30	150	0.20
4	30	200	0.15
5	50	100	0.50
6	50	120	0.42
7	50	150	0.33
8	50	200	0.25
9	60	100	0.60
10	60	120	0.50
11	60	150	0.40
12	60	200	0.30
13	80	100	0.80
14	80	120	0.67
15	80	150	0.53
16	80	200	0.40
17	100	100	1.00
18	100	120	0.83
19	100	150	0.67
20	100	200	0.50
21	120	100	1.20
22	120	120	1.00
23	120	150	0.80
24	120	200	0.60

To eliminate the effects of generated mesh, three different meshes are generated and compared which are all two dimensional. These meshes are shown in Figure 3.14 and their properties are given in Table 3.5. All of the mesh refinements are made with OpenFOAM itself.

Table 3.5: Total cells of the meshes

	Coarse	Middle	Fine
Total Cells	258672	356442	467160
Refinement Level	1	2	3

It is seen that the results do not show a significant change between middle and fine meshes. Axial velocity profile obtained in the middle of the throttle for the meshes are shown in 3.15.

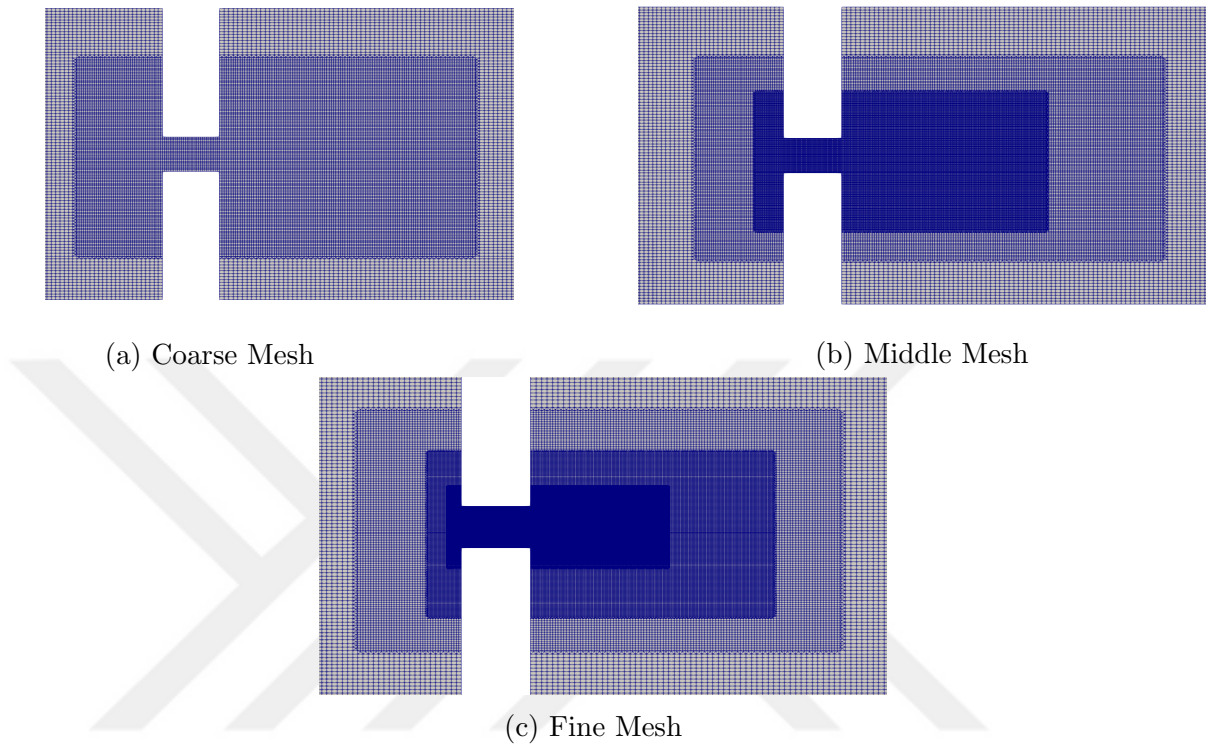


Figure 3.14: a) Coarse, b) Middle and c) Fine meshe sizes created for single throttle configuration

Maximum difference between middle and fine meshes for velocity is calculated as % 0.310. On the other hand between Coarse and Fine meshes this value is obtained as % 1.05. It is also seen from the Figure 3.15 that the Coarse mesh is incapable of resolving the flow near the wall. However by using, the coarse mesh clock time for simulating 1 seconds of the given analysis is around $1.577E^6$ seconds and the same time for middle and fine meshes are $32.72E^6$ and $111.11E^6$ seconds respectively.

Therefore even the lowest cost in terms are obtained in the coarse mesh, optimized accuracy and cost is obtained by middle mesh configuration. So, middle mesh refinement level will be used for the rest of this work. Also, a CPU study was conducted to determine the optimal number of cores for the analysis with the middle mesh. It is seen that CPU time drops around 16 cores and increases above this number of cores. CPU time and core number relation is given in the Figure 3.16 and related values are shown in Table 3.6.

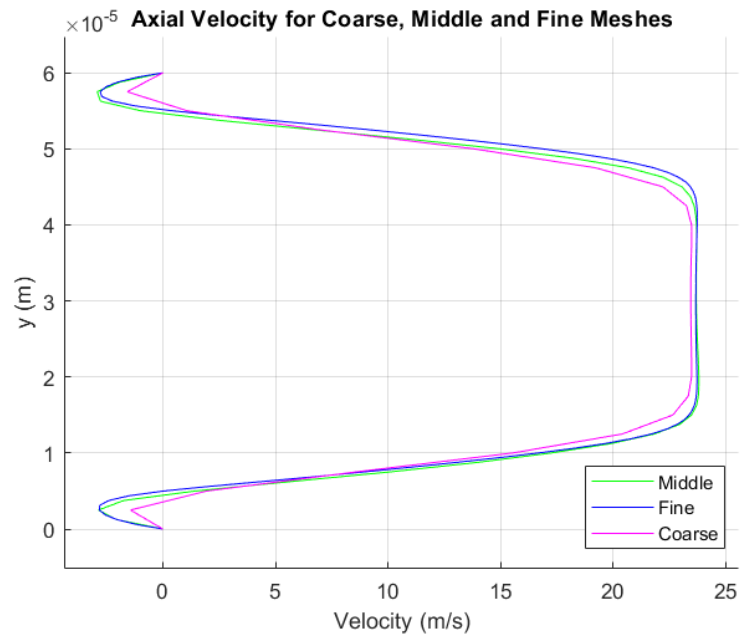


Figure 3.15: Axial velocity profiles for coarse, middle and fine meshes in the throttle

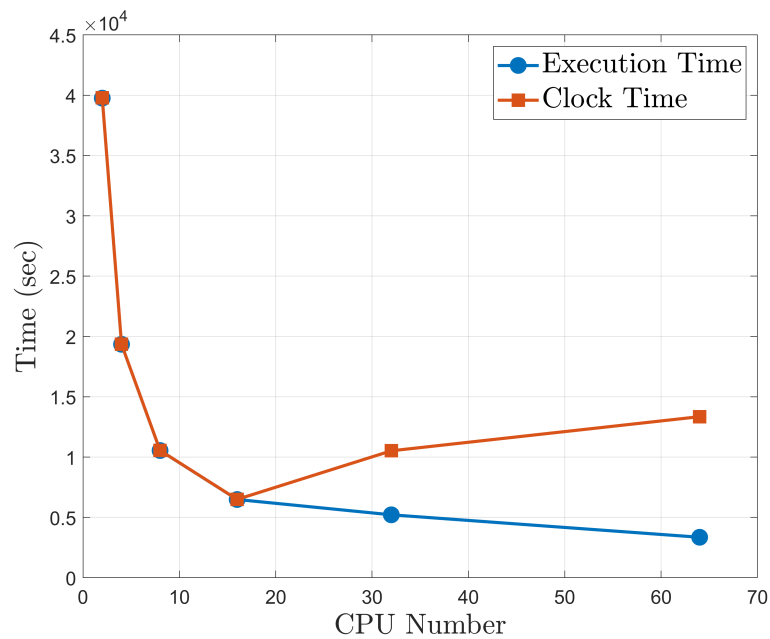


Figure 3.16: Clock time change according to the number of CPU's

Table 3.6: Total cells of the meshes

CPU Number	Execution Time (<i>sec</i>)	Clock Time (<i>sec</i>)
2	39758	39781
4	19350.7	19360
8	10545.6	10552
16	6484.23	6493
32	5214.28	10522
64	3352.93	13352

Regarding these values, for around 35000 cells 16 cores are used both for the throttle geometry and the other geometries which will be described in the upcoming sections of this chapter.

3.2.2 Double Channel Geometry

Regarding the single channel throttle geometry, a double channel geometry was produced for investigation of multiple channel interaction. With this way, interaction of two jets are investigated. Geometry and is shown in Figure 3.17. h is $60 \mu m$ and L is taken as $100 \mu m$.

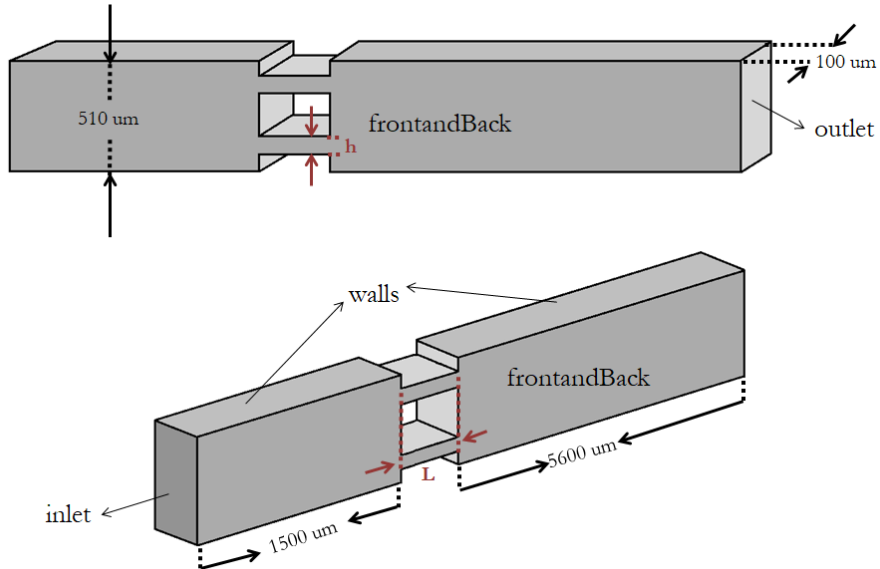


Figure 3.17: Geometry and boundary conditions of double throttle channel geometry

A grid with 2 levels of mesh refinement is again used. Produced mesh and its size is given in 3.18.

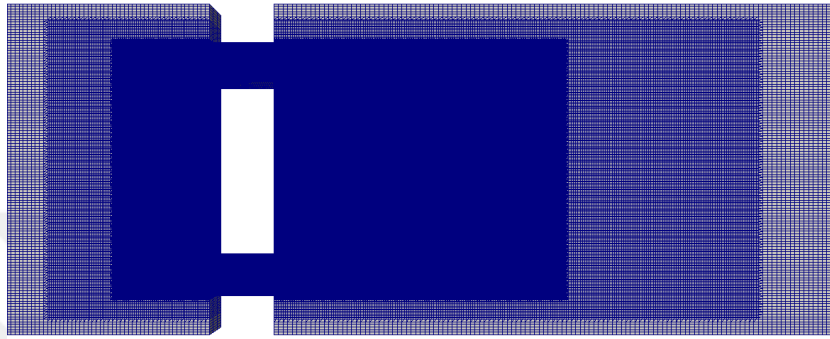


Figure 3.18: Grid of the double throttle channel geometry

3.2.3 Triple Channel Geometry

In addition to the double channel geometry, a triple channel geometry was investigated too. This geometry and its dimensions are shown in Figure 3.19.

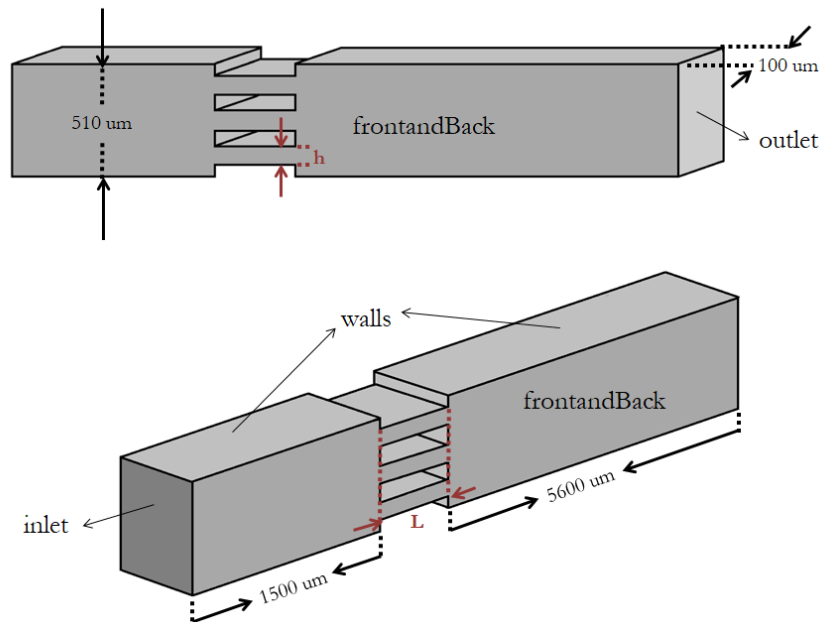


Figure 3.19: Geometry and boundary conditions of triple channel geometry

The main consideration for designing this channel is to see the cavitation behaviour when there are multiple jets that interact each other inspired from the geometry of the Schneider et al. [18]. In other words to see the effect of increasing channel numbers. A grid with 2 levels of mesh refinement is again used. Produced mesh and its size is given in 3.20.

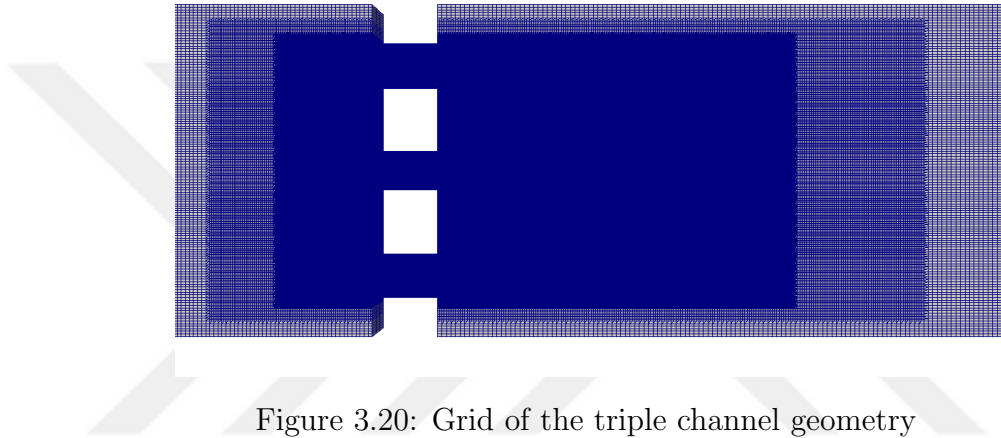


Figure 3.20: Grid of the triple channel geometry

3.2.4 Nozzle Inspired Channel Geometry

3.2.4.1 Smaller to Larger Cross Section

To see the effect of changing cross sectional area in the throttle part, a nozzle inspired geometry was produced. With this way the aim is to see the the effect of varying inlet and outlet area. Dimensions and the geometry are shown in Table 3.7 and Figure 3.21, respectively.

Table 3.7: Dimensions of the Geometry

	Dimensions (μm)
he	162
hi	60
w	225
a	174

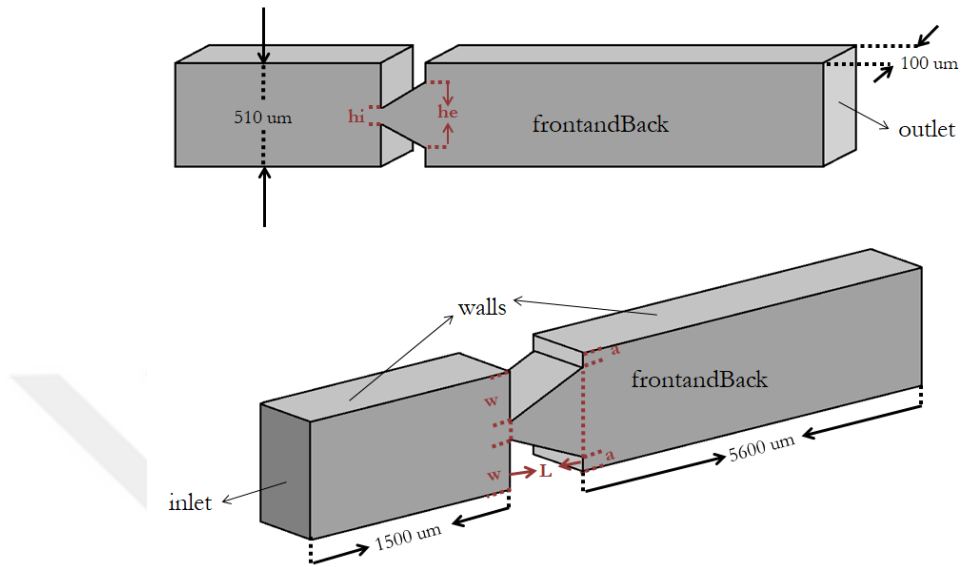


Figure 3.21: Geometry and boundary conditions of nozzle inspired channel geometry

A grid with 2 levels of mesh refinement is again used. Produced mesh and its size is given in 3.22.

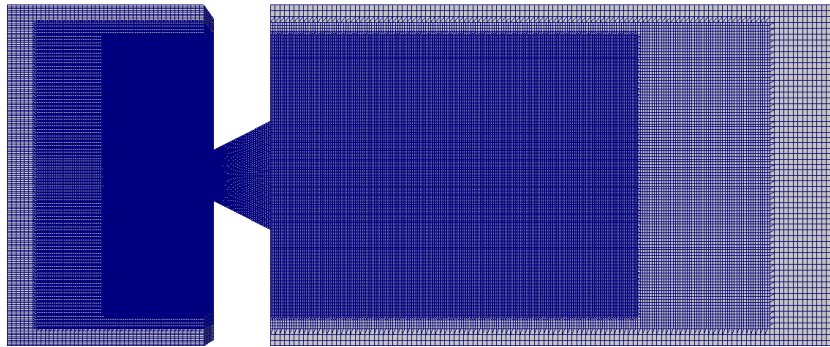


Figure 3.22: Grid of the nozzle type channel geometry

3.2.4.2 Larger to Smaller Cross Section

Regarding the previous geometry, a geometry having a larger cross section than its outlet is formed basically by reversing the one shown in 3.21. Since it has the same dimensions of the previous section, grid was kept constant.

3.2.5 Double Inclined Geometry

3.2.5.1 Smaller to Larger Cross Section

Another design was created with double inclined channels. The main aim of this geometry to investigate the non-parallel jet interactions unlike the others. Created geometry is shown in Figure 3.23.

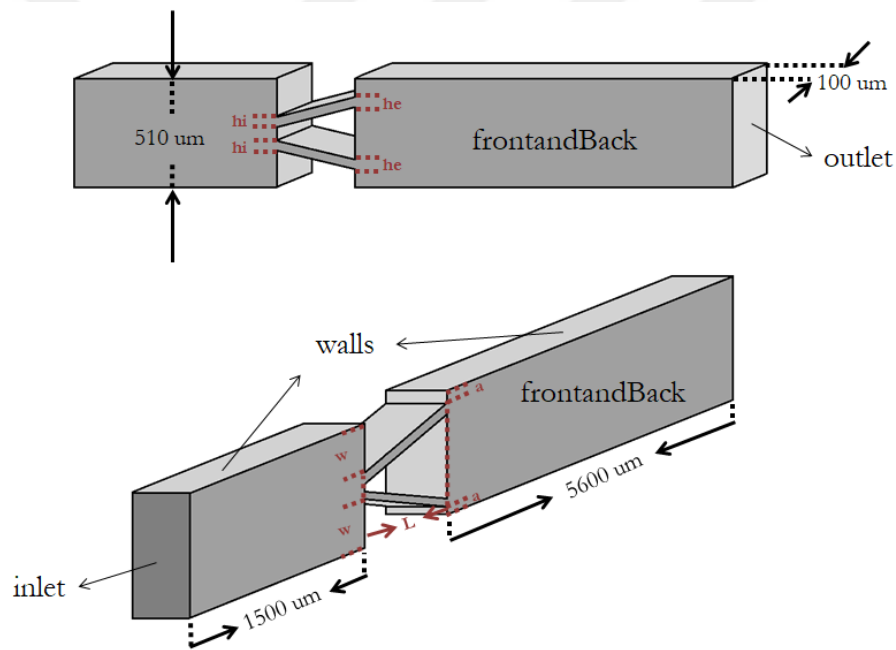


Figure 3.23: Geometry and boundary conditions double inclined channel geometry

Dimensions labelled in 3.23 are given in Table 3.8.

Table 3.8: Dimensions of the Geometry

	Dimensions (μm)
he	60
hi	60
w	143.9
a	60

Generated grid for this geometry is given in Figure 3.24

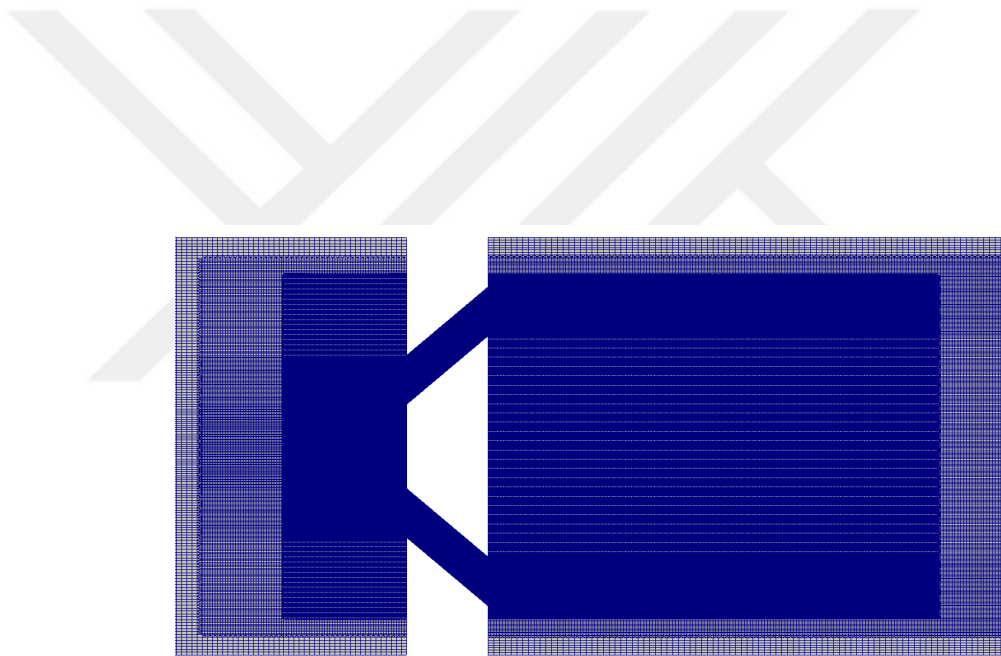


Figure 3.24: Grid of the double inclined channel geometry

Chapter 4

Calculations and Simulation Results

In this section, CFD results of the cavitation simulations with the previously discussed geometries and their related computations are given to investigate the behavior of cavitating flows. Several different coefficients and parameters critical for cavitation such as discharge coefficient and cavitation number are calculated as part of the investigation. With each geometry, analysis methodology proposed in Chapter 3 was used with 6 different input total pressure values given in 2.3. Used values are shown in Table 4.1.

Table 4.1: Measured Properties in the Set-up

Input Pressure at Point 1 (Pa)	Flow Rate (m^3/s)	Velocity (m/s)	Total Pressure (Pa)
100000	1.779e-08	0.3351	185250.019
200000	3.018e-08	0.5684	281283.118
300000	4.112e-08	0.7744	377825.604
400000	5.120e-08	0.9643	474677.594
500000	6.069e-08	1.1432	571746.932
600000	6.975e-08	1.3137	668978.537

4.1 Single Channel Throttle Geometry

In this section firstly the flow coefficients will be discussed then simulation results will be presented.

4.1.1 Coefficient Calculations

Several calculations and steps are taken in order to characterize the flow. As a result of these calculations; vena contracta location, contraction, velocity and discharge coefficients are obtained.

Vena Contracta

There are different parameters that defines the behavior of cavitating flows. As a start, *vena contracta* location is found. *Vena contracta* is described as the location with jets smallest area, highest velocity and the lowest pressure [39,40]. It shows Representation of the *vena contracta* is shown in Figure 4.1 below.

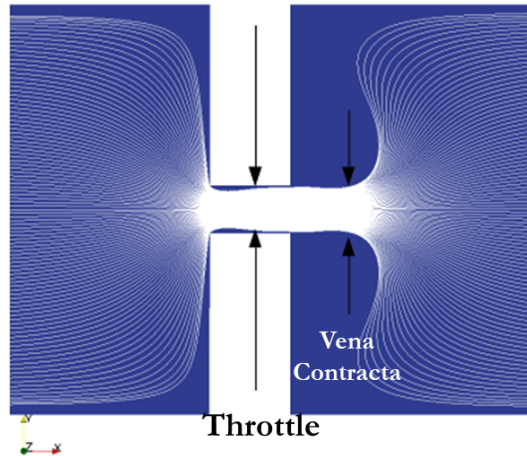
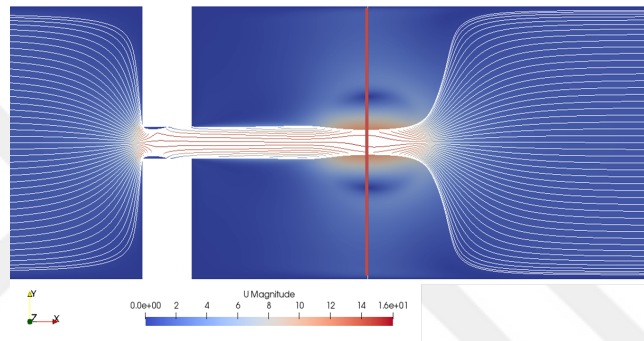


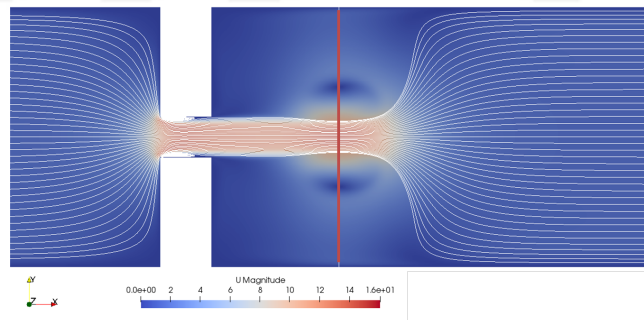
Figure 4.1: Representation of Vena Contracta

Position of *vena contracta* shows variety for different channel widths and lengths. In this manner 4.2 shows the change of the location with respect to

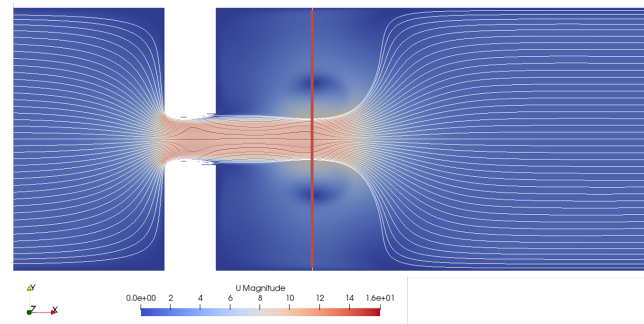
increasing channel width for same Reynolds number. Also the effect of the channel length is shown in 4.3. Two parameters are generated for these investigations which are β as the ratio between the width of the throttle and the channel ($\beta = h/510$) and A as the aspect ratio of the throttle ($A = h/L$). Since the location of *vena contracta* is related to the geometry, different flow rates are not investigated.



(a) Throttle with $\beta = 0,12$ and $A=0,6$

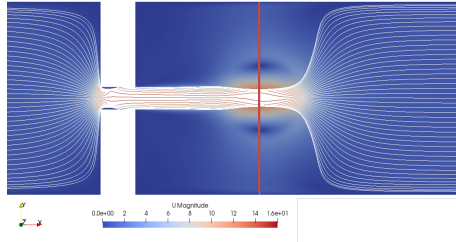


(b) Throttle with $\beta = 0,16$ and $A=0,8$

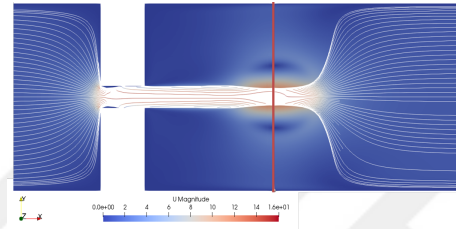


(c) Throttle with $\beta = 0,20$ and $A=1,0$

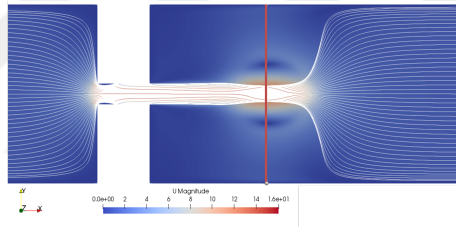
Figure 4.2: Location of *vena contracta* for different channel types) a) $\beta = 0,12$ and $A=0,6$, b) $\beta = 0,16$ and $A=0,8$ and c) $\beta = 0,20$ and $A=1,0$



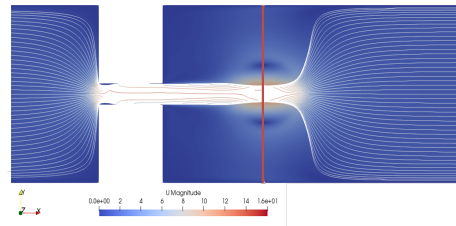
(a) Throttle with $\beta = 0, 12$ and $A=0,6$



(b) Throttle with $\beta = 0, 12$ and $A=0,5$



(c) Throttle with $\beta = 0, 12$ and $A=0,4$

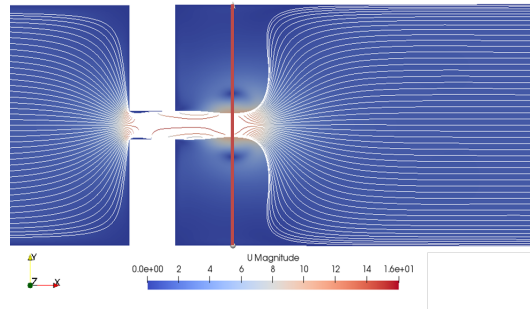


(d) Throttle with $\beta = 0, 12$ and $A=0,3$

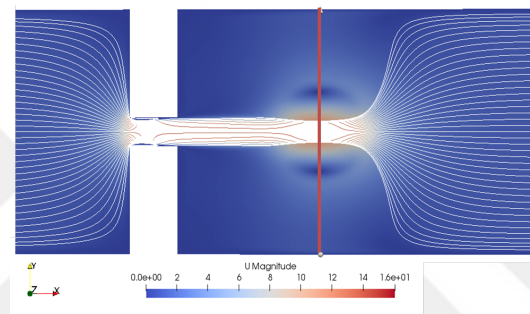
Figure 4.3: Location of *vena contracta* for different channel types) a) $\beta = 0, 12$ and $A=0,6$, b) $\beta = 0, 12$ and $A=0,5$ and c) $\beta = 0, 12$ and $A=0,4$ d) $\beta = 0, 12$ and $A=0,3$

As it is seen in Figure 4.2 and 4.3, channel width is the main driving parameter of channel geometries and on the contrary, channel length has no effect on the location of *vena contracta*.

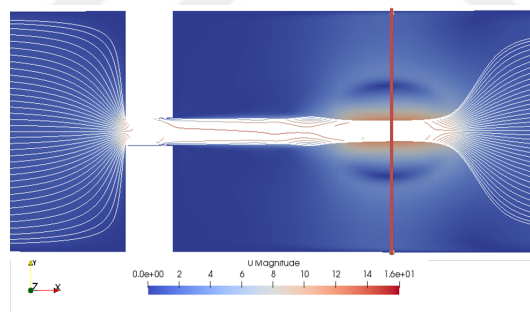
Effect of the Reynolds number for the same channels are also investigated. Figure 4.4 shows the behaviour of *vena contracta* location with respect to Reynolds number for channel with $60 \mu m$ width.



(a) $Re=25$



(b) $Re=43$



(c) $Re=58$

Figure 4.4: Location of *vena contracta* for different Reynolds numbers a) $Re=25$ b) $Re=42.6$ and c) $Re=58$

Contraction Coefficient

Contraction coefficient is a parameter to express the relation between the orifice geometry and the flow of the orifice. It is defined as the ratio between the areas of the flow at vena contracta to the area of the channel. Equation 4.1.1 shows this relation between channel width and vena contracta [41].

$$C_c = \frac{\text{Area of the flow at vena contracta}}{\text{Area of the channel}} \quad (4.1.1.1)$$

As both the area of the flow at *vena contracta* and channel width showed variety, contraction coefficient differs with respect to channel area. Results for channels are given with respect to the square root of Reynolds Number in the Figure 4.5.

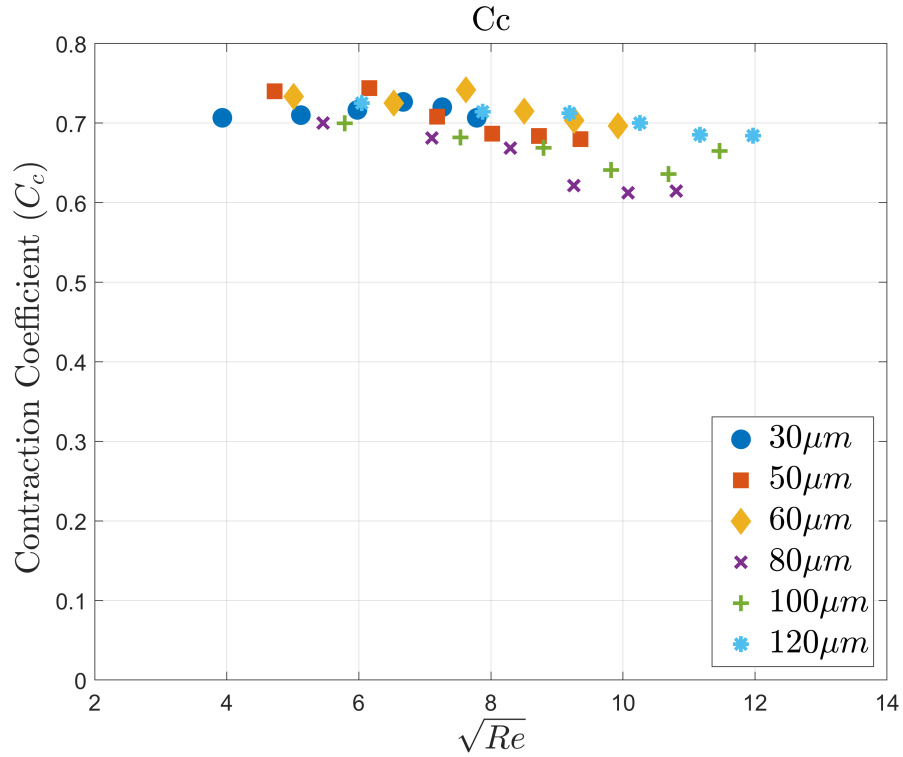


Figure 4.5: Contraction Coefficient with respect to the Square Root of Reynolds number

Tabulated results are given in Table 4.2.

Table 4.2: Contraction Coefficient Results for single throttle geometry

Input Pressure (Pa)	30	50	60	80	100	120	Average
100000	0.707	0.740	0.733	0.700	0.700	0.725	0.717
200000	0.710	0.744	0.725	0.681	0.682	0.714	0.709
300000	0.717	0.708	0.742	0.669	0.669	0.713	0.703
400000	0.727	0.687	0.715	0.621	0.641	0.700	0.682
500000	0.720	0.684	0.703	0.613	0.636	0.685	0.674
600000	0.707	0.680	0.697	0.615	0.665	0.684	0.675
Average	0.716	0.713	0.724	0.657	0.707	0.684	

Average value is around 0.7 for the contraction coefficient and it can be concluded that as the pressure at the inlet increases contraction coefficient is decreasing.

Discharge Coefficient

Discharge coefficient is defined as the ratio between actual flowrate of a throttle to the theoretical one [42]. There are several different ways to calculate it, for common type of valves, orifices etc. it is pre-determined by experiments [42, 43].

From the definition the relation between the coefficients are stated as follows [42];

$$Q = AV = C_c C_v A_0 V_i = C_d A_0 V_i \quad (4.1.1.2)$$

where A is the area of vena contracta, A_0 is the area of the throttle and V_i is the velocity at *vena contracta*. However, there are other methods for determining the discharge coefficient. It is driven from the Bernoulli equation its relation to the flow rate is written as [26];

$$P_{in} - P_{out} = \frac{24\mu L}{WH^3} \left(1 + \frac{H}{W}\right)^2 Q + \frac{\rho}{2C_d^2} \frac{Q^2}{h^2 H^2} \quad (4.1.1.3)$$

where H is is depth, h is throttle width, L is the length and W is the width of the

entrance section, Q is the flow rate and C_d is the discharge coefficient. However, this equation does not satisfy certain conditions.

Then the relation regarding the discharge coefficient is simplified to the following Equation 4.1.1 [26];

$$\frac{1}{C_d} = \frac{1}{C_c} - \frac{h}{W} \quad (4.1.1.4)$$

However, this equation does not satisfy conditions. As Reynolds Number gets smaller, effect of the viscous forces gets dominant and the previous equations can not model it [44, 45]. For those cases, in his book H.E. Merritt tabulates the discharge coefficients of short tube orifices as follows; For $\frac{D_h Re}{L} > 50$

$$C_d = [1.5 + 13.74(L/DR)^{\frac{1}{2}}]^{-\frac{1}{2}} \quad (4.1.1.5)$$

For $\frac{D_h Re}{L} < 50$

$$C_d = [2.28 + 64(L/DR)]^{-\frac{1}{2}} \quad (4.1.1.6)$$

For lower Reynolds numbers such as $Re < 10$ equation can be directly written as a function of Reynolds Number;

$$C_d = \delta Re^{\frac{1}{2}} \quad (4.1.1.7)$$

where δ is laminar flow coefficient related to the geometry. In addition to this one, Wu et. al. successfully derived the equation in terms of Reynolds Number for higher Reynolds Numbers too. The equation is given in 4.1.1 [46].

$$C_d = 0.61(1 + 1.07e^{-0.126\sqrt{Re}} - 2.07e^{-0.246\sqrt{Re}}) \quad (4.1.1.8)$$

For those purposes, Reynolds Numbers for the single throttle channel geometries is given in Table B.0.3 in Appendix B.0.3. Discharge coefficient results obtained from the simulations are given in 4.6.

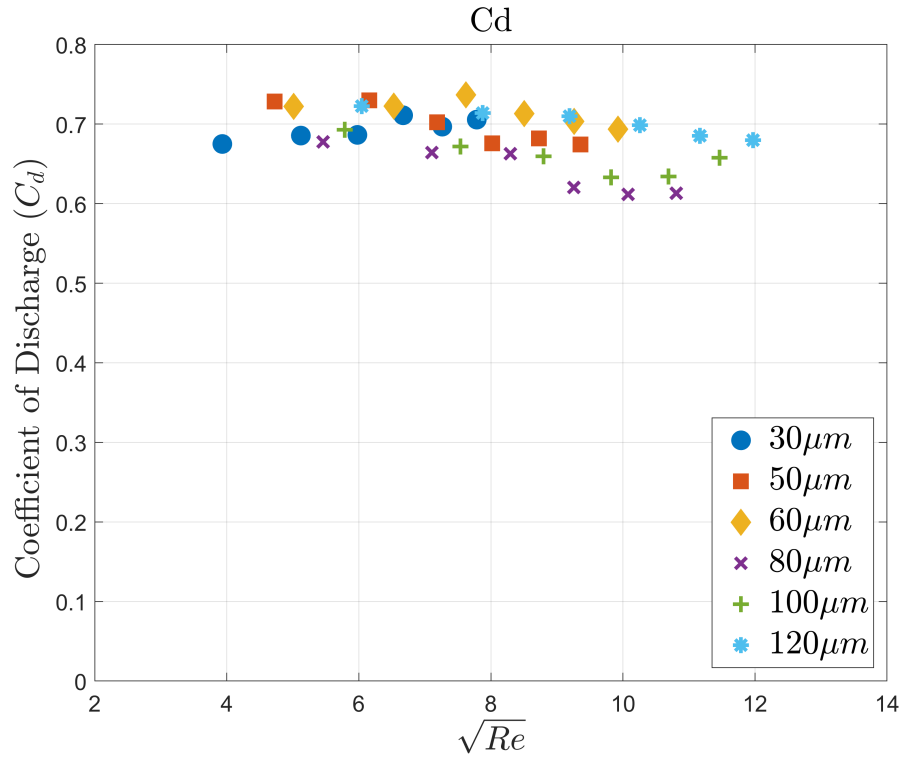


Figure 4.6: Discharge Coefficient with respect to the Square Root of Reynolds number

These results are then compared with the values obtained from equation that Wu et. al. derived. Results of channels with with of 30, 80 and 120 μm are given in 4.7, 4.8 and 4.9. Results of other channels are given in B.0.1. Even though the values are clustered in a small range, it is observed that as the Reynolds numbers increase the values are decreasing.

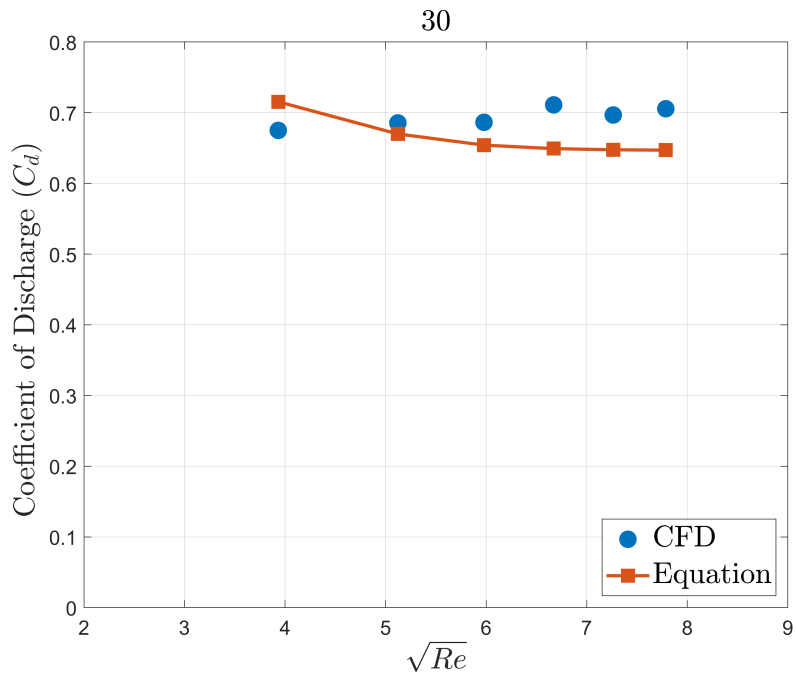


Figure 4.7: Discharge Coefficient of $\beta=0,06$ and $A=0,3$

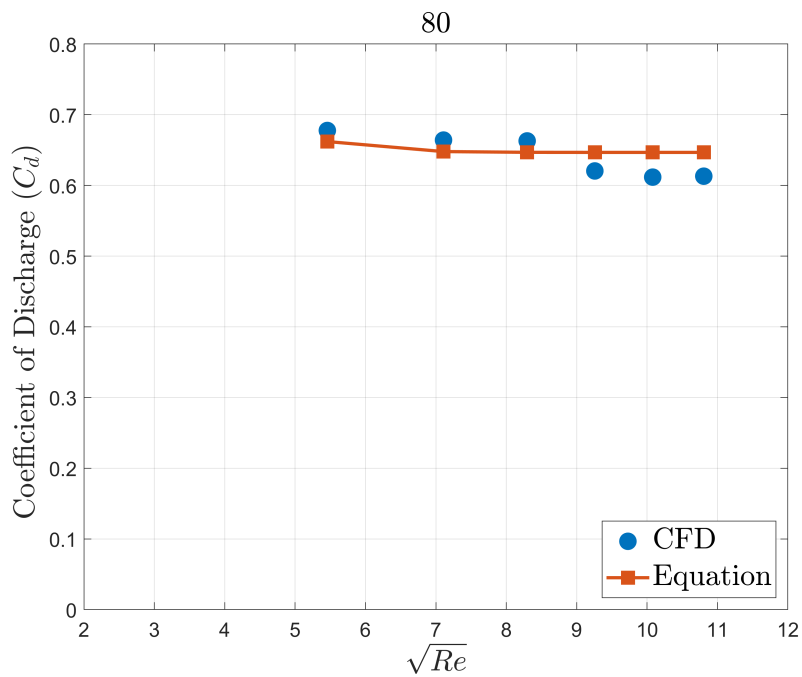


Figure 4.8: Discharge Coefficient of $\beta=0,16$ and $A=0,8$

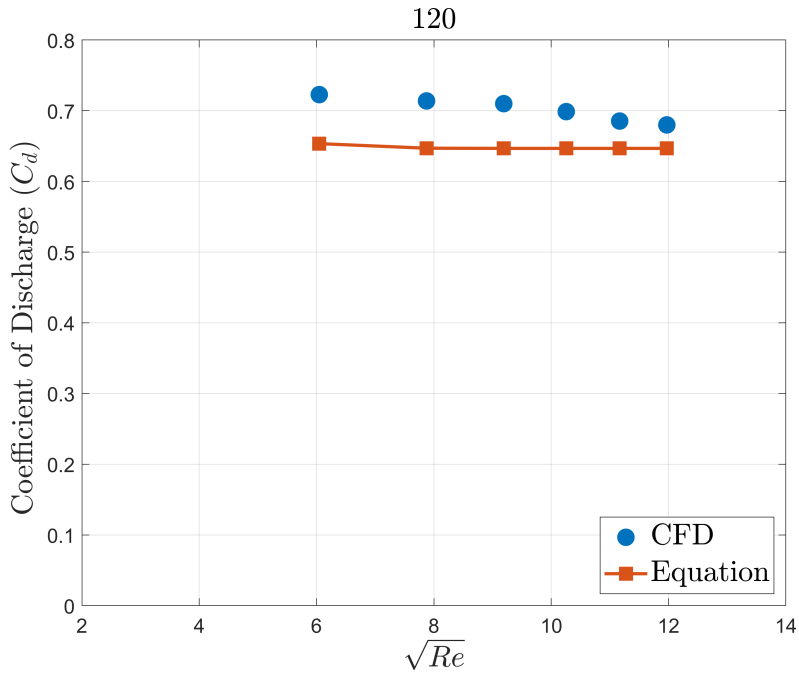


Figure 4.9: Discharge Coefficient of $\beta=0,24$ and $A=1,2$

Percentage errors are calculated between the equation of Wu et. al. [46] and CFD simulations. The results are given in Figure 4.10. It is seen that the lowest error value is obtained for $100 \mu m$ width channel. In terms of the input pressures lowest error values are obtained for 5 and 6 bar simulations. Table 4.3 provides values for each case.

Table 4.3: Percentage Errors for Discharge Coefficient in Single Channel Geometry

Input Pressure (Pa)	30	50	60	80	100	120	Average
100000	5.654	6.705	7.304	2.364	5.517	10.611	6.359
200000	2.330	11.863	11.191	2.508	3.829	10.333	7.009
300000	4.937	8.442	13.833	2.493	1.988	9.785	6.913
400000	9.531	4.486	10.253	4.057	2.088	8.042	6.410
500000	7.600	5.447	8.738	5.409	1.927	5.980	5.850
600000	9.056	4.276	7.260	5.202	1.706	5.139	5.440
Average	6.518	6.870	9.763	3.672	2.843	8.315	

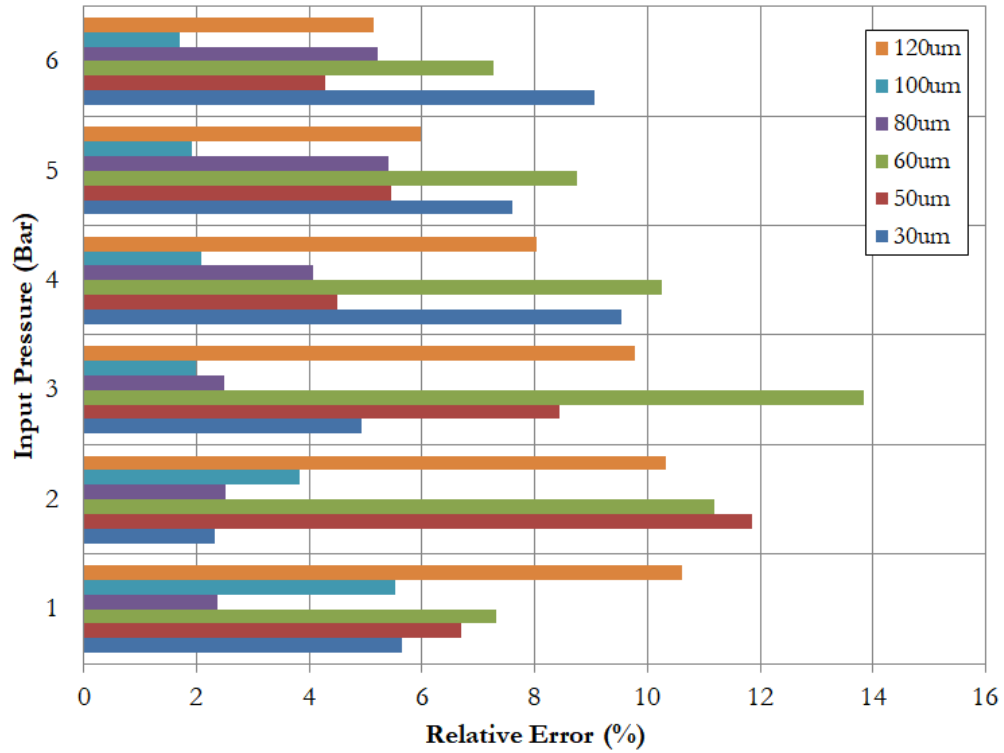


Figure 4.10: Percentage Error in Discharge Coefficient calculations

Velocity Coefficient

After the calculations of contraction and discharge coefficients velocity coefficient is calculated from the definition. Obtained results are given in Figure 4.11.

It is observed that as the Reynolds numbers increase the values are clustering near 1, yet the maximum coefficient calculated is 0.99 at most. Besides coefficients several different aspects in the design of throttle are investigated. These will be discussed in the upcoming sections.

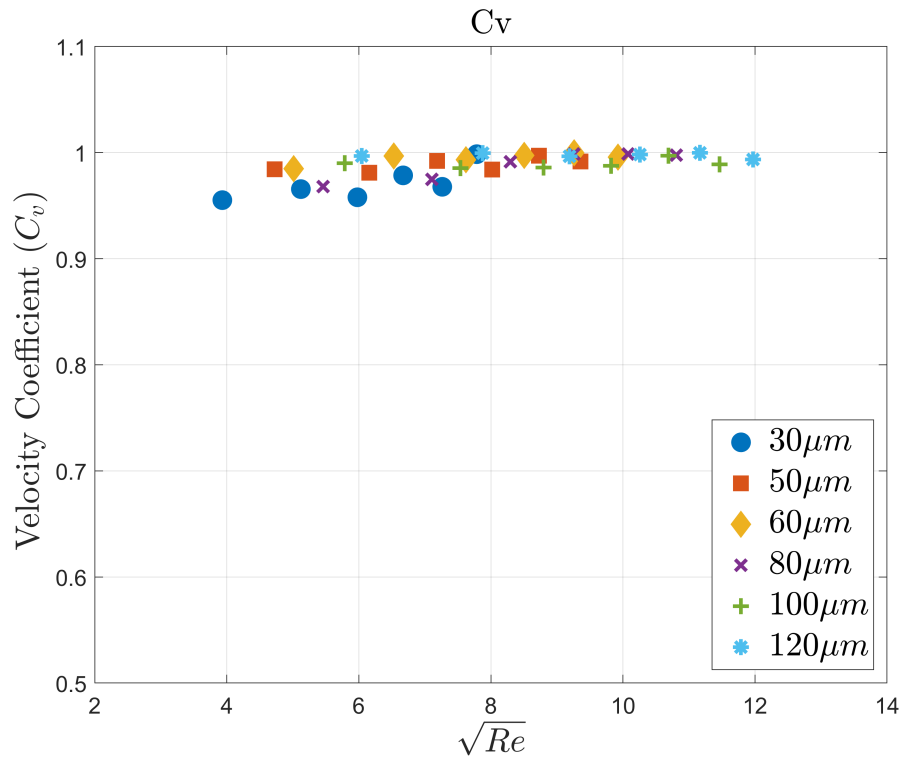


Figure 4.11: Velocity coefficient results for single channel Geometry

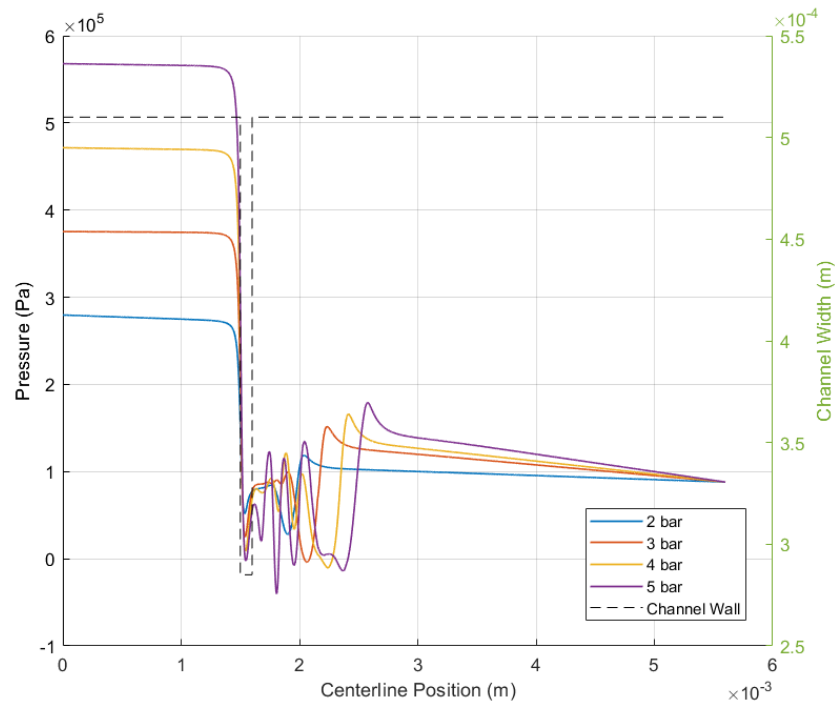
4.1.2 Effect of Input Pressure

As it is discussed previously, variation in input pressure changes the location of vena contracta, this effect can also be seen from the change in pressure along the center line of the channel. This effect is shown in Figure 4.12. Velocity graph along the same center line is given in B.0.2.

Location of the lowest pressure point also affects the phase change. Alpha contour of the channel with 60 width in Figure 4.13 shows the variation in the formation of bubbles in different input pressure values (ratio of fluid volumes as 1 being incompressible and 0 being compressible).



(a) Place of the centerline



(b) Pressure Changes for different channel thicknesses

Figure 4.12: Pressure change along the channel at $t=0.00013s$ for different inlet pressures

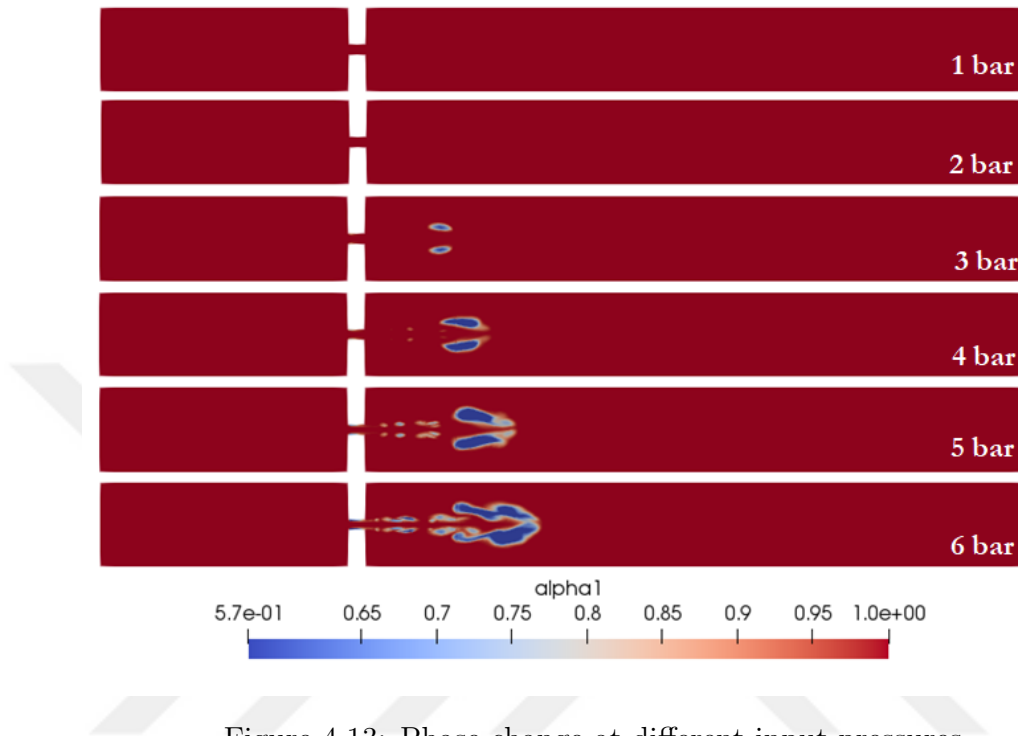


Figure 4.13: Phase change at different input pressures

4.1.3 Effect of Channel Thickness

To investigate the effect of channel thickness in cavitating flows, firstly the pressure change over the channel is investigated. For the same time step and same inlet total pressures, 4.14 shows the difference in pressure change over the center line of the channel.

When channel thickness is changed the alpha contour varies as it is shown in Figure 4.15 for a given inlet pressure of 3 bars. As the thickness increases, the time that vapour bubble forms changes regarding the velocity and pressure drop. However, decreasing it too much will also increase the friction losses. Therefore at 50 and 60 μm channels vapor bubbles tend to occur faster.

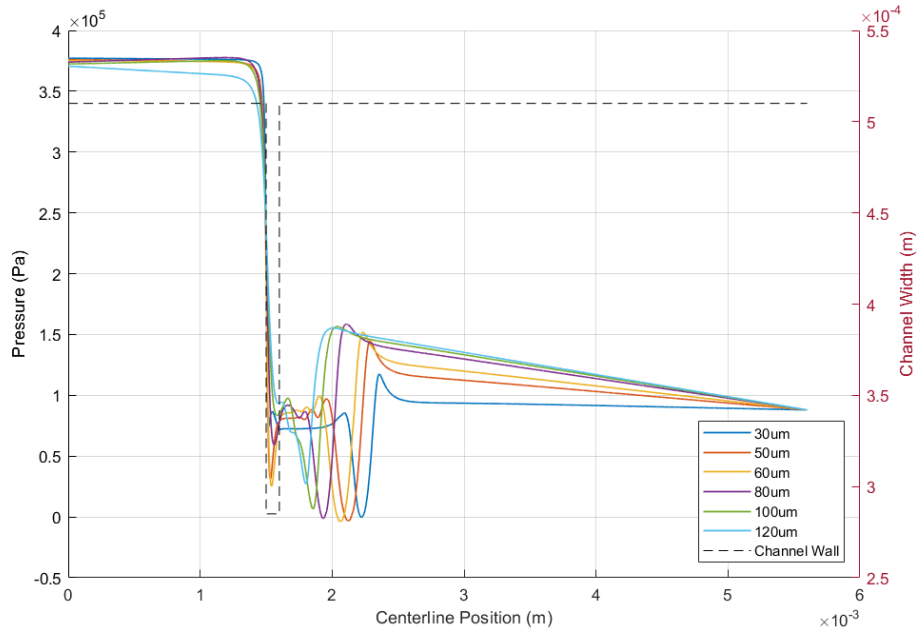


Figure 4.14: Representation of the Flow in the Experimental Set-up

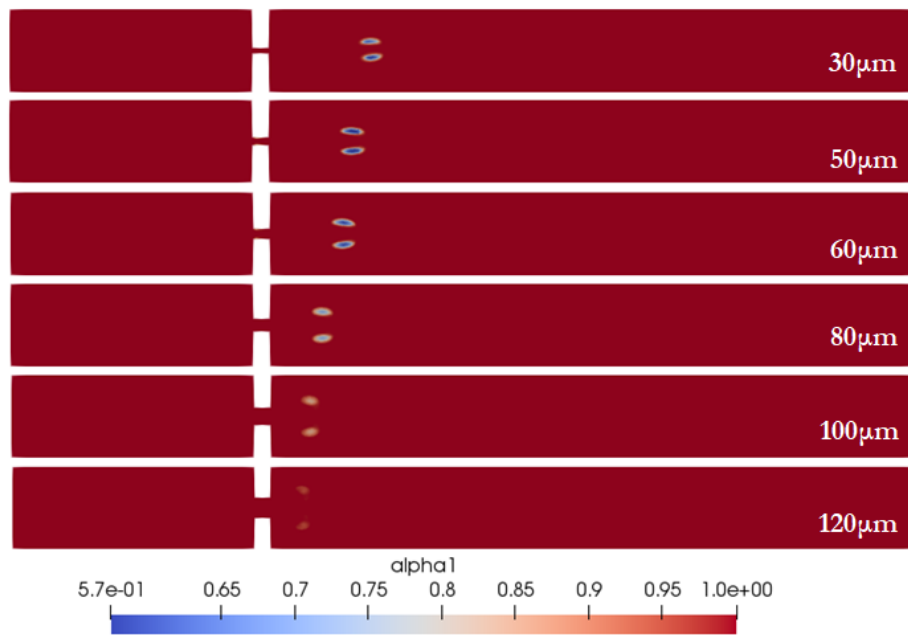


Figure 4.15: Alpha Contour at $t=0.00013$ for Different Channel types

4.2 Double Channel Geometry

Double channel geometry is created by multiplying a single channel. Jets created for each channel is identical with the single channel geometry until they collide with each other. After the interaction flow becomes completely chaotic. In this manner, velocity contour changing with respect to time is given in Figure 4.16 for the simulations with inlet pressure of 3 Bar. Pressure contour is given in Section B.0.4.1.

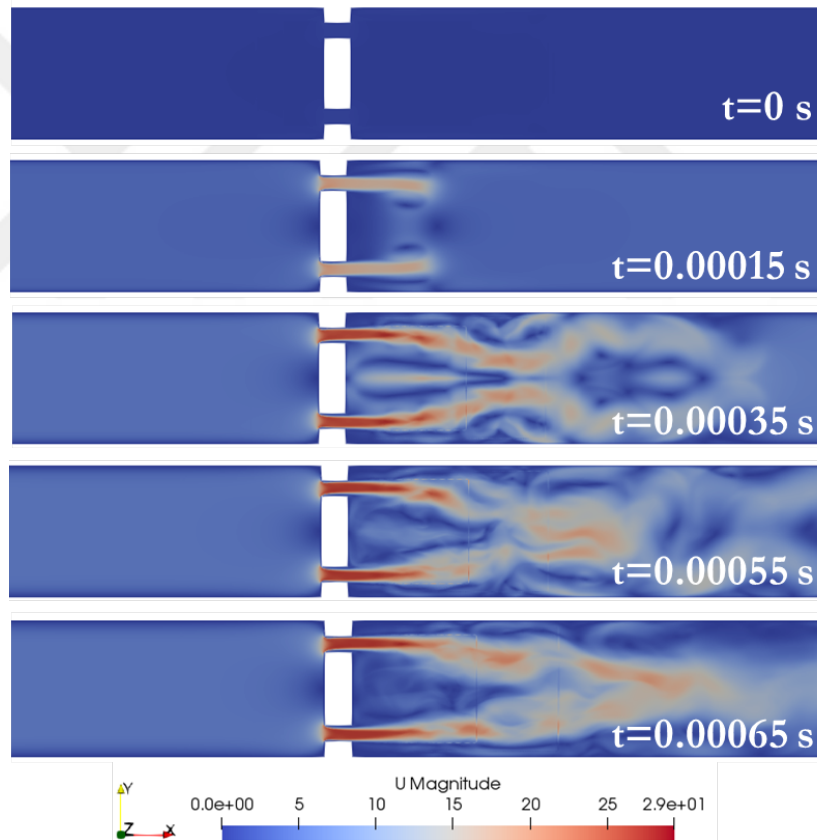


Figure 4.16: Velocity Contour with Respect to Time for Double Channel Geometry

As it is seen, flow is symmetrical since jets are not interacting with each other at $t=0.00035$ s. Then when two jets interact with each other flow pattern becomes random and chaotic as it is expected

Pressure drop along the center line of each channel is investigated for the 0.0005 second. Before any disturbance all pressure variations are equal. At 0.0005 however, jets start to collide and create chaotic variations.

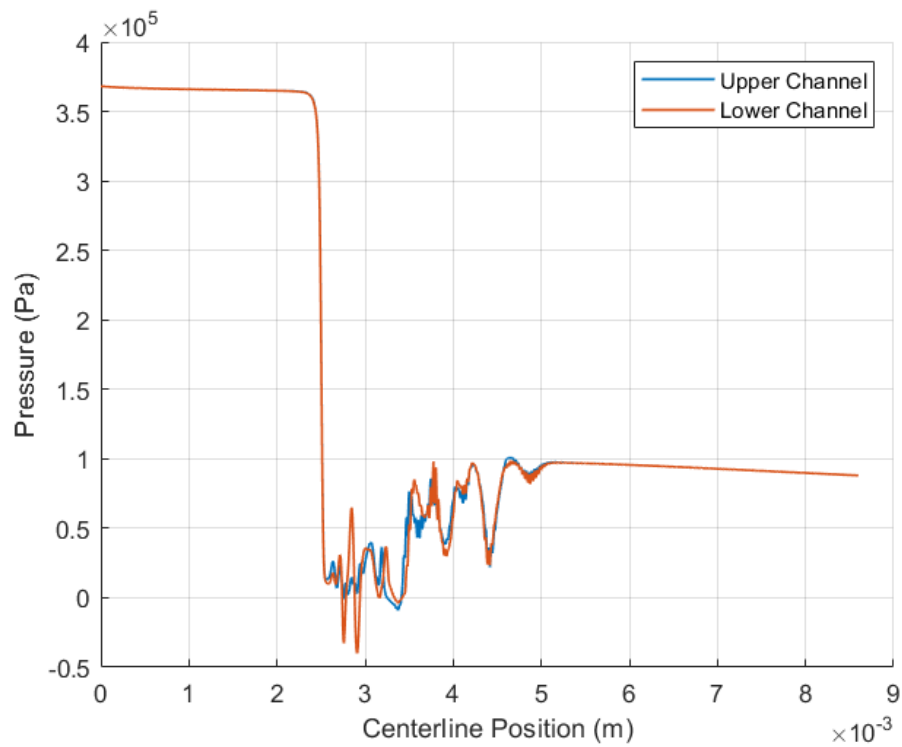


Figure 4.17: Pressure Change in Channels in Double Channel Geometry

Bubbles on the other hand starts to occur before that time since the pressure drop reaches below the vapor pressure beforehand. Related alpha contour is given in Figure 4.18.

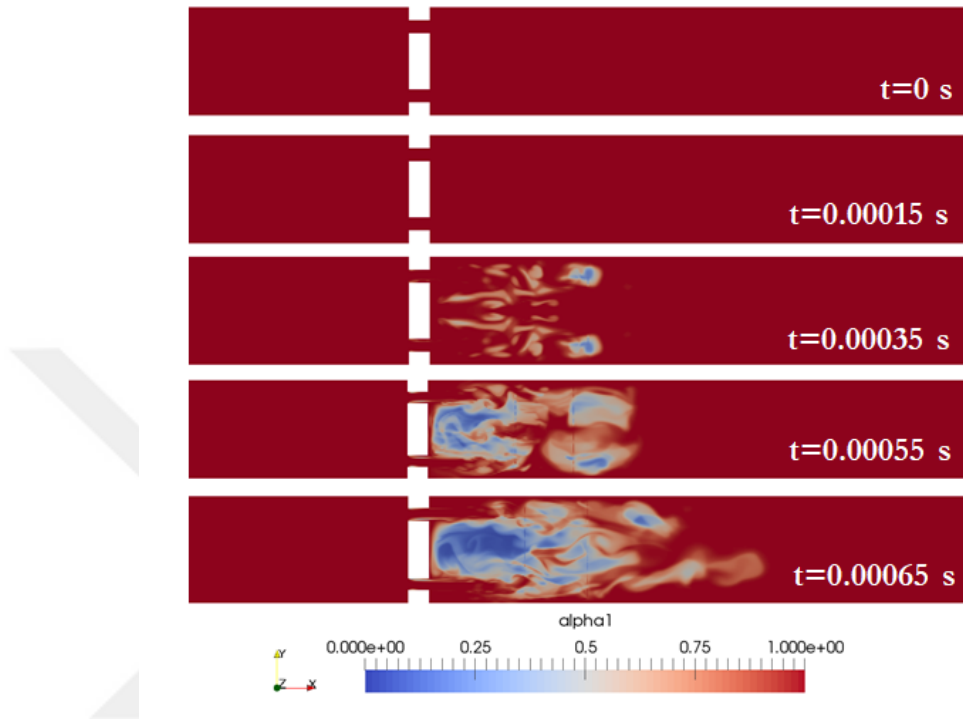


Figure 4.18: Alpha Contour with Respect to Time For Double Channel Geometry

4.3 Triple Channel Geometry

Triple channel geometry is created by placing three equal sized channels with equal distances to each other. Similar to the double channel geometry jets created for each channel is identical with the single channel geometry until they collide with each other. After the interaction flow becomes completely chaotic. In this manner, velocity contour changing with respect to time is given in Figure 4.19 for the simulations with inlet pressure of 3 Bar. Pressure and alpha contours are given in Section B.0.4.1.

As it is seen, flow is symmetrical until jets interact with each other at a previous time step than the double channel geometry. This behaviour is expected since the distance between the channels are narrower than the double channel geometry. Then when jets interact with each other flow pattern becomes random and chaotic again.

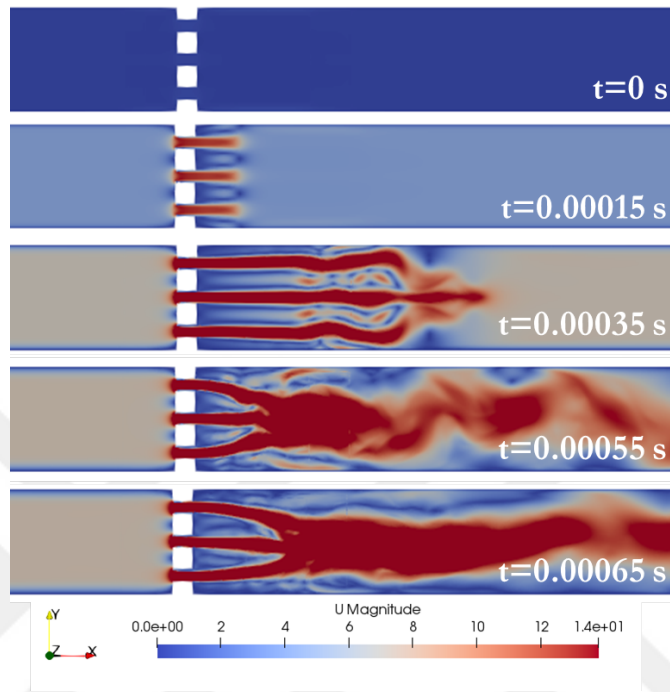


Figure 4.19: Velocity Contour with Respect to Time for Triple Channel Geometry

Pressure drop along the centerline of each channel is investigated for the 0.0005 second again.

Bubbles on the other hand starts to occur before that time since the pressure drop reaches below the vapour pressure beforehand. Related alpha contour is given in Figure 4.21.

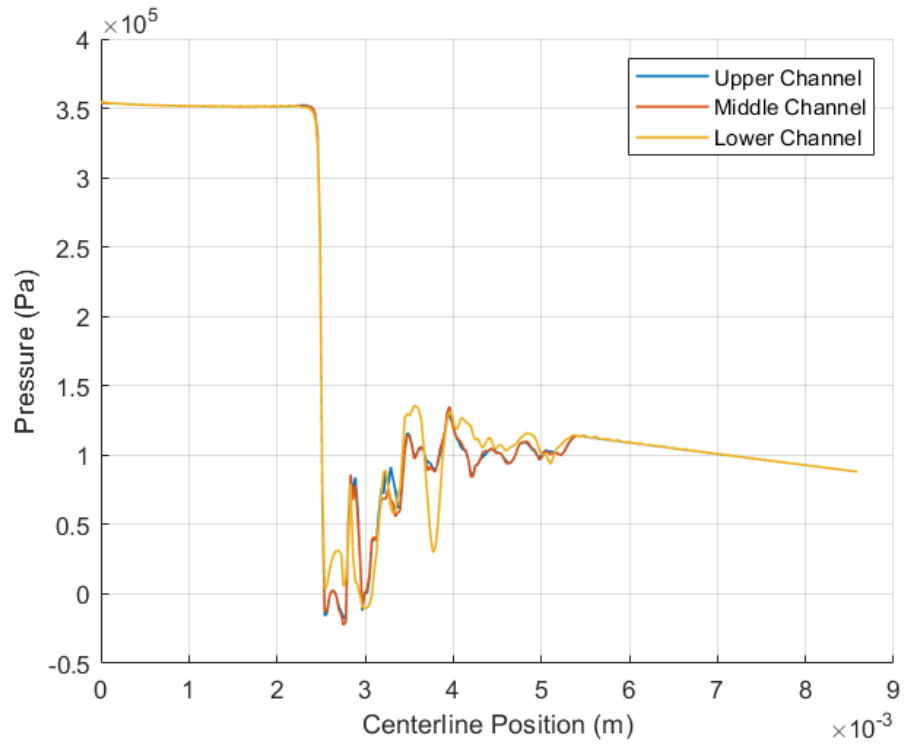


Figure 4.20: Pressure Change in Channels in Triple Channel Geometry

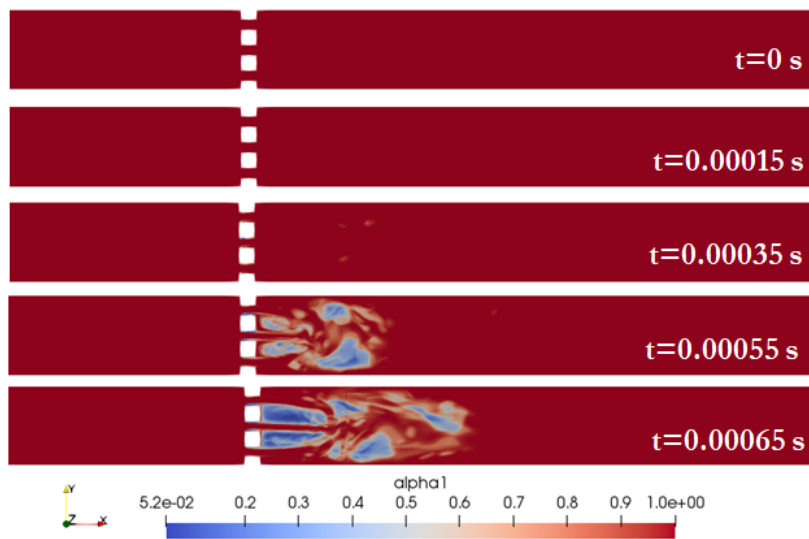


Figure 4.21: Alpha Contour with Respect to Time for Triple channel geometry

4.4 Nozzle Inspired Channel Geometry

4.4.1 Smaller to Larger Cross Section

Nozzle inspired geometries are created with increasing or decreasing the initial inflow area at the throttle region. As it is expected, when the exit area is smaller than the inlet area flow tends to speed up and opposite happens when the exit area is larger. In this manner, velocity contour changing with respect to time is given in Figure 4.22 for the simulations with inlet pressure of 3 Bar. Pressure and alpha contours are given in Section B.0.4.1.

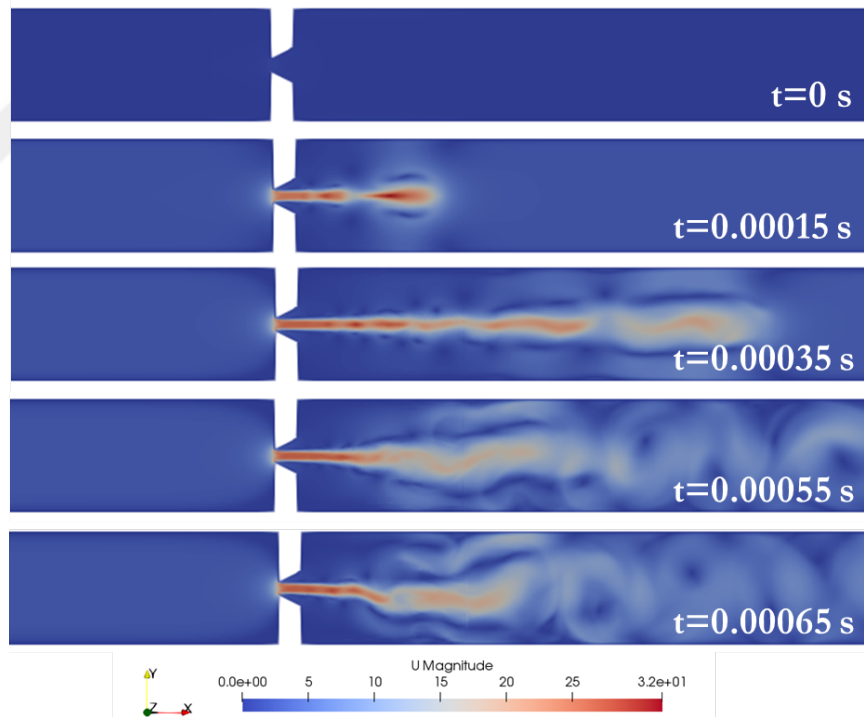


Figure 4.22: Velocity contour with respect to time for nozzle type channel geometry

In this manner, velocity contour of the mirrored geometry is given in 4.23. Different characteristics of the jets can be seen at $t=0.00035$ clearly. Jet in Figure 4.23 goes further than the one given in 4.22.

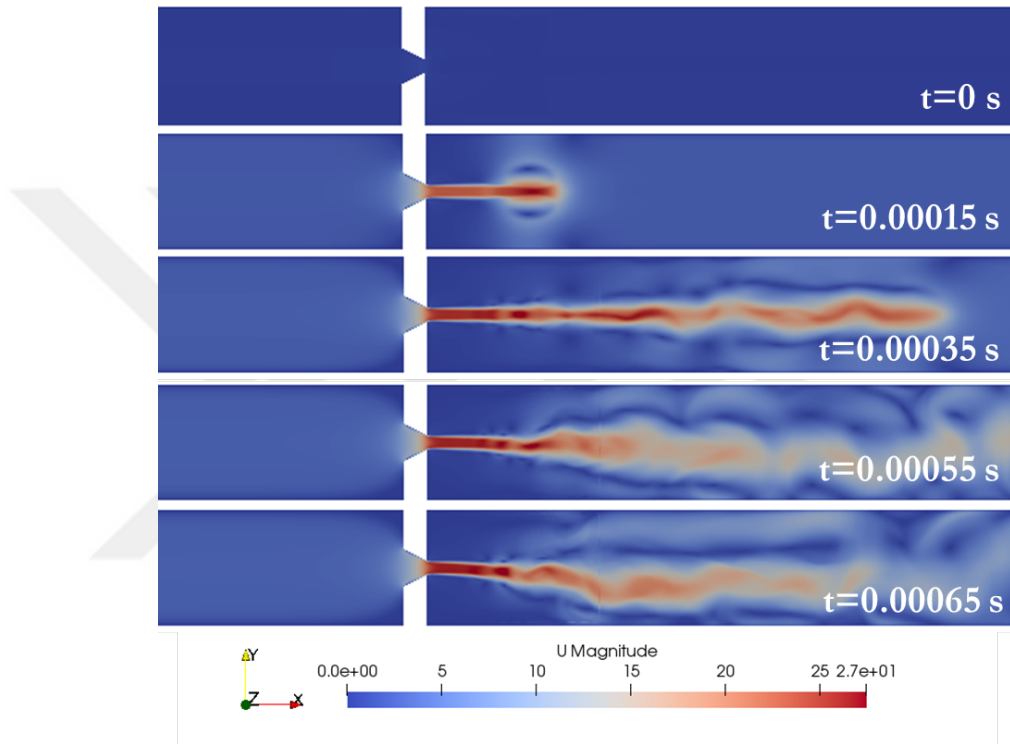


Figure 4.23: Velocity contour with respect to time for nozzle type channel geometry

To compare the phase change behaviour pressure changes along the centerline of both channels are presented in 4.24. It is seen that in larger to smaller section geometry, pressure drop is higher as it is expected.

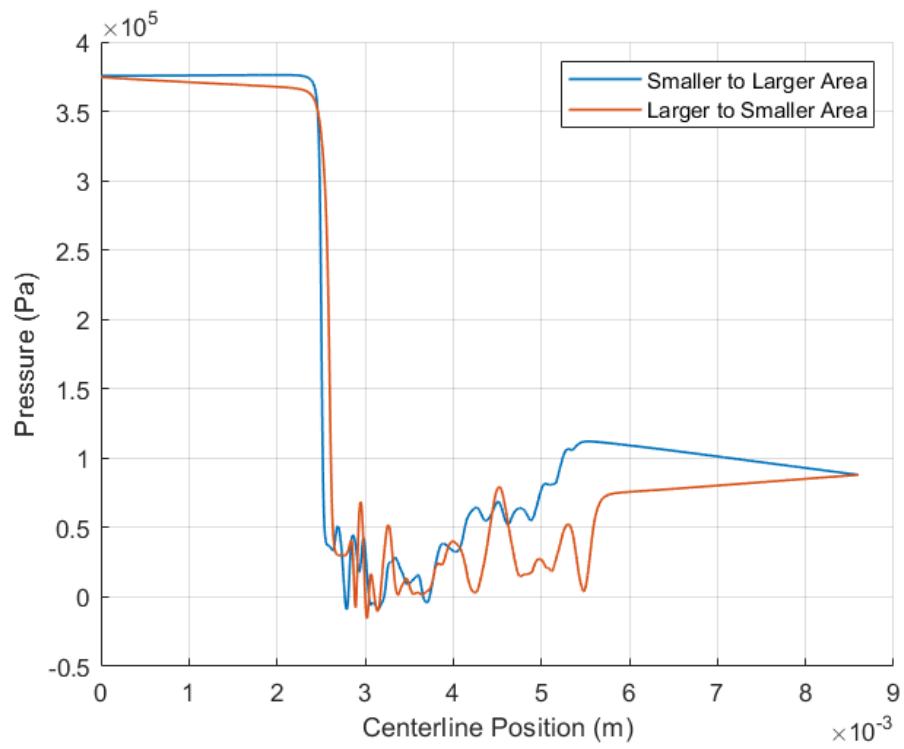


Figure 4.24: Pressure changes along the centerline of the nozzle inspired geometries

4.5 Double Inclined Geometry

Double inclined geometry is formed by two channels placed inclined to each other with 80.06 degrees as shown in Figure 4.25.

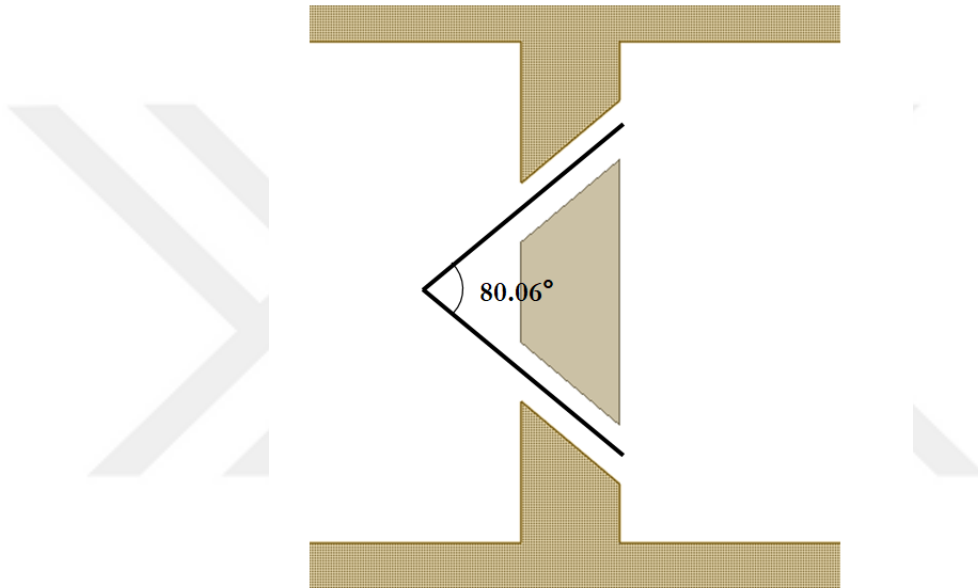


Figure 4.25: Angles in between channels

Firstly the jets are investigated regarding the velocity contours for 3 Bar inlet pressure given in Figure 4.26. It is seen that again two symmetrical jets are flowing until they distort each other.

Alpha contour of the given time steps are given in Figure 4.27 below. Fastest phase change is observed for this design due to the flow direction.

Corresponding pressure contour and vectors along the streamline are given in Section B.0.4.4.

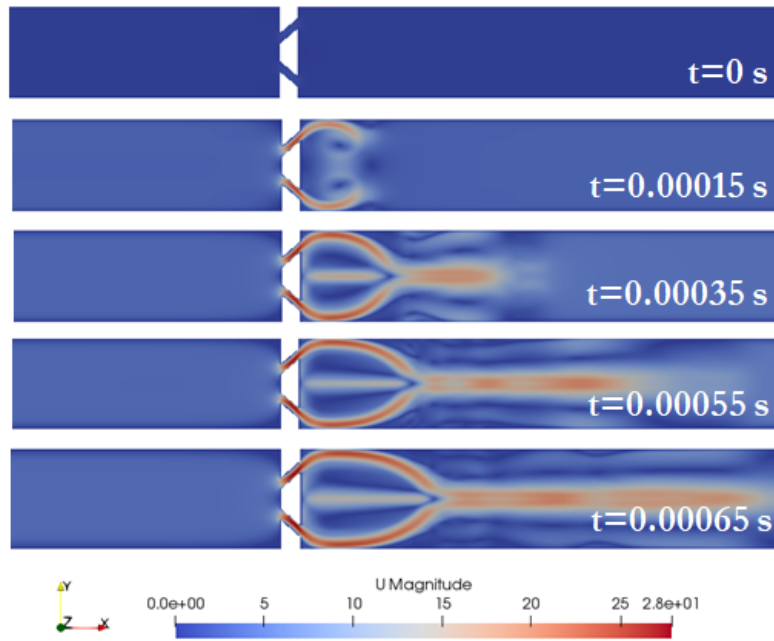


Figure 4.26: Velocity contour with respect to time for nozzle type channel geometry

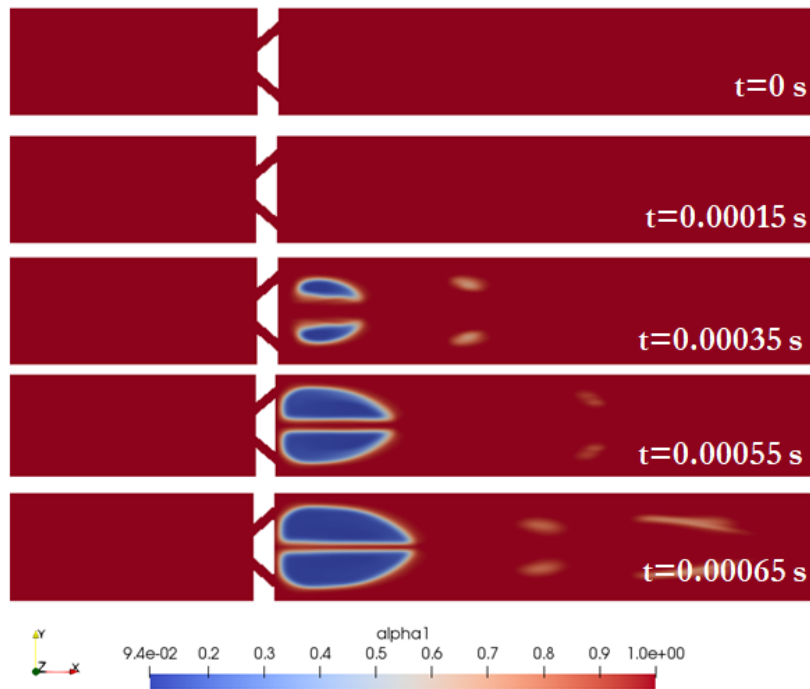


Figure 4.27: Alpha contour with respect to time for nozzle type channel geometry

Chapter 5

Experimental Set-up, Fabrication and Results

Experimental set-up was built to observe the cavitation phenomena. This set-up includes several parts such as the microfluidic devices whose geometries were given in Chapter 3, the pressure pump that is the main drive for fluid flow and a high speed camera for capturing the motion. In this chapter, components of the experiment set up and fabrication method will be explained. Lastly, the visuals obtained from the set-up is presented.

5.1 Set-Up

The set up includes several components which are listed below;

- A pressure pump
- Pressure regulator
- Air drier
- Flow rate sensor

- Microfluidic chip
- Fluidic connectors
- High speed microscope
- Pressure supply

The listed items are connected with each other as it is given in Figure 5.1 below.

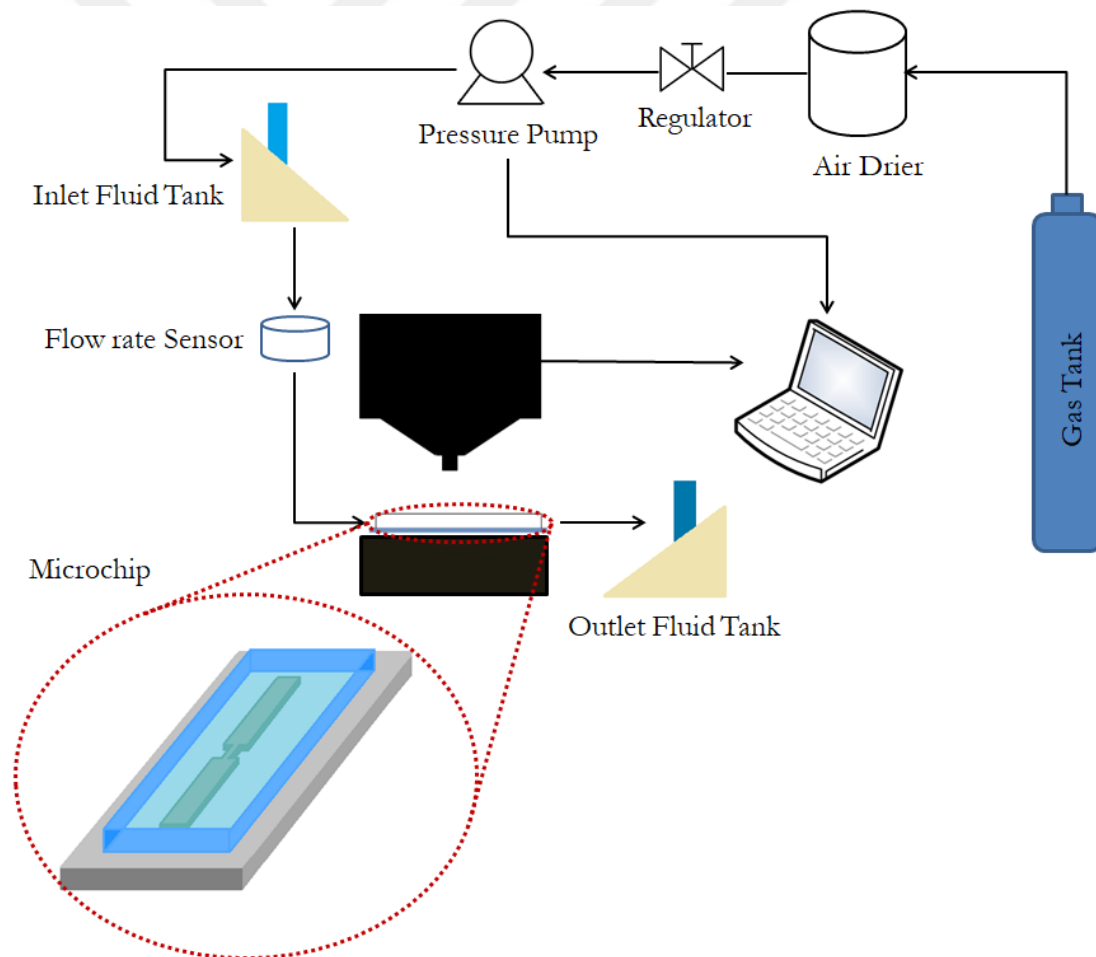


Figure 5.1: Experimental Set up

5.2 Fabrication of Microfluidic Chips

Microfluidic chips in which the cavitation was investigated were fabricated with photolithography technique. Among the different types of polymers, polydimethylsiloxane (PDMS) was used to create the chips with the conventional softlithography.

The procedure starts with creating a SU-8 (negative photoresist) mold that consists the desired chip geometries. Then using the mold the chips were fabricated from the PDMS and bonded to glass. The detailed procedure is as follows;

1) First step for the process is cleaning a 4 inch silicon wafer with acetone, isopropanol and DI water respectively. Then it is dried completely with first nitrogen gun and afterwards by putting it into the oven at 120°C for 5 minutes to vaporize the moisture remaining on the surface.

2) As an initial base layer, wafer is coated with SU-8 2005 by using spin coater. Spin parameters are given in Table 5.1. Chemical information and parameters of SU-8 2005 is set regarding the data sheet provided [47].

Table 5.1: Spin parameters for base layer

Step	Velocity (rpm)	Acceleration (rpm/s)	Time (s)
1	500	100	25
2	200	200	40

3) The wafer is prebaked on a hot plate with 65°C, 95°C and 65°C step by step with 2, 4 and 1 minutes respectively. When the heating is over wafer is cooled down to room temperature.

4) Later, the wafer is exposed to UV light with the settings provided below by using an empty glass mask.

- Manual top side - Contact Mode: Soft Contact
- Separation: 100 μm
- Mask thickness: 2.3 mm
- Sample thickness: 0.5 mm

- Resist thickness: $2 \mu m$
- Exposure intensity: $120 mJ/cm^2$

5) Sample is baked again at $65^\circ C$, $95^\circ C$ and $65^\circ C$ on hot plate for 1, 3, and 1 minutes respectively and left for cooling down to room temperature.

6) Next step is coating the wafer with SU-8 2050 with spin coater. The parameters used for this step is provided in Table 5.2 below [48].

Table 5.2: Spin parameters for main layer

Step	Velocity (rpm)	Acceleration (rpm/s)	Time (s)
1	500	50	40
2	2200	300	35

7) Wafer is baked again at $65^\circ C$, $95^\circ C$, and $65^\circ C$ on heaters for 3, 8, and 2 minutes respectively and then left for cooling to the room temperature.

8) Later, the wafer is exposed to UV light with the settings provided below and using the mask created before the process. Design of the mask consists of the desired chip geometries and it is given in C.

- Manual top side
- Contact Mode: Soft Contact
- Separation: $200 \mu m$
- Mask thickness: 2.3 mm
- Sample thickness: 0.5 mm
- Resist thickness: $2 \mu m$
- Exposure intensity: $230 mJ/cm^2$

9) Following the spin coating process, wafer is baked at $65^\circ C$, $95^\circ C$ and $65^\circ C$ on heaters for 3, 8, and 2 minutes respectively and then left for cooling down to the room temperature.

10) After the wafer is cooled down to the room temperature it is put in to SU=8 developer solution.

- 11) When the geometries are formed the wafer is washed with DI water.
- 12) Wafer is dried with a nitrogen gun until there are no water bubbles left and then the PDMS mixture with its curing agent is poured on the wafer.
- 13) To eliminate the bubbles inside the PDMS mixture, the vacuum pump is used.
- 14) When there are no bubbles inside the solution, it is put on the oven at 80°C for 30 minutes to harden PDMS.
- 15) As the PDMS hardens, it is peeled off from the master mold and cut into the pieces forming the chips and tubing holes are also opened.
- 16) Following the cleaning procedure of both PDMS mold and the glass, they are bonded to each other with plasma cleaner.
- 17) As a final step, tubings are connected to the chips with epoxy.

Steps that are taken during this process is schematically shown in 5.2.

Chips that are fabricated with this method are investigated under the microscope. Figure 5.3 shows the sample produced.

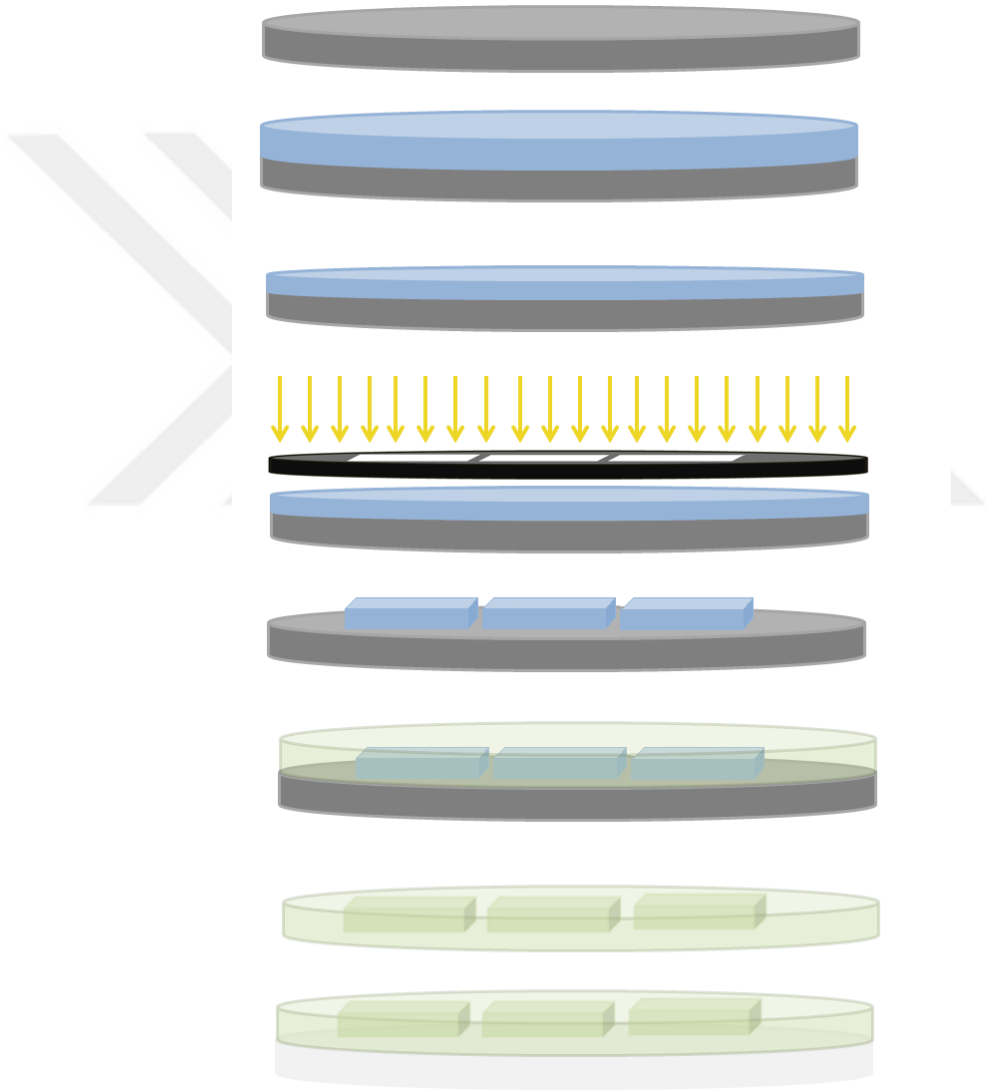


Figure 5.2: Photolithography technique to produce microchips with negative photoresist

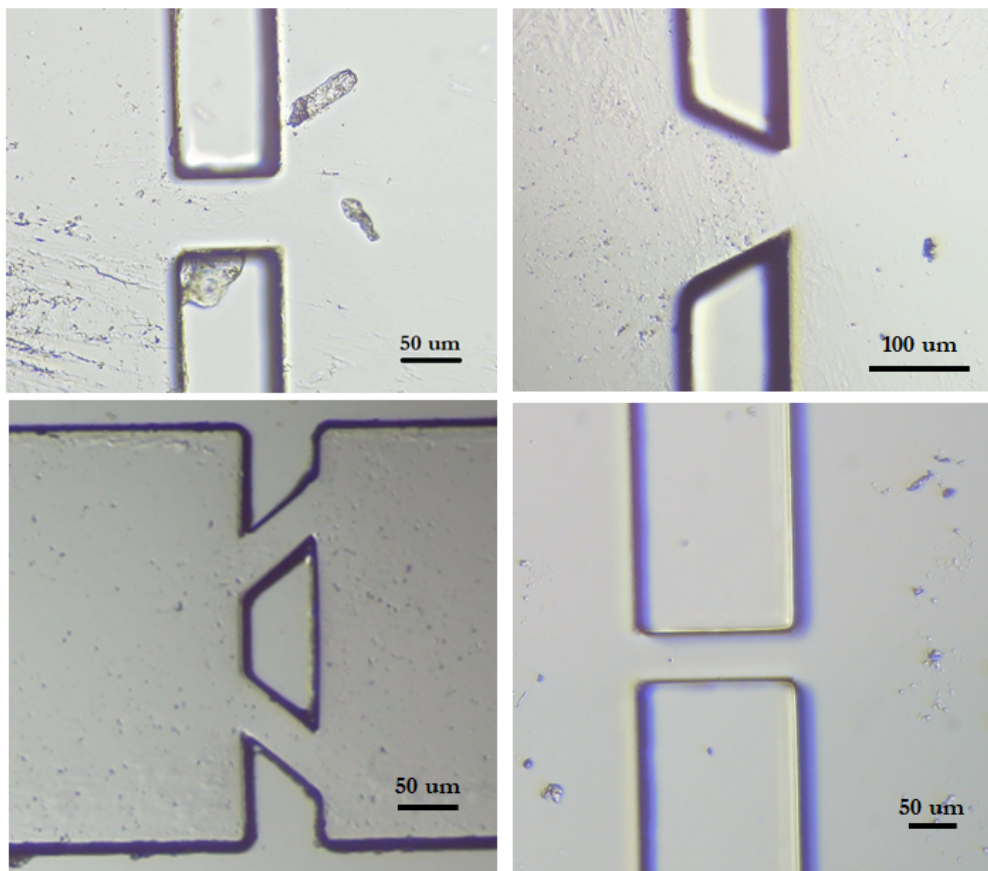


Figure 5.3: Visuals of the produced chips

5.3 Experimental Results

From the set-up that is previously explained, by using high speed camera taking 8-16 frames per second visuals of the cavitating flows are taken. It is seen that for lower input pressure values, flow does not encounter any phase changes. Representation of these flows are given in Figure 5.4 below for single throttle channel in 3 bars. It is shown that these flows are creating regular steady state flow behavior.

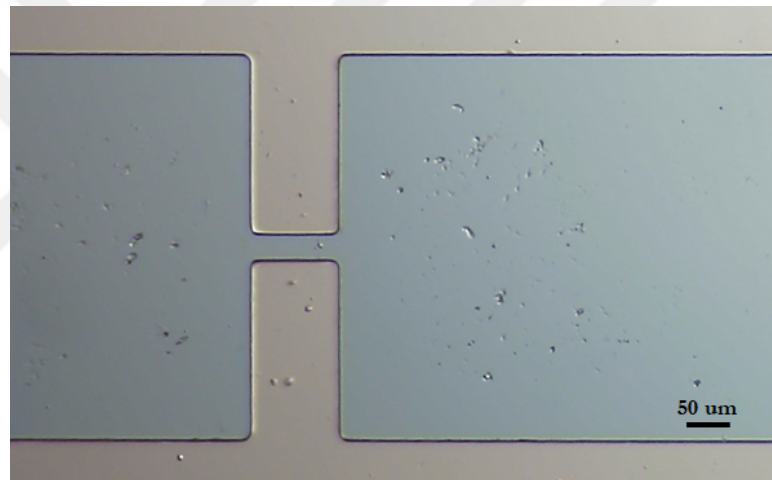


Figure 5.4: Steady flow in 30 micron width channel with 3 bars input pressure

This behaviour does not change its characteristics with any of the designs pre-described. For example Figure 5.5 shows the same steady flow with nozzle inspired geometry.

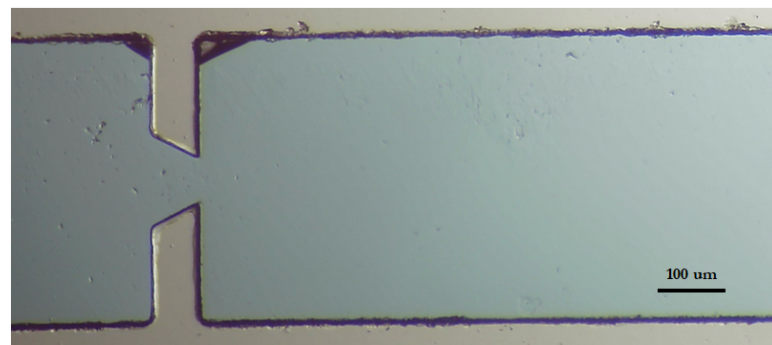


Figure 5.5: Steady flow in nozzle inspired geometry with 3 bars input pressure

As the input pressure is increased however, flow characteristics change like it is predicted in the simulations. For example for higher pressure values bubbles tend to occur and fade away. Around 4 and 5 bars these random bubbles start to occur as it is also predicted in the simulations early time steps. For 30 micron width single throttle channel the moment of the bubble occurring is captured and marked in 5.6. More visuals are provided in D.

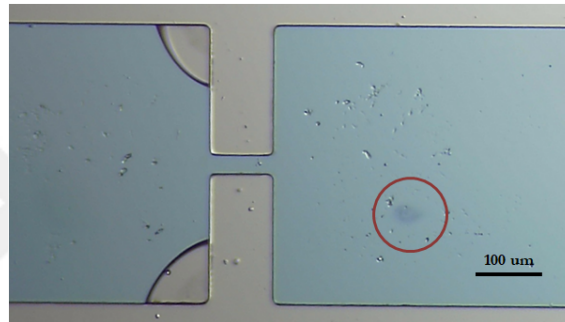


Figure 5.6: Vapour Bubble in the 30 Micron Channel

For around 5 and 6 bars, bubbles given in Figure 5.6 becomes multiple and resembles the simulation more. This similarity is highlighted in Figure 5.7 as both the CFD and the experiments have multiple initial low density zones.

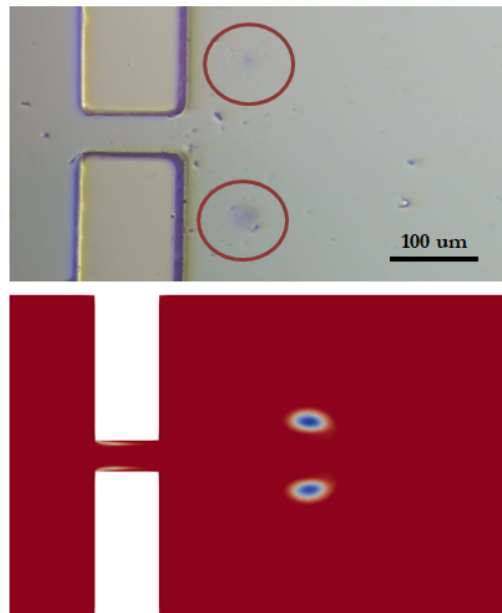


Figure 5.7: Simulation vs. Experimental Low Density Zones

For the higher velocities these formation of bubbles increase however since the flow is highly chaotic bubbles occur and disappears suddenly. Visual of this kind of a moment is given in Figure 5.8 with the similar simulation result.

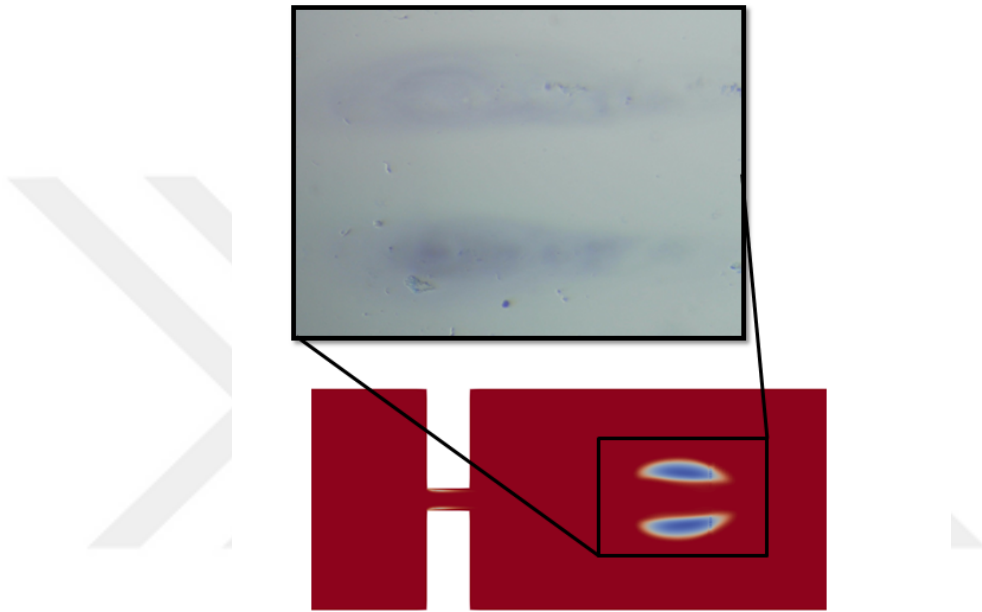
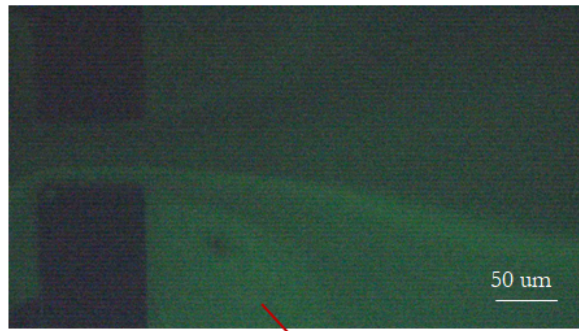


Figure 5.8: Symmetrical Low Density Zones in Simulation and Experiments

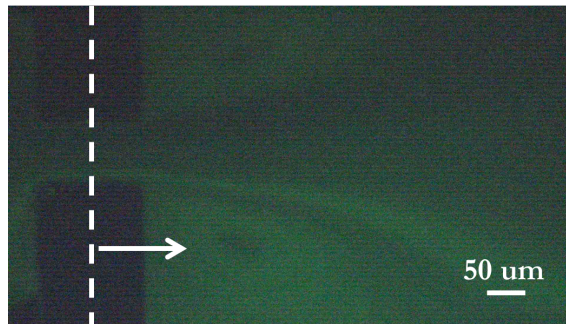
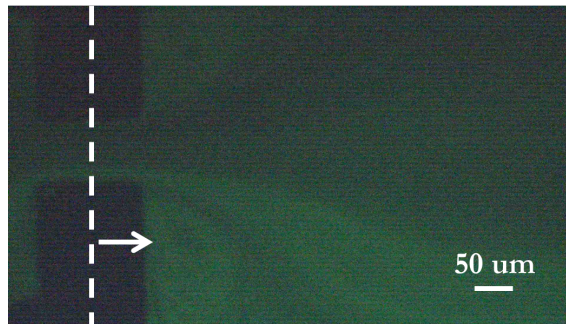
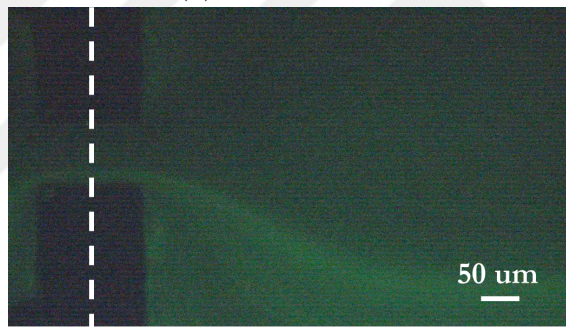
Cavitation behaviour is also investigated using latex beads, which are carboxylate-modified polystyrene fluorescent yellow-green, to compare the experimental results with simulation.

In Figure 5.9a, the region of vortex is clearly seen at the initial time steps and the movement of the vortex region is shown in Figure 5.9b.



Vortex region

(a) Vortex Region



(b) Movement of the vortex region with respect to the initial position

Figure 5.9: Vortex region (a) and its movement (b)

Then as the time passes, the cavitation zone becomes larger which is shown in Figure 5.10.

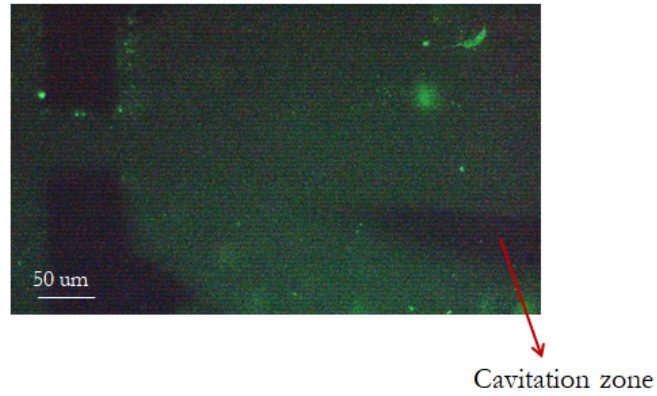


Figure 5.10: Cavitation Zone

Symmetrical formation of low density zones where the simulation also predicts is given in Figure 5.11.

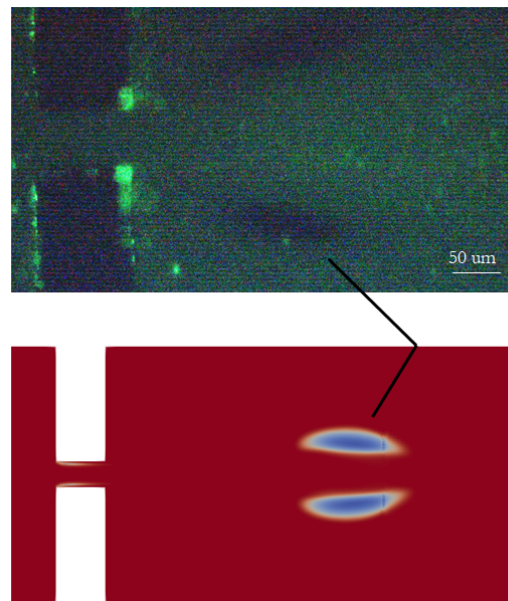


Figure 5.11: Symmetrical Low Density Zones

Throughout these experiments several parameters are controlled for the accuracy of the processes. Firstly, qualities of the chips which are fabricated by using PDMS and glass are kept constant by mixing the same amount of PDMS and

curing agent for every trial. Also, as the length of the tubing is important to reduce the friction and import a higher velocity fluid, the length of the tubings are also measured equally and implemented in the same ways for each chip. In addition, fluid is always used from the sealed tube providing the same fluid constantly to the system. Identical situation applies for the pressurized gas that is used for the pressure pump, also the pressure regulator is kept constant at its possible maximum condition always to prevent any input pressure changes.

Also, de-gasification was tried by placing the water in a vacuum chamber for 24 hours. Similar pattern is observed on our case due to our set-up as it is seen in Figure 5.12 below.

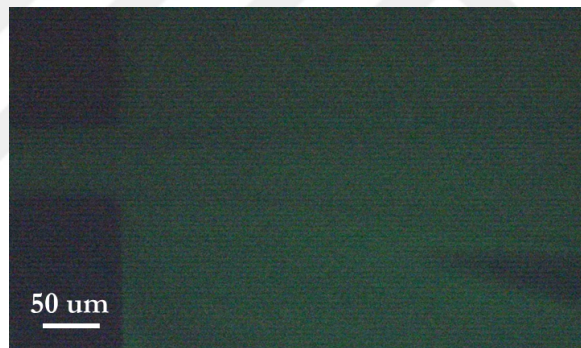


Figure 5.12: Cavitation Bubble with Degasified Water

However, even the experimental results show great resemblance with the simulations, certain upgrades can be applied for better quality. These improvements that will increase the visual capability and data quality will be discussed in 6.

Chapter 6

Conclusion and Future Work

Throughout this study, several geometries and test cases were produced to investigate the behavior of cavitating flows. To simulate the flow, measurements are conducted and implemented in the open source software OpenFoam with the boundary conditions that are verified previously.

Several different cases were run for single throttle channel geometry such that both the effect of thickness of the channel and the effect of input pressure on the cavitation is investigated. Cases with varying input pressures were also generated for other geometries.

It is seen that increasing the Reynolds Number and decreasing the channel width shifted *vena contracta* point towards left. On the other hand, increasing the channel width moved it towards right. It is also observed that the channel length does not have any significant effect on the *vena contracta* point. As the *vena contracta* point shifts towards right it can be said that the bubbles are forming at a previous time step.

However, decreasing the channel width too much also results of higher friction and dominance of viscous forces. Therefore, it is not always correct to say that as the channel width decreases bubbles form faster.

Simulations were conducted 2D since difference between 2D and 3D were considered small and 3D analysis were expensive to conduct. However, for a better accuracy, simulations could be ran 3D. On the other hand, tubings are connected to the chips vertically in real life. Yet, simulations did not consider the friction from the flow changing its direction.

Along with the simulations, experiments were also conducted with a set up that basically consists of a pressure pump, fabricated chips and a high speed microscope. In this manner, visuals of the bubbles are captured for several different cases. While conducting the experiments, major problem is the descending velocity through the channels. It is seen that most of the velocity generated by the pressure difference is lost due to the friction and viscous forces generated by the tubing before entering the chips which caused phase change to occur only in the highest pressure input by lowering the tubing length. This problem occurred due to the pressure pump used for the experiments and its low compatibility with tubing with larger diameters. To be able to generate higher velocities inside the chips larger tubing could be used by modifying the gadget. If not possible, pressure source can be changed.

To avoid pressure loss, it is also possible to use a pressure pump and a chip design that pressure is implemented from the middle of the channel as Mishra et. al. suggest [49]. On the other hand, to be able to generate experimental data for calculating flow coefficients or validating the solver with experimental data, local pressure, velocity and temperature sensor should be used [50].

Some parameters throughout the experimental procedure were easy to keep constant or equal, however there were some which could not be kept in its ideal form. One example of this situation is come across with the fluorescent particles uniformity. As the particles stay longer in the water solution, solution's homogeneity is lost causing some regions to shine more brightly than other regions. As a suggested future work, surface properties can be investigated as a parametric study to see its effect on cavitation behaviour. More properties of the same kind could be generated for parametric studies with a suitable set-up.

Also, de-gasification was tried by a vacuum chamber by placing the liquid beforehand yet process is not serving for the purpose of the study since most of the coolants used in industry cannot be de-gasified before entering the cooling channels. However as a suggested future work, de-gasification can be performed parametrically to study on its effect on cavitation.

Even with these conditions, simulations show great accuracy with both literature and experimental visuals. With the suggested additions, validations can be improved with more data and more accurate CFD results.

As a future work, simulations with even higher inlet pressures as well as variations in the thickness of the channel widths of the new designs could be tried such that a pattern between generated bubbles and channel thickness could be observed to serve for controllable bubble generation chips. Also, the relation between the inlet pressure and the starting time step of chaotic behaviour of the flows can be studied as a future work.

Bibliography

- [1] M. F. Wadel, “Comparison of high aspect ratio cooling channel designs for a rocket combustion chamber with development of an optimized design,” 1998.
- [2] J. Huh and S. Kwon, “Microcooling channel effect on a monopropellant microelectromechanical system thruster performance,” *Journal of Propulsion and Power*, vol. 33, no. 6, pp. 1591–1595, 2017.
- [3] H. Ziebland and R. Parkinson, “Heat transfer in rocket engines.,” 1971.
- [4] C. E. Brennen, *Cavitation and bubble dynamics*. Cambridge University Press, 2014.
- [5] N. Tamaki, M. Shimizu, K. Nishida, and H. Hiroyasu, “Effects of cavitation and internal flow on atomization of a liquid jet,” *Atomization and Sprays*, vol. 8, no. 2, 1998.
- [6] R. E. Arndt, “Cavitation in fluid machinery and hydraulic structures,” *Annual Review of Fluid Mechanics*, vol. 13, no. 1, pp. 273–326, 1981.
- [7] T. Aoyama, S. Suzuki, A. Kawamoto, T. Noda, T. Ozasa, T. Kato, and T. Ito, “Preventive design and analysis of cavitation noise on diesel engine,” *R&D Review of Toyota CRDL*, vol. 40, no. 1, 2007.
- [8] M. Pizzarelli, F. Nasuti, and M. Onofri, “Analysis of curved-cooling-channel flow and heat transfer in rocket engines,” *Journal of Propulsion and Power*, vol. 27, no. 5, pp. 1045–1053, 2011.

- [9] H. Shi, M. Li, P. Nikrityuk, and Q. Liu, “Experimental and numerical study of cavitation flows in venturi tubes: From cfd to an empirical model,” *Chemical Engineering Science*, vol. 207, pp. 672–687, 2019.
- [10] L. Hanimann, L. Mangani, E. Casartelli, and M. Widmer, “Steady-state cavitation modeling in an open source framework: Theory and applied cases,” 2016.
- [11] R. E. Bensow and G. Bark, “Simulating cavitating flows with les in open-foam,” in *V European conference on computational fluid dynamics*, pp. 14–17, 2010.
- [12] C. P. Egerer, S. Hickel, S. J. Schmidt, and N. A. Adams, “Large-eddy simulation of turbulent cavitating flow in a micro channel,” *Physics of Fluids*, vol. 26, no. 8, p. 085102, 2014.
- [13] G. Cazzoli, S. Falfari, G. M. Bianchi, C. Forte, and C. Catellani, “Assessment of the cavitation models implemented in openfoam® under di-like conditions,” *Energy Procedia*, vol. 101, pp. 638–645, 2016.
- [14] A. Asnaghi, A. Feymark, and R. E. Bensow, “Numerical simulation of cavitating flows using openfoam,” in *Proceedings of the 18th Numerical Towing Tank Symposium, Cortona, Italy*, 2015.
- [15] H. G. Weller, G. Tabor, H. Jasak, and C. Fureby, “A tensorial approach to computational continuum mechanics using object-oriented techniques,” *Computers in Physics*, vol. 12, no. 6, p. 620, 1998.
- [16] C. Mishra and Y. Peles, “An experimental investigation of hydrodynamic cavitation in micro-venturis,” *Physics of Fluids*, vol. 18, no. 10, p. 103603, 2006.
- [17] P. Rudolf, D. Kubina, M. Hudec, J. Kozák, B. Maršálek, E. Maršálková, and F. Pochylý, “Experimental investigation of hydrodynamic cavitation through orifices of different geometries,” in *EPJ Web of Conferences*, vol. 143, p. 02098, EDP Sciences, 2017.

- [18] B. Schneider, A. Koşar, and Y. Peles, “Hydrodynamic cavitation and boiling in refrigerant (r-123) flow inside microchannels,” *International Journal of Heat and Mass Transfer*, vol. 50, no. 13-14, pp. 2838–2854, 2007.
- [19] C. Mishra and Y. Peles, “Size scale effects on cavitating flows through microorifices entrenched in rectangular microchannels,” *Journal of microelectromechanical systems*, vol. 14, no. 5, pp. 987–999, 2005.
- [20] C. Mishra and Y. Peles, “Development of cavitation in refrigerant (r-123) flow inside rudimentary microfluidic systems,” *Journal of microelectromechanical systems*, vol. 15, no. 5, pp. 1319–1329, 2006.
- [21] Z.-j. Jin, Z.-x. Gao, X.-j. Li, and J.-y. Qian, “Cavitating flow through a micro-orifice,” *Micromachines*, vol. 10, no. 3, p. 191, 2019.
- [22] R. Singh and Y. Peles, “The effects of fluid properties on cavitation in a micro domain,” *Journal of Micromechanics and Microengineering*, vol. 19, no. 2, p. 025009, 2009.
- [23] S. Dabiri, W. Sirignano, and D. Joseph, “Cavitation in an orifice flow,” *Physics of Fluids*, vol. 19, no. 7, p. 072112, 2007.
- [24] M. Ghorbani, G. Deprem, E. Ozdemir, A. R. Motezakker, L. G. Villanueva, and A. Koşar, “On “cavitation on chip” in microfluidic devices with surface and sidewall roughness elements,” *Journal of Microelectromechanical Systems*, vol. 28, no. 5, pp. 890–899, 2019.
- [25] V. Lomakin, M. Kuleshova, and E. Kraeva, “Fluid flow in the throttle channel in the presence of cavitation,” *Procedia Engineering*, vol. 106, pp. 27–35, 2015.
- [26] M. Medrano, P. Zermatten, C. Pellone, J.-P. Franc, and F. Ayela, “Hydrodynamic cavitation in microsystems. i. experiments with deionized water and nanofluids,” *Physics of Fluids*, vol. 23, no. 12, p. 127103, 2011.
- [27] C. Mishra and Y. Peles, “Flow visualization of cavitating flows through a rectangular slot micro-orifice ingrained in a microchannel,” *Physics of Fluids*, vol. 17, no. 11, p. 113602, 2005.

- [28] M. Medrano, C. Pellone, P. Zermatten, and F. Ayela, “Hydrodynamic cavitation in microsystems. ii. simulations and optical observations,” *Physics of Fluids*, vol. 24, no. 4, p. 047101, 2012.
- [29] *OpenFOAM User Guide*.
- [30] *FRP: flow-rate platform, a microfluidic flow sensor*.
- [31] A. Sadaghiani, H. Rajabnia, S. Çelik, H. Noh, H. Kwak, M. Nejatpour, H. Park, H. Acar, B. Mısırlıoğlu, M. Özdemir, *et al.*, “Pool boiling heat transfer of ferrofluids on structured hydrophilic and hydrophobic surfaces: The effect of magnetic field,” *International Journal of Thermal Sciences*, vol. 155, p. 106420, 2020.
- [32] A. K. Sadaghiani, R. Altay, H. Noh, H. Kwak, K. Şendur, B. Mısırlıoğlu, H. Park, and A. Koşar, “Effects of bubble coalescence on pool boiling heat transfer and critical heat flux—a parametric study based on artificial cavity geometry and surface wettability,” *International Journal of Heat and Mass Transfer*, vol. 147, p. 118952, 2020.
- [33] C. Greenshields, “Openfoam v6 user guide: 4.5 solution and algorithm control,” July 2018.
- [34] T. Holzmann, *Mathematics, Numerics, Derivations and OpenFOAM(R)*. 3 2019.
- [35] D. M. Mughal, *Wind Prediction Modelling and Validation using Coherent Doppler LIDAR Data*. PhD thesis, Curtin University, 12 2016.
- [36] M. Deshpande, J. Feng, and C. L. Merkle, “Numerical modeling of the thermodynamic effects of cavitation,” 1997.
- [37] G. H. Schnerr and J. Sauer, “Physical and numerical modeling of unsteady cavitation dynamics,” in *Fourth international conference on multiphase flow*, vol. 1, ICMF New Orleans, 2001.
- [38] G. Schnerr, “Modeling and computation of unsteady cavitating flows based on bubble dynamics,” in *Numerical simulations of incompressible flows*, pp. 544–574, World Scientific, 2003.

- [39] J. V. Lienhard and J. I. Lienhard, “Velocity coefficients for free jets from sharp-edged orifices,” 1984.
- [40] S. A. Hall, M. E. Bricker, D. L. Willet, W. N. Irani, I. Afridi, and P. A. Grayburn, “Assessment of mitral regurgitation severity by doppler color flow mapping of the vena contracta,” *Circulation*, vol. 95, pp. 636–642, Apr 1997.
- [41] N. D. Katopodes, *Free-surface flow: environmental fluid mechanics*. Butterworth-Heinemann, an imprint of Elsevier, 2019.
- [42] D. J. B. Calvert, “Coefficient of discharge.”
- [43] “Orifice, nozzle and venturi flow rate meters.”
- [44] F. Johansen, “Flow through pipe orifices at low reynolds numbers,” *Proceedings of the royal society of London. series A, containing Papers of a Mathematical and Physical character*, vol. 126, no. 801, pp. 231–245, 1930.
- [45] H. E. Merritt, *Hydraulic control systems*. John Wiley & Sons, 1991.
- [46] D. Wu, R. Burton, and G. Schoenau, “An empirical discharge coefficient model for orifice flow,” *International journal of fluid power*, vol. 3, no. 3, pp. 13–19, 2002.
- [47] “Microchem, su-8 2000 permanent epoxy negative photoresist processing.”
- [48] M. Saqib, *Effect of Channel Geometry on Alternating Droplet Generation*. PhD thesis, Bilkent University, 5 2018.
- [49] C. Mishra and Y. Peles, “Cavitation in flow through a micro-orifice inside a silicon microchannel,” *Physics of Fluids*, vol. 17, 2002.
- [50] A. Morozov and U. Iben, “Experimental analysis and simulation of cavitating throttle flow,” *HEFAT 2008*, 2008.

Appendix A

Code

```
1 %=====
2 % Poiseuille Flow
3 % Author: Gokce Ozkazanc
4 % Date: 21 April 2019
5 %=====
6 clear
7 clc
8 close all
9 %% Initializations
10 w = 60e-6;           %channel width
11 L = 800e-6;         %channel length
12 T = 1;              %total simulation time
13 dt = 1e-6;          %time step
14 dp_dx = 2000/L;    %pressure difference
15 mu = 1e-3;          %dynamic viscosity
16 Ny = 200;           %grid in y
17 Nx = 200;           %grid in x
18 %
19 % Grid calculation
20 dy = w/(Ny-1);
21 dx = L/(Nx-1);
22 mesh_y = 0:dy:w;
23 mesh_x = 0:dx:L;
```

```

24 [X,Y] = meshgrid(mesh_x,mesh_y);
25
26 Nt = ceil(T/dt);    %timestep
27 u_old = zeros(Ny, 1);
28
29 %% Foam
30 foam_data = importdata('lineX1.U.xy',' ');
31 foam_y = foam_data(:,1);
32 foam_u = foam_data(:,2);
33 [foamX,foamY] = meshgrid(mesh_x,foam_y);
34
35 foam_data3 = importdata('3D_int_lineX1.U.xy',' ');
36 foam_y3 = foam_data3(:,1);
37 foam_u3 = foam_data3(:,2);
38 [foamX3,foamY3] = meshgrid(mesh_x,foam_y);
39
40 foam_data2 = importdata('int_lineX1.U.xy',' ');
41 foam_y2 = foam_data2(:,1);
42 foam_u2 = foam_data2(:,2);
43 [foamX2,foamY2] = meshgrid(mesh_x,foam_y2);
44
45
46 %% Solution
47 for n = 1:Nt
48     % Thomas algorithm
49     N = size(u_old, 1);    u = zeros(N, 1);
50     C_1 = -dt/(2*dy^2);    C_2 = 1 + dt/(dy^2);
51     a = zeros(N-1, 1);    b = zeros(N, 1);    r = ...
        zeros(N, 1);
52     r(2) = dt*dp_dx/mu + (-C_2+2)*u_old(2) - C_1*u_old(3);
53     a(2) = C_1/C_2;    b(2) = r(2)/C_2;
54
55     for k = 3:N-2
56         r(k) = dt*dp_dx/mu + (-C_2+2)*u_old(k) - ...
            C_1*u_old(k+1) - C_1*u_old(k-1);
57         a(k) = C_1/(C_2-C_1*a(k-1)); b(k) = (r(k) - ...
            C_1*b(k-1))/(C_2 - C_1*a(k-1));
58     end
59     r(N-1) = dt*dp_dx/mu + (-C_2+2)*u_old(N-1) - C_1*u_old(N-2);
60     b(N-1) = (r(N-1) - C_1*b(N-2))/(C_2 - C_1*a(N-2));

```

```

61     u(N-1) = b(N-1);
62     for k = N-2:-1:2
63         u(k) = b(k) - a(k)*u(k+1);
64     end
65     % Dirichlet boundary conditions
66     u(1) = 0;          u(N) = 0;          u_old = u;
67 end
68 u_interp = imresize(u,1.3,'bilinear');
69 u_interp = u_interp(:,1);
70
71 grid_u = [];
72 grid_foam_u = [];
73 for k = 1:length(mesh_x)
74     grid_u = [grid_u u];
75     grid_foam_u = [grid_foam_u foam_u];
76 end
77
78 %% PLOTS
79 % Plot the analytical and Foam solutions
80 figure
81 plot(u, linspace(0, w, Ny))
82 hold on
83 plot(foam_u, foam_y, 'r')
84 hold on
85 plot(foam_u2, foam_y2, 'm')
86 grid on
87 title('Calculated Velocity for Different Solvers')
88 legend('Analytical Solution', 'simpleFoam', 'interPhaseChangeFoam')
89 ylabel('y (m)')
90 xlabel('Velocity (m/s)')
91 ylim([0 w])
92
93 %
94 % 2D vs. 3D
95 figure
96 plot(foam_u2, foam_y2, 'og')
97 hold on
98 plot(foam_u3, foam_y3, 'r')
99 hold on
100 grid on

```

```

101 %title('Difference of 2D and 3D solutions with respect to ...
        Analytical Solution')
102 legend('2D', '3D')
103 ylabel('y (m)')
104 xlabel('Velocity (m/s)')
105 ylim([0 w])
106
107 surf(mesh_x, mesh_y, grid_u)
108 ylabel('y (m)')
109 xlabel('x (m)')
110 title('Velocity From MATLAB')
111 view(2)
112 shading interp
113 colorbar
114 axis([0 L 0 w])
115
116 figure
117 surf(mesh_x, mesh_y, grid_u)
118 ylabel('y (m)')
119 xlabel('x (m)')
120 title('Velocity From MATLAB')
121 view(2)
122 shading interp
123 colorbar
124 axis([0 L 0 w])

```

Appendix B

Results

B.0.1 Discharge Coefficient Results

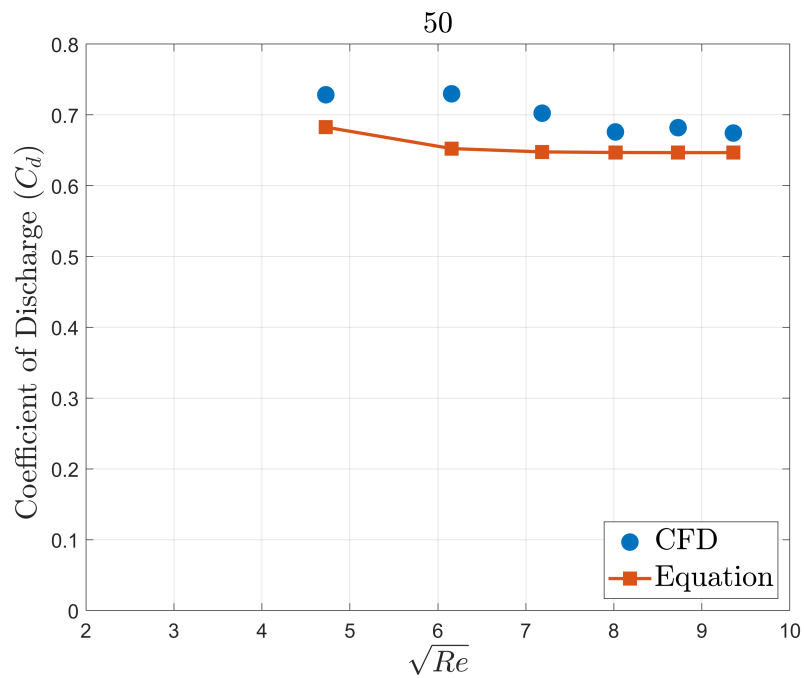


Figure B.1: $\beta=0,1$ and $A=0,5$

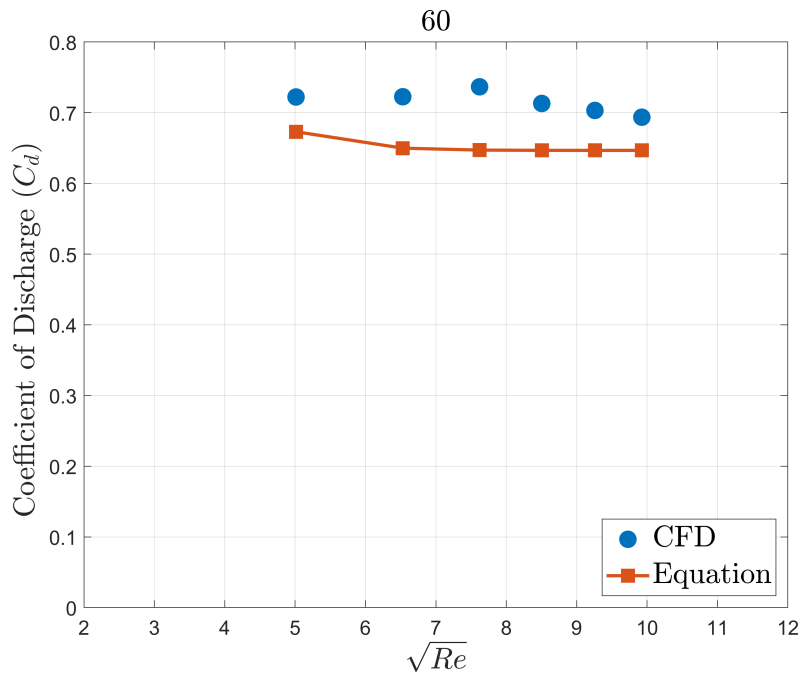


Figure B.2: $\beta=0,12$ ans $A=0,6$

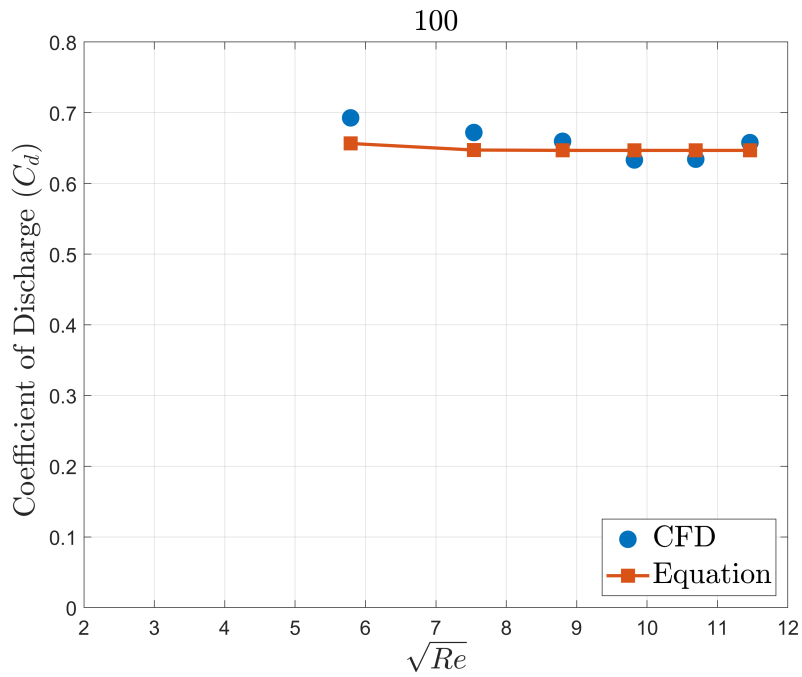


Figure B.3: $\beta=0,20$ and $A=1,0$

B.0.2 Effect of Input Pressure Results

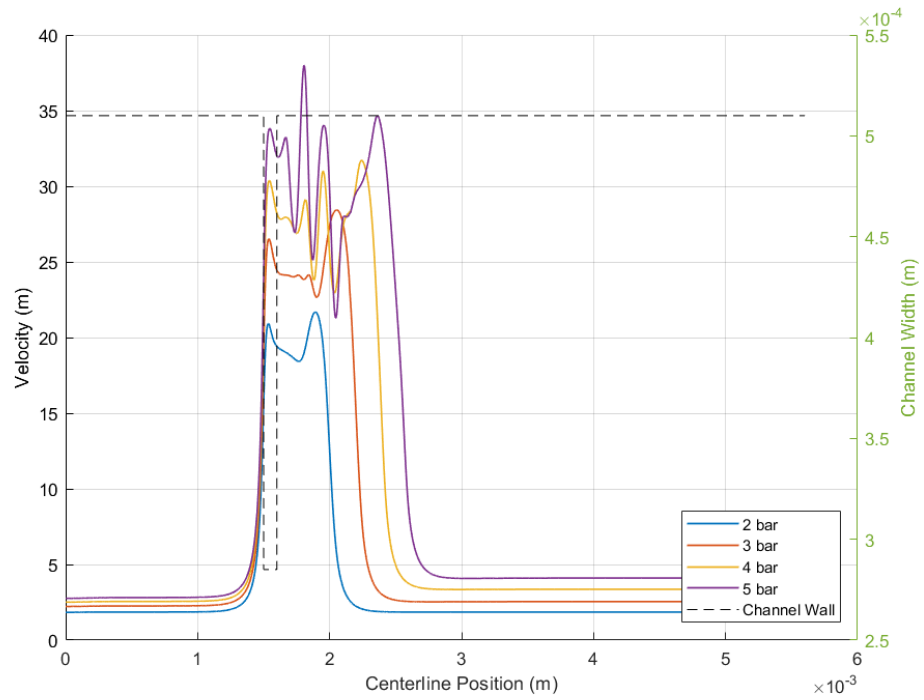


Figure B.4: Velocity Along the channel centerline in different pressure inputs

B.0.3 DhRe/L vs. Reynolds Number Table

Input Pressure (bar)	Channel Width											
	30		50		60		80		100		120	
	Re	$D_h Re/L$	Re	$D_h Re/L$	Re	$D_h Re/L$	Re	$D_h Re/L$	Re	$D_h Re/L$	Re	$D_h Re/L$
1	15.466	0.473	22.340	0.605	25.132	0.644	29.786	0.449	33.510	0.489	36.556	0.743
2	26.235	0.555	37.896	0.670	42.632	0.701	50.527	0.737	56.843	0.758	62.011	0.770
3	35.739	0.600	51.623	0.701	58.076	0.727	68.830	0.756	77.434	0.772	84.474	0.782
4	44.504	0.629	64.283	0.720	72.318	0.742	85.711	0.767	96.424	0.780	105.190	0.788
5	52.758	0.650	76.206	0.733	85.731	0.752	101.608	0.774	114.309	0.786	124.700	0.793
6	60.626	0.666	87.571	0.743	98.518	0.760	116.762	0.779	131.357	0.789	143.298	0.796

Table B.1: wRe/L for all single throttle runs

B.0.4 CFD Results

B.0.4.1 Double Channel Geometry

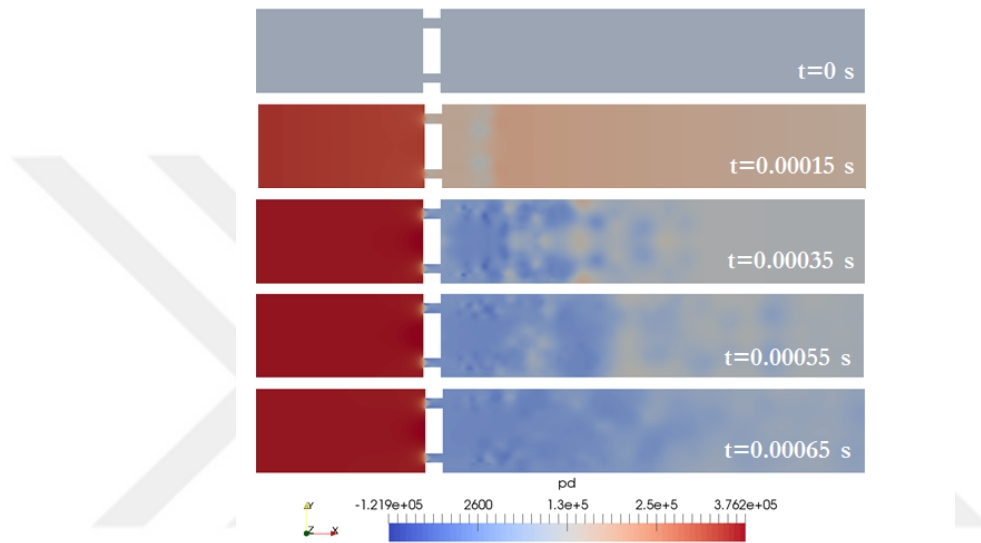


Figure B.5: Pressure contour with respect to time for double channel geometry

B.0.4.2 Triple Channel Geometry

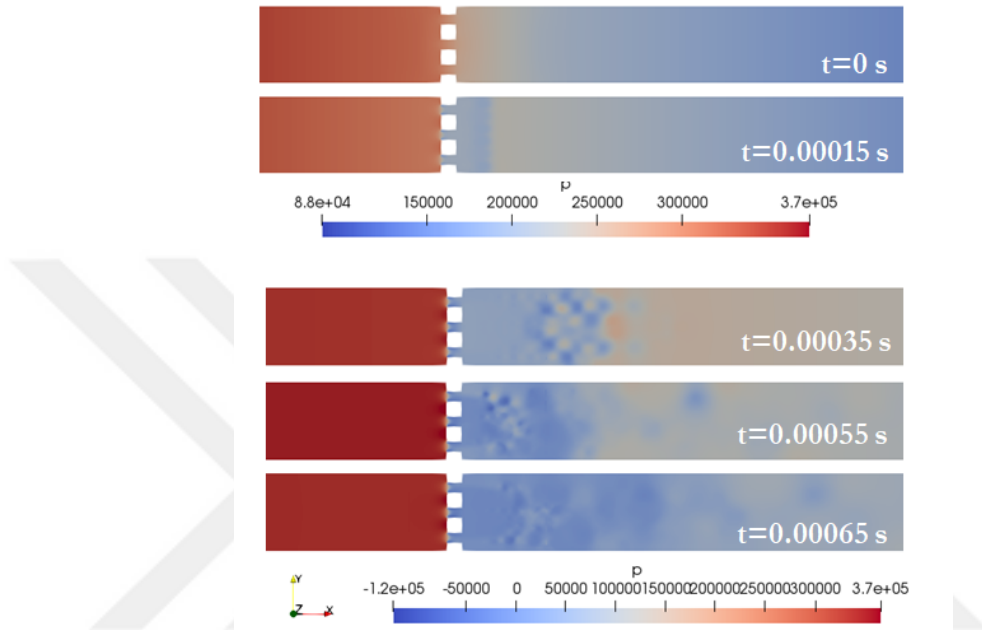


Figure B.6: Pressure contour with respect to time for triple channel geometry

B.0.4.3 Nozzle Inspired Channel Geometry

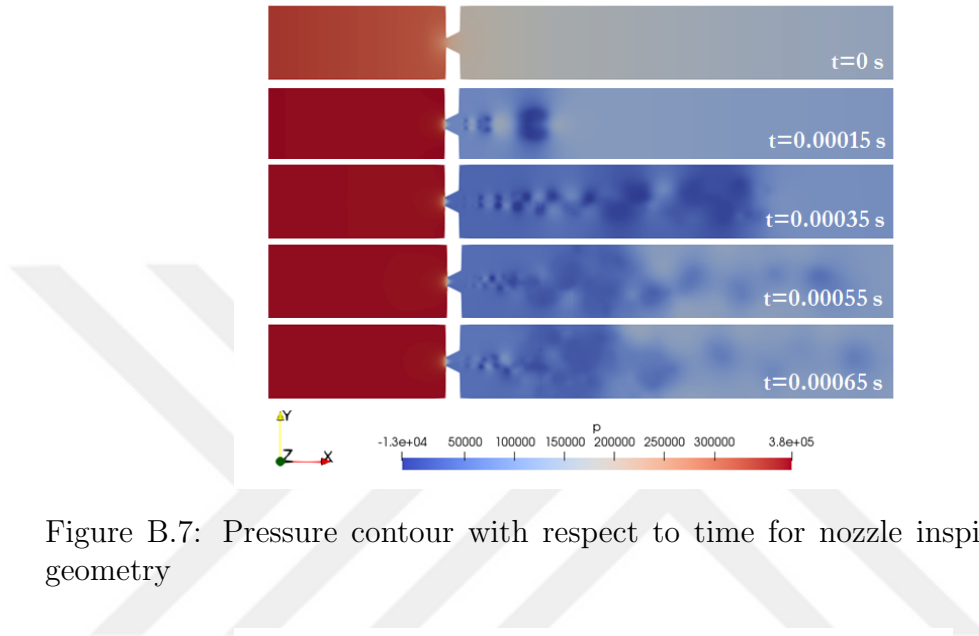


Figure B.7: Pressure contour with respect to time for nozzle inspired channel geometry

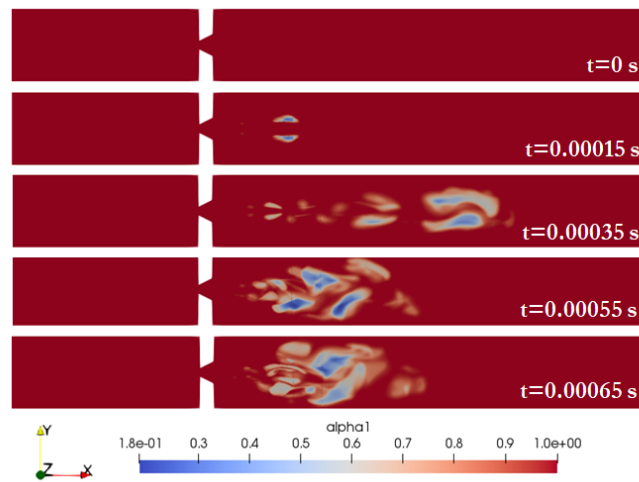


Figure B.8: Pressure contour with respect to time for nozzle inspired channel geometry

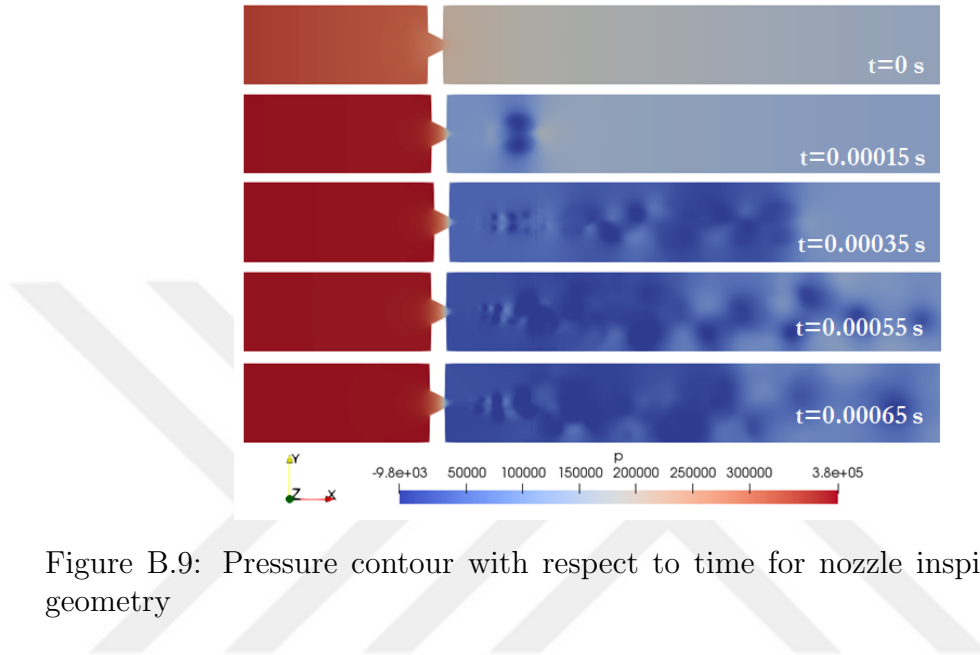


Figure B.9: Pressure contour with respect to time for nozzle inspired channel geometry

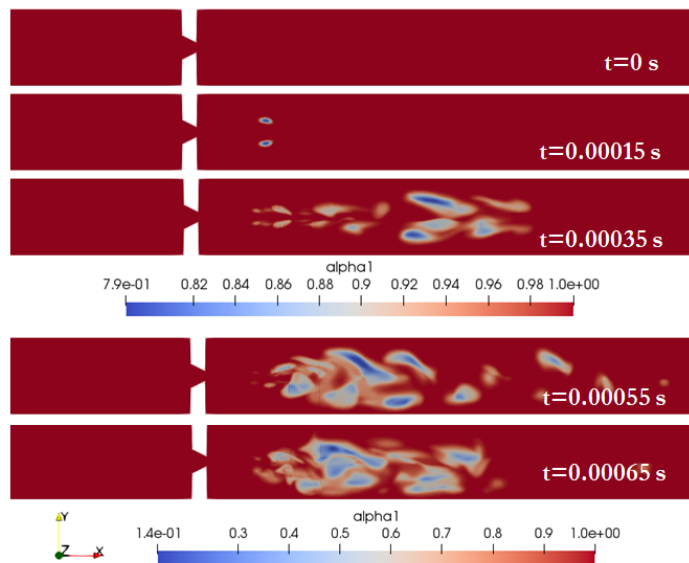


Figure B.10: Pressure contour with respect to time for nozzle inspired channel geometry

B.0.4.4 Double Inclined Channel Geometry

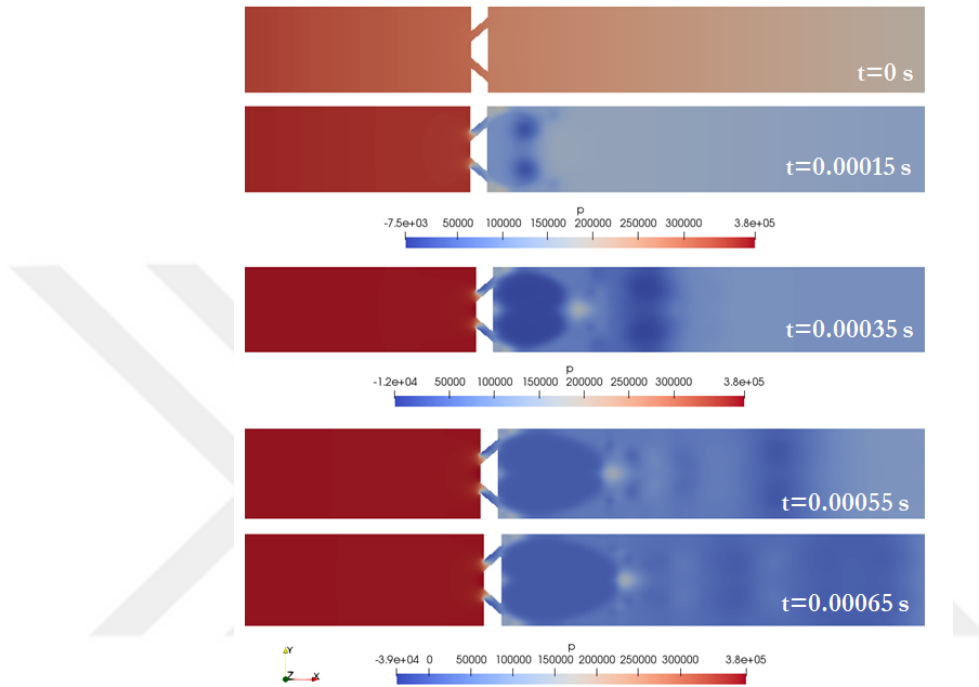


Figure B.11: Pressure contour with respect to time for double inclined geometry

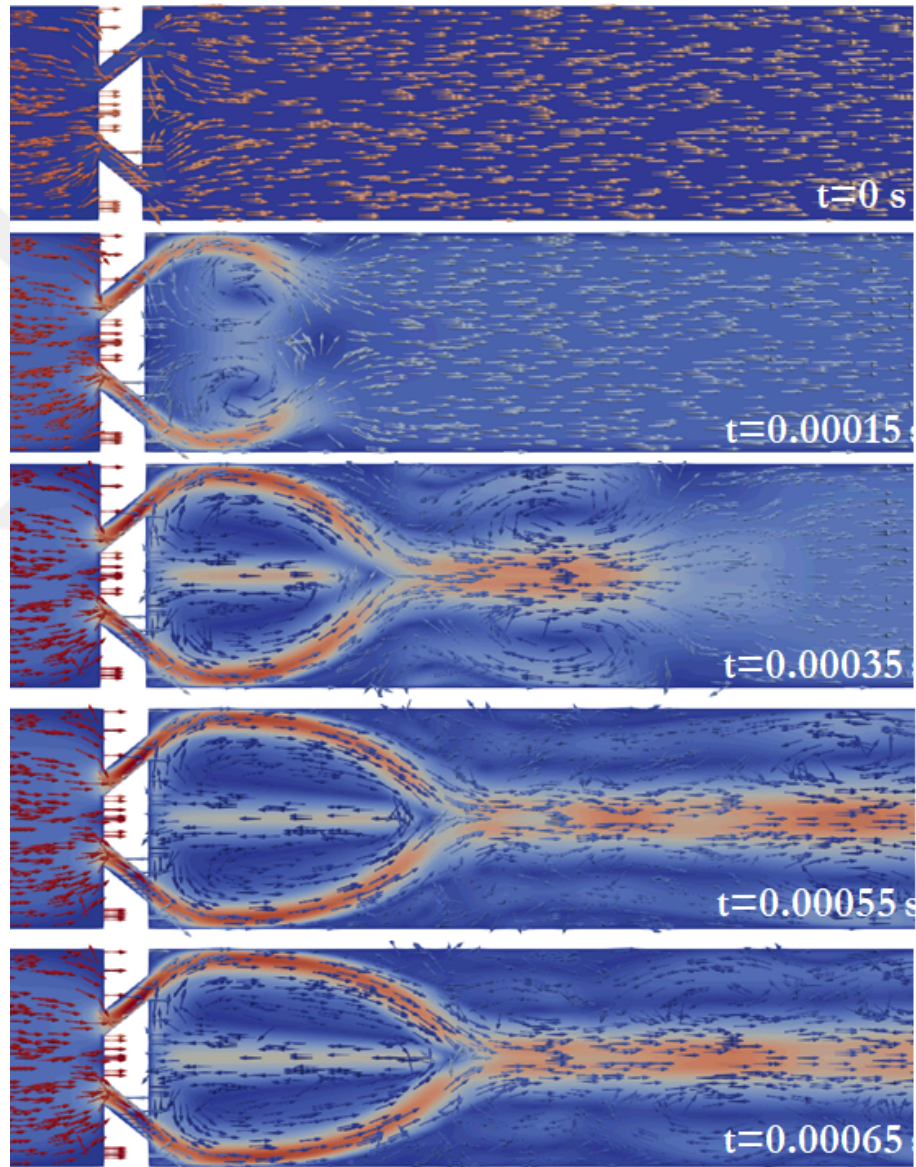


Figure B.12: Velocity vectors with respect to time for double inclined geometry

Appendix C

Masks

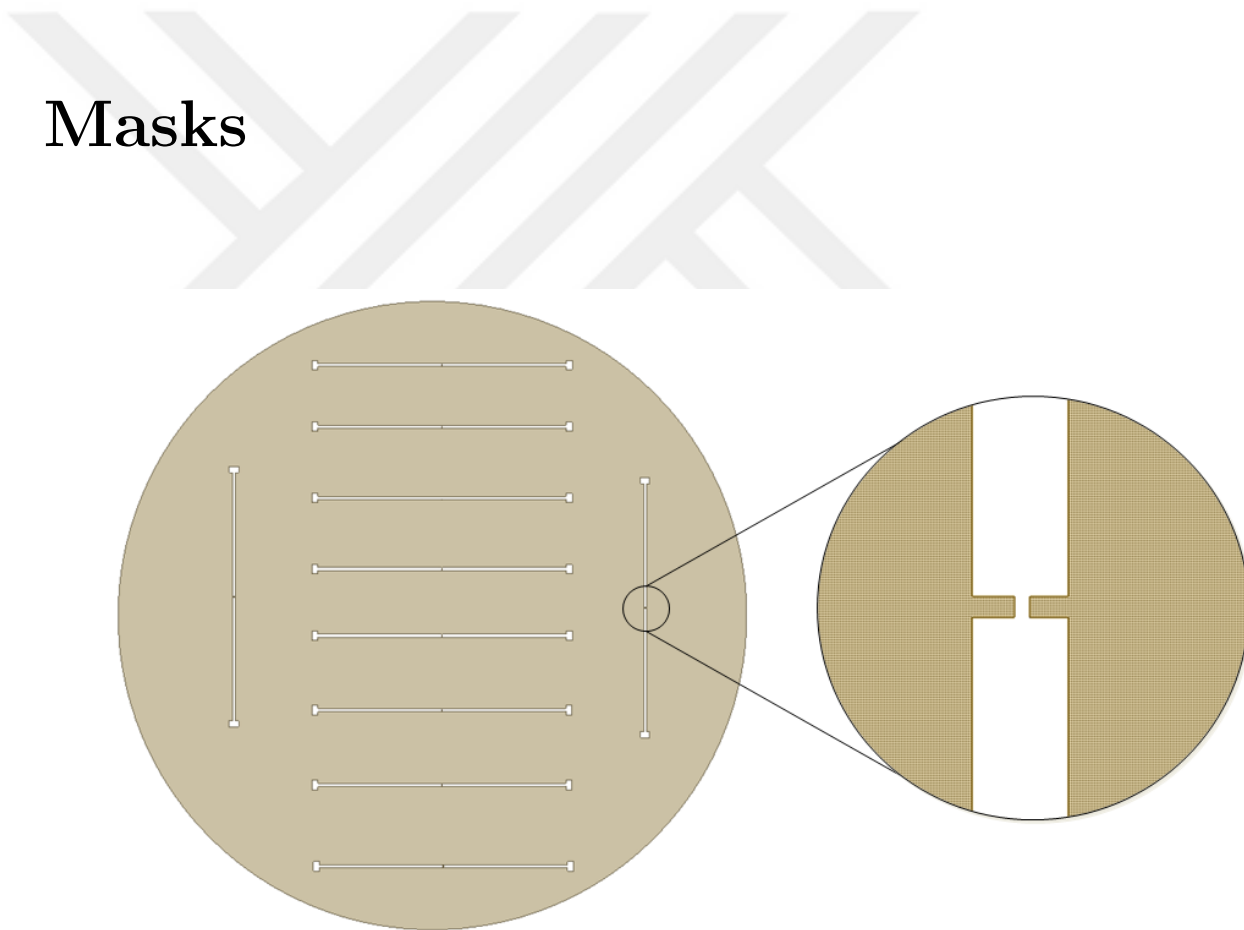


Figure C.1: Mask 1

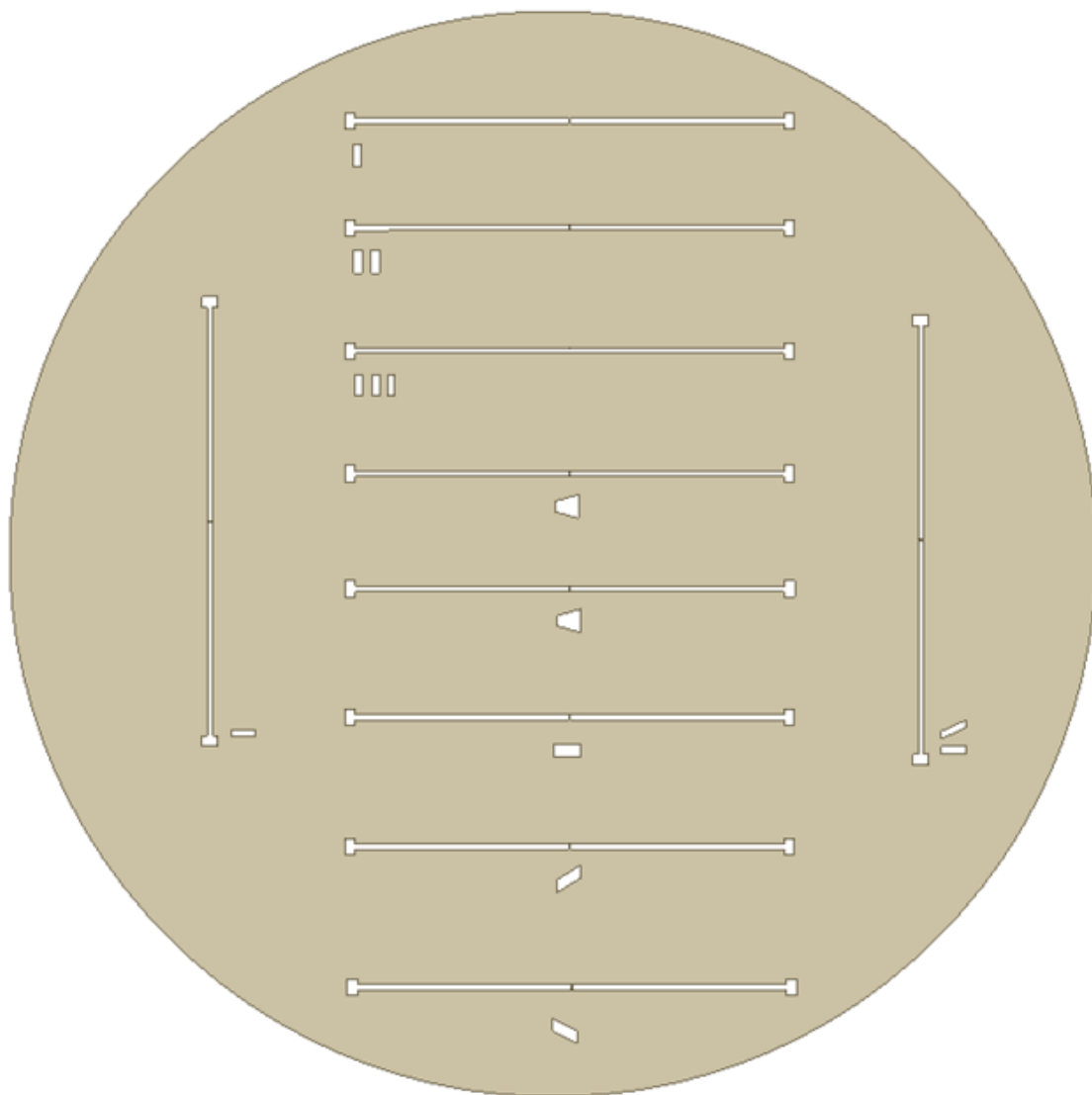


Figure C.2: Mask 2

Appendix D

Experiment Visuals

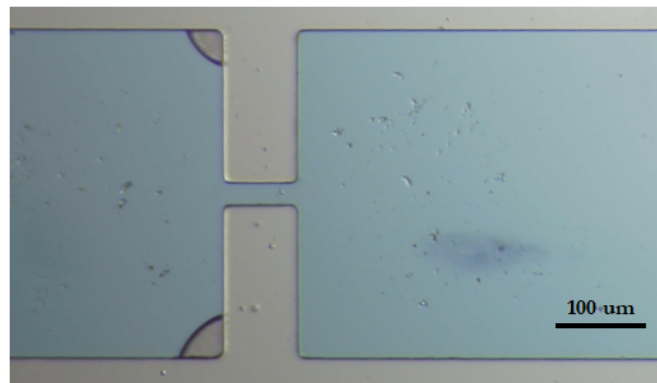


Figure D.1: Bubble vapors for 30 micron channel